THE IMAGE QUALITY AND DOSIMETRIC BENEFITS OF A NOVEL 2.5 MV SINTERED DIAMOND TARGET BEAM ON A MODERN RADIATION THERAPY LINEAR ACCELERATOR

by

Jennifer Marie Borsavage

Submitted in partial fulfilment of the requirements
for the degree of Doctor of Philosophy

at

Dalhousie University
Halifax, Nova Scotia
August 2024

Dalhousie University is located in Mi'kma'ki, the ancestral and unceded territory of the Mi'kmaq. We are all Treaty people.

Dedication

For Luke – forever grateful for your love and support. Thank you for pushing me through.

EHGW, EMKW, KLG, MAP and all individuals and families who've been afflicted by cancer.

Table of Contents

LIST OF TABLES

LIST OF FIGURES

ABSTRACT

Targeted dose delivery is achieved in radiotherapy treatments using image guidance for accurate patient positioning, and specialized collimators to shape the radiation field to the beam's-eye-view of the treatment volume while shielding healthy tissue. Image guidance plays an important role in this workflow to inform patient setup before and/or during treatment. In the stereotactic treatment scheme, which involves high dose delivery in one or a few treatments, dose conformity to the treatment volume is of heightened concern, necessitating sharp dose fall-off immediately beyond the prescription isodose surface.

The purpose of this thesis is two-fold; to investigate the potential improved image quality in beam's-eye-view MV image guidance and the dose fall-off in stereotactic treatments using a novel 2.5 MV low-Z target beam on a modern linear accelerator. Due to the decreased photoelectric absorption of low-energy photons within the target, low-Z beams contain higher proportions of low-energy photons compared to a high-Z target beam. In this work, a commercial 2.5 MV beam was modified to replace the conventional copper target with sintered diamond. It was hypothesized that this modification would produce a beam with a higher yield of low-energy photons that would contribute improved contrast characteristics for imaging and sharper dose fall-off for stereotactic treatments.

This thesis is composed of three manuscripts that examine the image quality characteristics of the novel beam and the dosimetric characteristics in stereotactic treatments. The first manuscript, 'Investigation of planar image quality for a novel 2.5 MV diamond target beam from a radiotherapy linear accelerator', evaluates the planar image quality of the 2.5 MV low-Z target beam compared to the commercial 2.5 and 6 MV beams. This work demonstrates improved planar image quality compared to the commercial beams. The second manuscript, 'Improving image quality and reducing dose with 2.5 MV diamond target volume-of-interest cone beam CT', investigates the image quality and dose characteristics of the 2.5 MV low-Z target beam in both full field of view and volume of interest cone beam CT. This study reports on improved image quality in both acquisition modes and the resultant dose-sparing from collimation in volume of interest acquisitions. The third manuscript, 'Investigation of a novel 2.5 MV sintered diamond target beam for intracranial linac-based stereotactic treatments', evaluates the 2.5 MV low-Z target beam in stereotactic treatments of trigeminal neuralgia and ocular melanoma. This study describes a dosimetric advantage in terms of dose fall-off and sparing of normal tissue compared to a conventional 6 MV beam.

The manuscripts contained in this thesis highlight the design and installation of the sintered diamond target, the methods of evaluating the novel beam in both imaging and stereotactic treatment applications, and the combined image quality and dosimetric advantages which could be realized through clinical implementation.

LIST OF ABBREVIATIONS USED

ALARA = As low as reasonably achievable

BEV = Beam's-eye-view

CAX = Central axis

CBCT = Cone beam computed tomography

CNR = Contrast-to-noise ratio

CPE = Charged particle equilibrium

CSDA = Continuous slowing down approximation

DQE = Detector quantum efficiency

DSB = Double strand break

EBRT = External beam radiation therapy

EPID = Electronic portal imaging device

FFF = Flattening filter free

FOV = Field of view

HDMLC = High definition multileaf collimator

IGRT = Image guided radiation therapy

KERMA = Kinetic energy released per unit mass

linac = Linear accelerator

MC = Monte Carlo

MLC = Multileaf collimator

MTF = Modulation transfer function

MU = Monitor unit

OAR = Organ at risk

OM = Ocular melanoma

PDD = Percent depth dose

PTV = Planning target volume

QA = Quality assurance

RMTF = Relative modulation transfer function

SAD = Source-to-axis distance

SBRT = Stereotactic body radiation therapy

SID = Source-to-imager distance

SNR = Signal-to-noise ratio

SRS = Stereotactic radiosurgery

SRT = Stereotactic radiotherapy

SSB = Single strand break

SSD = Source-to-surface distance

TCPE = Transient charged particle equilibrium

TN = Trigeminal neuralgia

TPS = Treatment planning system

VOI = Volume-of-interest

Z = Atomic number

ACKNOWLEDGEMENTS

Thank you to my supervisors, Dr. James Robar and Dr. Amanda Cherpak for their unwavering support, patience, and encouragement. I appreciate the opportunities which you have afforded for me and look forward to our paths continually crossing. And to the rest of my committee members, Thalat Monajemi and Michael Ha for your guidance. It's been a pleasure learning from all of you.

Thank you, Mom and Dad, for helping me get here, all my accomplishments are owed to you. To you and my sisters, for guiding and supporting me in my long-haul academic pursuits. Thank you all for continually lifting me up, every time without fail.

To Jameson, forever appreciative for you - for uprooting your life to adventure to Nova Scotia with me, taking care of me through this journey, helping me with my experimental setups, and always encouraging me to continue.

Donnie, thank you for always coming to visit, for all your support, and the numerous plane tickets home when I needed a reset. Looking forward to forever exploring Nova Scotia with you!

To Matthew, thank you for your friendship. Grateful for all our goofy times and brainstorm/collaboration sessions. Your comradery is unmatched – so thankful to have you by my side throughout this journey and all that's next!

Katie and Jess, thank you for your visits, love, and confidence boosting. Grateful for the opportunity to share this place with you.

To all my Halifax friends, I LOVE YOU!

Nova Scotia, thankful for your acceptance, beauty, and rum cream.

Chapter 1 Introduction

1.1 The global burden of cancer

Cancer is a growing global burden, ranking as one of the leading causes of death worldwide and accounting for nearly 1 in 6 deaths in 2020[1]. The global occurrence is estimated to increase by 47% in 2040, amounting to 28.4 million new annual cases compared to 19.3 million in 2020[2]. These increased trends in incidence and mortality mirror the global change in population in terms of aging and growth and are further contributed by sociodemographic factors[2]. In Canada, cancer is the leading cause of death, surpassing cardiovascular disease; national statistics estimate that 2 in 5 Canadians will receive a cancer diagnosis in their lifetime and 1 in 4 Canadians will die from cancer[3]. The prevalence is similar in the United States, where it is estimated that 41/100 men and 39/100 women will develop a cancer in their lifetime[4]. Based on 2021 statistics, cancer wears the heaviest burden on people 55+ in the US, comprising 80% of all cases[4].

While there are uncontrollable factors contributing to the global incidence of cancer (i.e. aging), the apparent sociodemographic influences are a societal responsibility to address. The World Health Organization projects that nearly 30% of cancer cases in low- and lower-middle-income countries originate due to cancer-causing infections such as human papilloma virus and hepatitis and one third of cancer deaths are due to lifestyle including alcohol/tobacco use, obesity and diet, and a lack of physical activity[1]. It is important for clinicians and researchers to acknowledge the systemic social and political influences

which contribute to an individual's health conditions and the overarching socioeconomic disparities of cancer in pursuit of tackling the disease. Creating equity in healthcare requires parity in health education, livable wages and fair working conditions, universal access to vaccines, screening, and access to quality treatment to mitigate these social inequalities.

With a continuously expanding understanding of the disease and the advancing technologies with which cancer can be detected and treated, clinicians and researchers are urged to improve global cancer outlooks. Considering the global aging population and the existing disparities in cancer prevention and treatment, increased accessibility to affordable care is imperative to lessen the burden of cancer on the healthcare system and society combined. In addition to creating more accessibility and equity in cancer care, continuous research and development efforts geared toward improving treatment techniques and modalities are prerogative to improving patient outcomes.

1.2 The role of radiation therapy in cancer treatment

Cancer describes a set of diseases characterized by the uncontrolled reproduction of abnormal cells that have the potential to spread to other parts of the body. Cancer is a genetic disease which may occur in all cell types and tissues, arising from changes in the genes which control cellular growth and division. These genetic changes can result from environmental and hereditary influences as well as intrinsic genetic errors which occur in the cell division process [5]. The hallmarks of cancer can be described by eight phenotypes,

classified by Hanahan, including 1) sustained proliferative signaling, 2) evasion of growth suppressors, 3) resisting cell death, 4) enabling replicative immortality, 5) angiogenesis (i.e. growth of vasculature to supply tumor), 6) activating invasion and metastasis, 7) reprogramming cellular metabolism, and 8) avoiding immune destruction[6]. While all cancers possess common traits, the genotype of the disease is highly heterogenous, complicating the development of a single curative treatment. Instead, prescribed treatment regimens are tailored to the type, stage, and genetic profile of the disease. Common therapies employed in the treatment of cancer include surgery, chemotherapy, radiation therapy and immunotherapy. Surgery is the gold standard treatment, which is commonly combined with adjuvant radiation therapy, where adjuvant describes the combination of treatments to improve the total efficacy. In this scheme, radiation therapy can be administered before surgery to shrink the tumor (i.e. neoadjuvant) or after surgery (i.e. adjuvant) to eliminate the microscopic disease left behind from surgery. Radiation therapy may also be prescribed as the primary treatment, for both curative and palliative indications, where palliative treatment is administered to help relieve the symptoms of cancer for late-stage cases[5]. It is estimated that nearly 50% of all cancer patients receive radiation therapy at some point during their treatment regimen[7–9] and approximately 60% of those receiving radiation therapy are undergoing curative treatment[8]. Radiation therapy can be delivered using an external beam of radiation or internal radioactive sources, as used in brachytherapy. External beam radiation therapy (EBRT), as is the focus of this thesis, is the most common radiation therapy treatment modality.

1.3 Biological mechanisms of ionizing radiation in cancer therapy

Ionizing radiation describes particles and electromagnetic waves (i.e. x-rays or photons) that possess enough energy to remove one or more orbital electrons from the atoms and molecules composing the matter through which it passes. Radiobiology is the study of the biological response of tissues to ionizing radiation[10], forming the basis for the use of radiation therapy in cancer treatment. In the simplest context, ionizing radiation interacts with the cells in a tumor, causing irreparable damage that leads to cell death. This cellular damage results from the ionization of critical cellular structures (i.e. DNA). DNA damage can occur by direct or indirect action. Direct action results from the ionization of atoms or molecules contained within the DNA through interactions with ionizing radiation. Indirect action occurs when ionizing radiation interacts with other atoms or molecules within the cell to form free radicals which impart biological damage to DNA. Due to the unpaired orbital electron, free radicals are chemically unstable and highly chemically reactive. Free radicals interact with the surrounding matter by stripping orbital electrons from the constituent atoms/molecules to reach a more stable state[11]. When in proximity, these free radicals can interact with DNA. The damage that occurs from direct or indirect ionization of DNA results in the breakage of chemical bonds which can sever the strands of DNA. A single strand break (SSB) occurs when one nucleotide is damaged, cleaving one strand of the double-helix into two pieces. Due to the complimentary base pairing of DNA strands, the intact sister strand serves as a template for repairing the damaged nucleotide, and thus SSBs are of insignificant consequence. Double strand breaks (DSBs) result from the breakage of both DNA strands at nucleotides which are adjacent or

separated by only a few base pairs. Unlike SSB repair, DSBs do not have a reliable template to facilitate repair of complimentary base pairs and is therefore error prone. DSBs are of heightened importance, as their occurrence can lead to cell death, carcinogenesis or genetic mutation [10].

The biological response to ionizing radiation can be quantified using the linear quadratic model, which characterizes the surviving fraction of an in vitro cell culture as a function of radiation dose. The formulation of this model is as follows, $S = e^{-(\alpha D + \beta D^2)}$, where S represents the surviving fraction of cells, D is the radiation dose, and α and β are constants which represent the different components of cell killing. The linear component, as described by α, represents the cell death occurring from a 'single hit' event, or lethal damage inflicted by a single particle track. The quadratic component, characterized by β, represents the cell death that occurs due to the interaction of biological damage incurred from multiple particle tracks. The ratio of the two components, α/β, represents the dose at which both cell killing components are equal, and characterizes the relative radiosensitivity of a given cell line. Typically, malignant cells demonstrate a high α/β ratio (~10 Gy), whereas normal tissues have a low α/β ratio (~3 Gy)[12].

Due to the risks posed to surrounding healthy tissues, the prescribed dose in radiation therapy is typically delivered in daily treatments of small doses (~1.5-3 Gy)[5], known as fractions, over a period of several weeks. Fractionation schemes are based on the different radiosensitivities and repair capacities of healthy and malignant cells.

Fractionation exploits these differences by providing time for the normal tissue to repair radiation induced damage while maintaining the cumulative damage to the tumor cells. In addition to the allotted repair period for healthy tissues, fractionation also benefits the radiosensitivity of tumor cells. These observed effects are based on the underlying radiobiological principles known as the four R's of radiobiology[10], as follows:

1. Repair – Between fractions, cells have the ability to repair sub-lethal damage caused by radiation.
2. Reassortment – Cells redistribute through the cell cycle following irradiation. This reassortment increases the likelihood of larger tumor cell populations in a more radiosensitive phase of the cycle during subsequent fractions.
3. Repopulation – Cells can repopulate through cellular division between fractions.
4. Reoxygenation – As tumor cells die following irradiation, hypoxic cells may reoxygenate due to increased blood supply, increasing the radiosensitivity in subsequent fractions.

1.4 External beam radiation therapy

Radiation therapy involves the delivery of ionizing radiation to treat malignant tumors or otherwise benign conditions using either an internal source (i.e. brachytherapy) or an external beam of radiation, as in external beam radiation therapy (EBRT). The type of ionizing radiation used in EBRT can be either electrons, photons, protons, or heavy ions; selected based on the treatment site and/or accessibility. In general, photons are most common and will be the focus of discussion herein. There are several platforms on which

EBRT can be delivered, including teletherapy, linear accelerators, tomotherapy, linear accelerators on robotic arms etc., each differing in the engineering design, available treatment energies and image guidance systems. One common feature among EBRT platforms is a collimation system that serves to shape the photon beam, transmitting particles through the open aperture (i.e. field) and blocking those outside. The collimation system enables targeted dose delivery, focusing the dose to the treatment volume while obstructing the particle fluence directed towards the surrounding healthy tissues. Specification of the radiation field is informed by the anatomy being treated, necessitating a pre-treament imaging set for planning purposes in the EBRT workflow.

1.4.1 EBRT treatment workflow

Following diagnosis and treatment prescription, the typical EBRT workflow can be broken down into six major steps as follows:

(i) Acquire pre-treatment image dataset(s)

(ii) Contour treatment volume and surrounding organs at risk (OARs)

(iii) Treatment planning

(iv) Treatment plan quality assurance (QA)

(v) Patient Setup

(vi) Treatment delivery

These steps are illustrated in Figure 1, below.

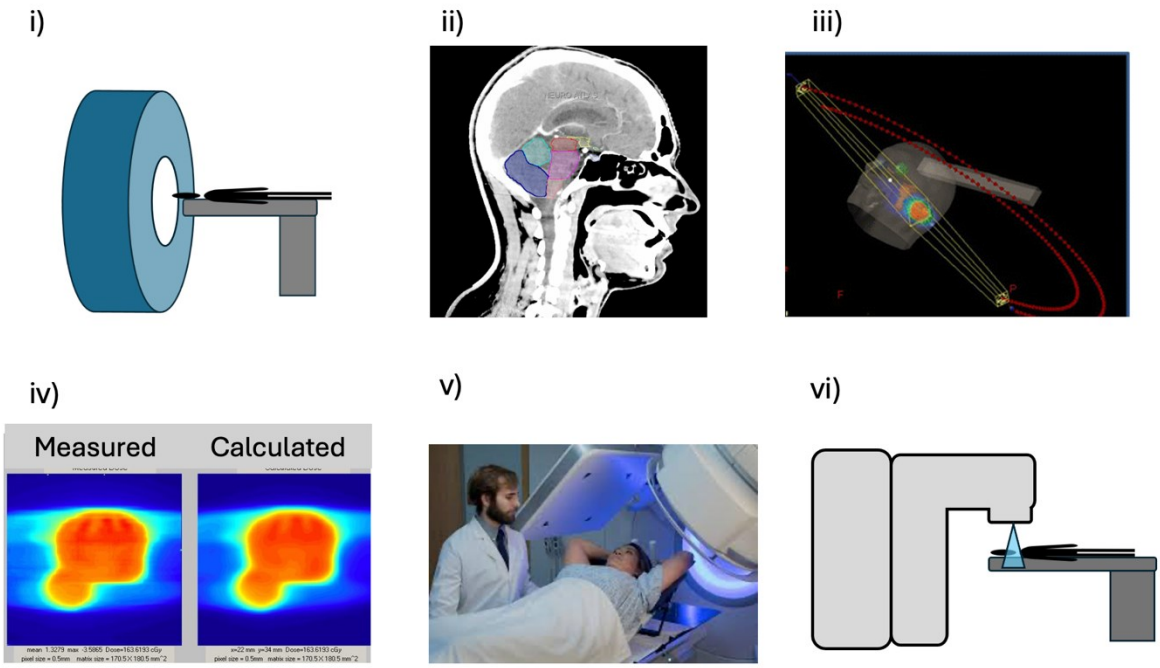

Figure 1. Illustration of the EBRT workflow including: i) acquisition of pre-treatment image datasets, ii) contouring of treatment volume and organs at risk, iii) treatment planning, iv) treatment plan quality assurance, v) patient setup, and vi) treatment delivery. .

The pre-treatment planning CT serves two main functions in EBRT, providing the geometric information about the anatomy and the material composition data. The geometric data is used for contouring structures of interest and raytracing for calculation of particle fluence, whereas the material composition is needed for converting particle fluence to absorbed dose in each media through which the particles are transported. Once the anatomy has been contoured on the planning CT, the planner optimizes the beam placement and relative dose contributions of each field to achieve the best balance between dose coverage to the treatment volume and dose sparing of OARs. Before treatment can be delivered to the patient, QA checks are performed to ensure that the plan is satisfactory in terms of its dosimetric characteristics and machine deliverability. This may involve delivery of the plan to a detector to compare the measured distribution

to that calculated in the TPS, as illustrated in the figure. On the day of treatment, the patient is set up on the machine to align the treatment anatomy with respect to the central axis of the treatment beam, according to the treatment plan. Verification of patient setup is performed by acquiring planar or volumetric images to confirm proper alignment. If necessary, the radiation therapist will shift the treatment couch to adjust the alignment according to the comparison between setup and planning CT images. The utilization of imaging in this scheme describes image guidance, or image guided radiation therapy (IGRT), in which the anatomical information guides planning, setup, and/or treatment decisions. Once the patient is properly aligned to the machine, according to the treatment plan, treatment is delivered.

1.4.2 Significance of IGRT

Image guidance plays an important role in delivering precise radiotherapy treatment by providing means for accurate patient setup and monitoring of patient positioning. In the delivery of EBRT, image guidance refers to any imaging modality which aids in the localization of the treatment anatomy before or during treatment. All modern radiotherapy treatments employ CT image guidance for planning purposes, but additional modalities may be used depending on the treatment site and system availability. Of the numerous image guidance systems available, the most common are the MV and kV on-board imaging systems equipped on most modern linear accelerators. Although kV imaging is advantageous in terms of image quality and dose, there are instances in which MV imaging may prove useful (e.g., imaging of the chest wall during treatment of breast

cancer). The current TrueBeam (Varian Medical Systems, Palo Alto, CA) treatment platform is equipped with a 2.5 MV imaging-exclusive beam, providing increased contrast compared to the higher quality treatment beams (i.e. 4 MV or 6 MV)[13]. The improved contrast is due to the larger proportion of diagnostic energy x-rays in the beam, which can be further optimized by replacing the current target material with sintered diamond[14].

1.5 Low-Z targets

Typical MV radiotherapy beamlines contain a thick high atomic number (Z) target used in photon production. Photon production occurs when electrons are accelerated into the target, in which they interact through a radiative process called bremsstrahlung. In this process, the electrons undergo coulombic interactions with the nuclei of the target material causing them to slow down, losing some or all their energy. The energy lost by the electron is emitted as a photon. While this explanation is brief, the mechanisms of photon production in linear accelerators and the bremsstrahlung process are discussed in detail in section 2.1. The low energy bremsstrahlung photons produced in the superficial layers of the target will be preferentially attenuated via photoelectric absorption within a high-Z target compared to a low-Z alternative. This is illustrated in Figure 2 which demonstrates example spectra generated from a 6 MeV beam incident on a low-Z and high-Z target. In this figure, the 6 MV photons emerging from the respective targets represent sample energy spectra, depicting the relative proportion of high energy photons (higher frequencies) and low energy photons (lower frequencies), as reflected in

the corresponding plotted spectra. The preferential attenuation of low energy photons is due to the Z^3 dependency of the photoelectric mass attenuation coefficient which governs the probability of interaction, as is discussed in section 2.4.1. Implementing a low-Z target for photon production allows for recovery of more of these photons, which are advantageous for creating contrast in x-ray imaging.

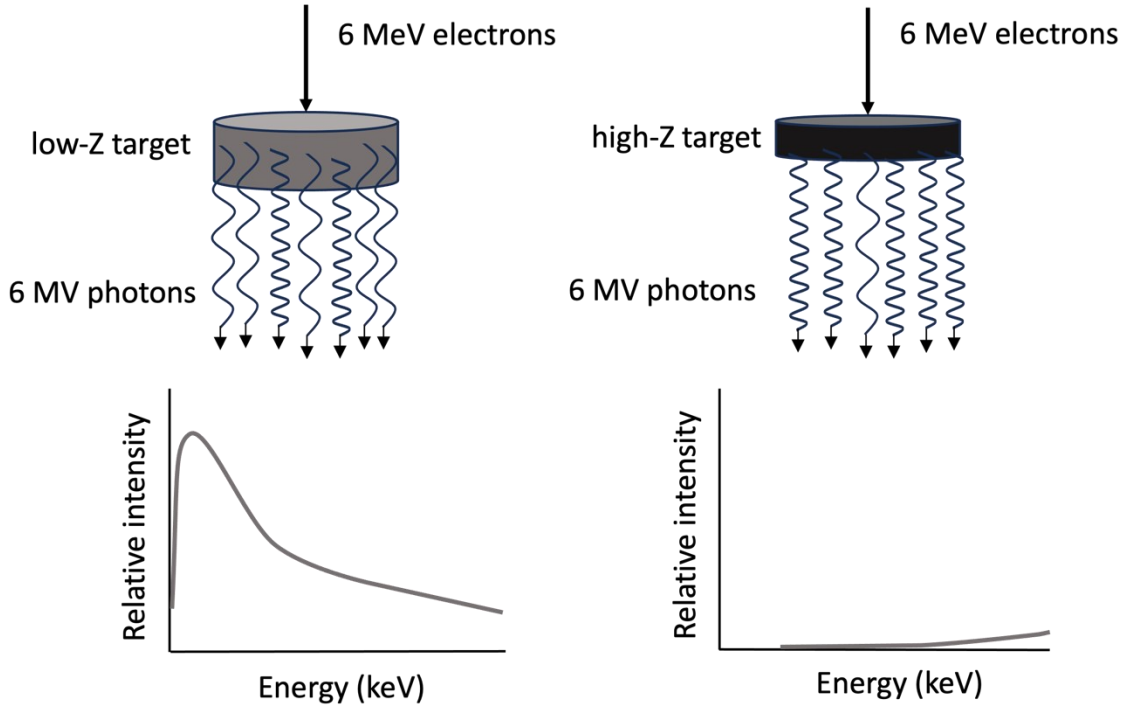

Figure 2. Illustration of preferential photoelectric absorption of low energy photons in high-Z targets with corresponding spectra.

1.5.1 Low-Z target history

The application of low-Z targets in MV beam production was first theorized by Galbraith in 1989 as means of improving the achievable contrast in portal imaging[15]. Galbraith's work indicated a need for an imaging-optimized beam, explaining that treatment beams

were purposely designed to prioritize high energy photons. While all unfiltered bremsstrahlung beams possess a continuous spectrum of energies (i.e. ranging from 0 MeV to the accelerating potential of the incident electrons), a typical treatment beam contains a minimal fraction of low-energy photons (e.g. 0.3% for 6 MV)[16]. Though this is advantageous for producing the desired dose characteristics for treatment, diagnostic energy photons (i.e. 25 – 150 keV)[17] create contrast in an image and should therefore be abundant in a beam used for imaging. Galbraith suggested the implementation of a low-Z target to maximize the yield of diagnostic energy photons, creating a beam more suitable for MV imaging. To test his hypothesis, Galbraith installed beryllium and graphite targets on an AECL Therac-20 for 4 and 6 MV beam production, demonstrating an increase in the fractional yield of diagnostic energy photons and a resultant improvement in contrast by factors up to two times compared to the 6 MV treatment beam[15]. Since Galbraith's inaugural low-Z target study over three decades ago, low-Z targets have been investigated on various treatment platforms, using a variety of low-Z materials and incident electron energies.

Low-Z targets have been experimentally implemented on many major commercial linear accelerators including Siemens Mevatron MXE[17], Oncor[18], Primus[19], KD2[19], and Artiste[19] systems, Elekta Precise[20] and SL25[21,22] units, as well as Varian 2100 EX[16,23–25] platforms. The optimal target material has been extensively investigated with a concentration on carbon, beryllium and aluminum as the frequent candidates. While most studies identified the largest contrast benefit would be obtained by using the lowest Z material,

Flampouri et. al. observed similar contrast characteristics amongst beams produced with aluminum, carbon and beryllium targets. Due to these similarities, this group prioritized the modest 5-10% increase in bremsstrahlung efficiency achieved using the aluminum target[21,22]. Ostapiak et. al. observed the greatest fluence of low energy photons (i.e. $h\nu <$ 300 keV) for a beryllium target, however, these authors recommended carbon due to the material cost as well as the associated toxicity with machining beryllium[17]. Within the last 15 years, recent studies have converged on carbon as the ideal material. While most authors utilized graphite, Sawkey et. al. demonstrated similar image quality amongst sintered diamond and graphite target beams noting the benefits of the increased sintered diamond density[18].

In addition to target material, target thickness has been investigated for effects on contrast and spatial resolution. Early studies which utilized thin targets (i.e. thickness less than the continuous slowing down approximation (CSDA) range of incident electrons) required use of a plastic filter downstream from the target to absorb transmission electrons. Flampouri et. al. demonstrated minimal variation in spectral characteristics and consequent contrast with target thickness[21], motivating the use of full thickness targets in later studies. In terms of spatial resolution, Connell and Robar demonstrated a slightly improved spatial resolution for a full thickness 4.5 MeV/beryllium target beam compared to the clinical 6 MV beam. While this trend was not consistent across all the low-Z target beams they investigated, they noted that all beam parameter combinations produced beams with sufficient spatial resolution compared to 6 MV. In addition to target thickness,

Connell and Robar examined the effect of target placement on spatial resolution. Due to electron scatter in air, this study concluded that placing the target closest to the exit window of the accelerating structure from which the electron beam emerges made the greatest impact on the achievable spatial resolution [25].

Most early studies utilized nominal treatment energies for generating low-Z target beams, primarily 4 and 6 MV. While this was practical for initial proof of concept, early data demonstrated benefit from the combination of low energy/low-Z target beams[26]. Parsons and Robar generated beams with energy less than 2.40 MeV using beam tuning to allow selection of mean electron energy between 1.90 and 2.35 MeV[23]. At these energies, the authors observed CNR improvements by factors ranging from 6.2-7.4 and 3.7-4.3 times in thin and thick phantoms[23], respectively, compared to previous improvements of 2.7-3.8 times for a 3.5 MeV beam[24]. Parsons and Robar concluded insignificant differences between image quality achieved with the 2.35 MV beam compared to 1.90 MV but noted a near 2X increase in the electron beam current. As a result, the authors suggested the use of 2.35 MV carbon target beam for further low-Z target investigation[23].

In 2013, Varian proposed a 2.5 MV 'low-X' imaging mode for the TrueBeam 2.0 platform as a commercial solution to improve MV image quality. Before the release of the new platform, Parsons et al. evaluated the proposed low-X imaging beam against two 2.35 MV carbon target beams on the TrueBeam and Clinac platform using Monte Carlo simulations in VirtuaLinac and BEAMnrc. Compared to the 2.35 MV carbon target beam on the Clinac

platform, Parsons et al. observed a decrease in the relative fraction of diagnostic energy photons by 10% and 28% for the 2.35 MV carbon target and 2.5 MV low-X beams, respectively, on the TrueBeam platform. The harder photon energy spectra decreased contrast by factors of 1.1 and 1.4 (thin phantom) and 1.03 and 1.4 (thick phantom), for the 2.35 MV carbon target and low-X beams, respectively, compared to the 2.35 MV carbon target Clinac beam[14]. Despite the advances made to the portal imaging system, the findings by Parsons and Robar suggest that the current MV image contrast could be further improved, motivating our experimental implementation of low-Z targets in the 2.5 MV beamline on the TrueBeam platform. These studies, along with other low-Z target studies described in section 2.7 have been summarized by Robar in Table 1.

Table 1. Summary of low-Z target parameters used in previous studies and corresponding effects on imaging[27]

Author	Target thickness and material	Electron energy	Effect on imaging[a]
Galbraith (1989)	14.2 mm graphite	6 MeV	Contrast increase by up to a factor of 2
Tsechanski et al. (1998)	5 mm aluminum	4.0 MeV	Qualitative improvement of contrast in head-and-neck imaging
Ostapiak et al. (1998)	16.5 mm beryllium, 15.7 mm carbon	6.0 MeV	Contrast increase by up to a factor of 4
Flampouri et al. (2005)	6 mm aluminum	4 MeV	Contrast increase by up to a factor of 9.5 (thin objects)
Faddegon et al. (2008)	13.2 mm graphite	4.2 MeV	Contrast-to-Noise Ratio (CNR) increase by a factor of 3, improvement of spatial resolution by a factor of 2
Roberts et al. (2008)	20 mm carbon (28%), nickel exit window (71%)	5.6 MeV (mean)	Contrast increase by factor of 1.3 for thick objects and 4.6 for thin objects
Orton et al. (2009)	10 mm aluminum	6.0 MeV	Contrast increase by a factor between 1.6 and 2.8
Robar et al. (2009a)	6.7 mm and 10.0 mm aluminum	3.5 MeV and 7.0 MeV	CNR increase by up to a factor of 2.4 (7.0 MeV) and 4.3 (3.5 MeV)
Sawkey et al. (2010)	13.2 mm graphite, 13.2 mm sintered diamond	4.6 MeV and 6.4 MeV	Similar CNR/dose with diamond compared to graphite
Roberts et al. (2011)	20 mm carbon (28%), nickel exit window (71%)	5.6 MeV (mean)	Factor of 5 to 7 less dose required for comparable CNR
Fast et al. (2012)	13.2 mm graphite	4.2 MeV	CNR increase by a factor of 2.6
Robar et al. (2012)	7.6 mm graphite	2.35 MeV	Greater reduction of dose with field collimation compared to 6 MV
Parsons and Robar (2012a)	7.6 mm carbon, 6.7 mm aluminum	1.85 to 2.35 MeV	CNR increase by factor ranging from 2.2 to 9.7

[a] All studies compared to 6 MV, with the exception of Tsechanski et al. who compared to 10 MV.

1.6 Stereotactic radiotherapy and radiosurgery

Stereotactic radiosurgery (SRS) and radiotherapy (SRT) are highly precise radiation therapy techniques involving the conformal delivery of a high dose of radiation to a small, well-defined target volume. SRS refers to the delivery of a single fraction of high dose radiation, whereas SRT is delivered in several (i.e. less than five) fractions. The indications for SRS and SRT include intracranial malignant and benign tumors, vascular

malformations, and functional disorders[28]. Compared to conventionally fractionated external beam treatments that deliver less dose per fraction, healthy tissue sparing is highly emphasized for patients undergoing stereotactic treatments in order to avoid induction of secondary cancers and/or loss of function. Due to the risks associated with the geometric miss of ablative SRS doses, special care is taken to ensure precise delivery including the use of dedicated machines tuned within strict mechanical tolerances, dedicated immobilization devices, and high-resolution image guidance systems.

Healthy tissue sparing in SRS is accomplished by using many small beams, incident from various angles, all converging on the target volume[29]. This technique provides adequate dose homogeneity and conformality at the target, while minimizing the dose to the proximal normal structures and healthy tissues. In treatment planning, stereotactic beams are selectively placed to avoid entry and exit dose through delicate structures while meeting the required dose coverage, as informed by the anatomy and planning objectives. These beams are shaped using precisely machined conical collimators (4 mm – 25 mm in diameter) or multi-leaf collimators which act to transmit dose through the open aperture while shielding the anatomy outside of the aperture.

1.6.2 Brief History

Stereotactic principles were introduced to the field of radiation therapy in the 1950s-60s with Lars Leksell's invention of the Gamma Knife as means of treating cranial diseases that were inoperable with classic surgery. Stereotactic techniques utilize a three-

dimensional coordinate system to localize and target anatomical structures using medical imaging to identify the treatment volume. These coordinates were registered to an external frame which was secured to the patient's skull and bolted to the treatment table to ensure accurate patient positioning and prohibit motion throughout treatment. The Gamma Knife consists of ~200 Co-60 sources arranged in a hemispherical array, transmitting radiation towards the patient through narrow collimators. This technology allowed precise specification of ablative radiation doses to small treatment volumes while shielding the surrounding healthy tissue.

SRS was developed on linear accelerators with the invention of linac-compatible frames and collimation in the 1980s[30], allowing widespread accessibility to treatment. In addition to increased accessibility, the integration of SRS on linear accelerators led to expansive research and development of less invasive immobilization devices to improve patient comfort. The invention of high definition multileaf collimators (HDMLCs) offered an alternative collimation method to stereotactic cones which allowed intricate shaping of radiotherapy fields and thus more customized dose specification. The development of specialized machines with high mechanical precision and high dose rate capabilities, dedicated image guidance systems, and advanced treatment planning techniques bolstered the growth of modern linac-based stereotactic treatments; delivered with a frameless immobilization system, using image guidance to monitor and correct for intrafractional motion. Parallel to the development of technologies to support linac-based SRS, the indications of this treatment modality expanded to include extracranial sites with stereotactic body radiation therapy (SBRT).

While the adoption of linac-based SRS has vastly expanded the field in many ways, it also represents a paradoxical shift from implementing low-energy gamma radiation with Co-60 (i.e. with an average energy of 1.25 MeV) to prioritizing higher energy beams, most commonly 6 MV. Despite 6 MV being long regarded as the ideal radiotherapy treatment energy[31], previous studies have shown that lower MV energy photons are advantageous in stereotactic treatments due to the decreased lateral scatter of secondary electrons[29,32]. This is illustrated in the comparative dose distributions from Ding and Homann in below, where the 2.5 MV beam demonstrates sharper dose fall-off compared to the higher energy treatment beams.

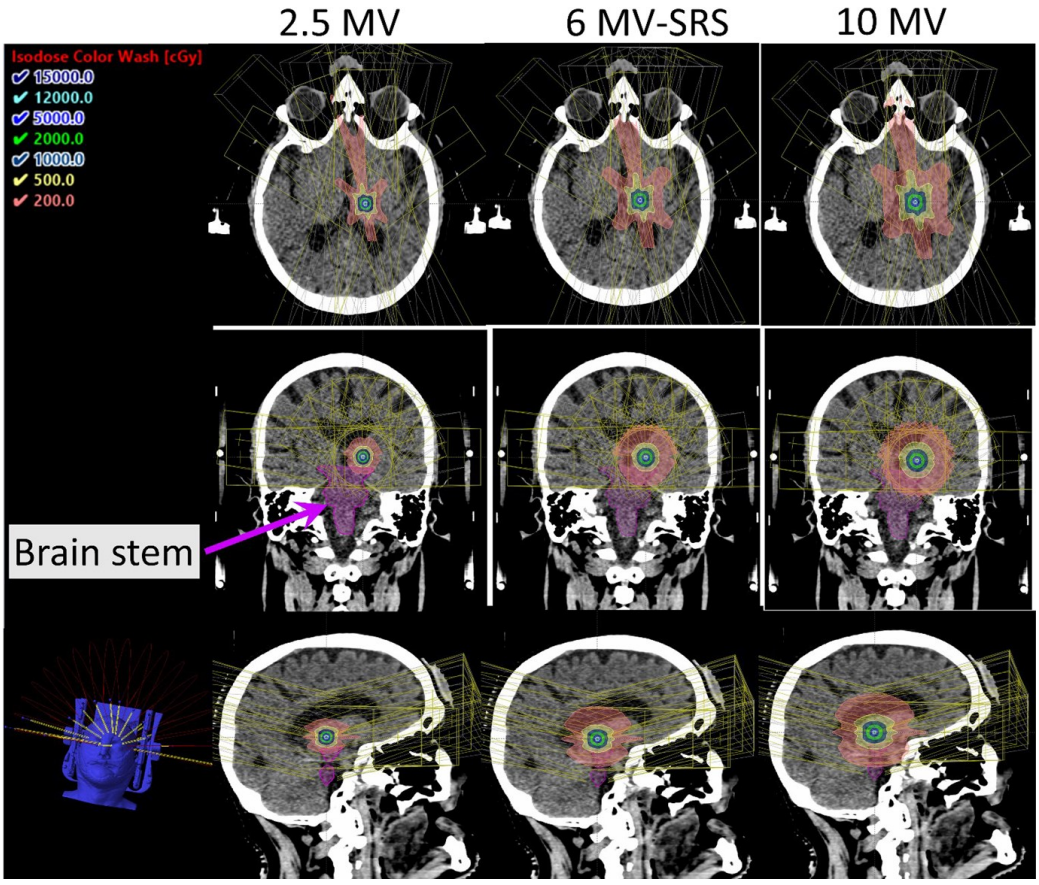

Figure 3. Comparative dose distributions for thalatomy plan from Ding and Homann

The recently commercialized Zap-X (Zap Surgical San Carlos, CA) radiosurgical platform exploits this advantage, utilizing a 3 MV beam for intracranial SRS treatments[33]. Motivated by the same theory, recent studies[34–36] have investigated the 2.5 MV beam on the TrueBeam platform for potential treatment applications in standard and stereotactic treatments. Despite this beam being intended for imaging, both studies demonstrated a dosimetric advantage compared to the 6 MV beam in terms of improved dose fall-off, due to the decreased lateral scatter of secondary electrons.

1.6.3 Common treatment sites

The indications for SRS and SRT are intracranial including both malignant and benign disease as well as vascular malformations and functional disorders. The most common malignancy treated with this modality is brain metastases[37], cancerous tumors which present in the brain with primary origins in different tissue. Other common indications include trigeminal neuralgia, meningiomas, schwannomas and arterial venous malformations[38]. While benign tumors do not possess the metastatic potential seen with malignancies, these abnormal growths impinge upon surrounding healthy tissue posing risk of loss of function. For example, the presence of an acoustic neuroma growing in the inner ear may interfere with hearing and balance. In addition to cancerous growths, SRS and SRT are commonly employed in the treatment of functional disorders, such as trigeminal neuralgia to alleviate pain.

High radiation doses are delivered to these disease sites with the goal of ablating the pathology with a non-invasive intervention. While stereotactic collimation and volumetric

modulation techniques allow spatial specification of dose to minimize the dose to healthy tissue, dose delivery outside of the treatment volume is unavoidable due to the entry and exit paths of the beam as well as scatter. To avoid causing inadvertent injury to normal brain tissue, beam placement is determined using an optimization approach to manage the trade-offs between delivering adequate dose to the treatment volume and abiding by dose limits for surrounding organs at risk based on user input priorities. Generally, the same structures are of concern for all intracranial treatments, mainly the brainstem, optic pathway, cochlea, pituitary gland, lacrimal gland, and hippocampus[39]. The amount of dose these structures can tolerate varies based on different organ sensitivities. Dose limits are specified either in terms of a maximum point dose or dose volume constraints (i.e. a certain sub-volume of the organ can receive a maximum dose), depending on the organ's classification as serial or parallel.

1.7 Ocular Melanoma

1.7.1 Prevalence of ocular melanoma

Ocular melanoma, also known as uveal melanoma, is a rare form of cancer occurring in the eye, mainly the uvea. The incidence rate of ocular melanoma is estimated at 4-7 cases per million[40–42]. Although rare, ocular melanoma is the most common non-cutaneous melanoma[42], whose diagnosis presents poor visual and overall prognosis[41]. Those diagnosed with ocular melanoma face a 50% risk of developing distant metastases[40], commonly manifesting in the liver (95%), lung (24%), bones (16%), and skin (11%)[41]. The ultimate goal of treating ocular melanoma is maintaining visual acuity and preventing

metastasis[43]. As such, modern treatments are mainly eye-preserving rather than enucleation, commonly involving radiation therapy[41,42].

1.7.2 Ocular melanoma treatment

There are several radiation therapy modalities employed in the eye-preserving treatment of ocular melanoma; including plaque brachytherapy, SRS/SRT, and proton beam therapy[41]. The selection of one of these modalities is based on the site of origin, tumor size and location, age of the patient, the presence of extraocular extension, as well as socioeconomic variables (i.e. accessibility to treatment and cost). Currently, plaque brachytherapy is the most widely used eye-preserving radiation therapy treatment for ocular melanomas[44].

While plaque brachytherapy is most common, linac-based stereotactic treatments offer certain advantages over both plaque brachytherapy and proton beam therapy in treating ocular melanomas. Compared to plaque brachytherapy, linac-based stereotactic treatments are less invasive and are shown to produce similar tumor control[42]. Compared to protons, stereotactic-capable linear accelerators are more widely available than proton therapy machines, making treatment more accessible and cost-effective. Previous studies demonstrated comparable dose conformality[45] and local control rates[42] for ocular melanomas treated with photons compared to protons. Due to the proximity of structures in the ocular pathway, sharp dose fall-off is emphasized in stereotactic treatment of ocular melanoma to maintain visual acuity and quality of life.

1.8 Trigeminal Neuralgia

1.8.1 Prevalence of trigeminal neuralgia

Trigeminal neuralgia is a benign condition characterized by episodic unilateral facial pain which presents as a shocking or stabbing sensation and can be triggered by light touch[46]. The onset and termination of trigeminal neuralgia episodes are abrupt, typically lasting one second up to two minutes[47] and may be onset by hair combing, shaving or a cold gust of wind[48]. While trigeminal neuralgia is rare, with a lifetime prevalence of 0.16%-0.3% and an annual incidence of 4-29 cases per 100,000 people[47], it is the most common type of neuralgia[48]. Trigeminal neuralgia is more prevalent among women[46,47] with an incidence ratio of 3:2 (female:male)[47].

Trigeminal neuralgia is commonly experienced in one or both of the lower maxillary and mandibular branches of the trigeminal nerve, which feed into the lower part of the face[48]. As such, the neuralgic sensations are often concentrated near the jaw[46]. The debilitating pain interferes with fundamental activities of daily living such as eating/drinking and oral hygiene,[47] and can greatly affect one's quality of life. Those experiencing trigeminal neuralgia have an increased prevalence of anxiety and depression,[46] and a higher risk of suicide[46,47].

1.8.2 Trigeminal neuralgia treatment

The primary treatment for trigeminal neuralgia involves a low dose of antiepileptic drugs[46,47], however, surgical intervention may be needed for those who are ineligible or

unresponsive to drug therapies[47]. The three types of 'surgical' treatments available can be categorized as 1) invasive and non-ablative, 2) invasive and ablative, and 3) non-invasive and ablative[47]. While the first two treatment options involve classic surgery, non-invasive and ablative techniques describe SRS treatment. Microvascular decompression, an invasive and non-ablative treatment, serves as the standard of care for most patients experiencing trigeminal neuralgia[47]. SRS is employed for those who are ineligible for microvascular decompression due to the use of anesthesia[49]. While SRS treatment for trigeminal neuralgia is generally secondary to microvascular decompression, this treatment provides the least invasive procedure performed in an outpatient setting. Though non-invasive, SRS management of trigeminal neuralgia poses radiotoxicity risks to the surrounding healthy tissue, particularly the brainstem which is frequently abutting the treatment volume. To avoid damage to the brainstem, high dose fall-off is essential to reduce imposed complications, motivating our investigation of a novel beam to improve penumbra.

1.9 Research objectives

The primary goal of radiation therapy treatment is to deliver a lethal dose to the target volume while minimizing the dose to surrounding healthy tissues. In pursuit of this goal, modern radiation therapy utilizes advanced delivery techniques combined with image guidance to achieve safe and effective treatment. The work contained in this thesis is motivated by the postulates discussed in section 1.1, with the goal of improving the radiation therapy treatment workflow using a novel 2.5 MV sintered diamond target

beam. The aim of this research is two-fold: 1) to improve the current 2.5 MV image contrast on the TrueBeam platform using a low-Z sintered diamond target and 2) to investigate the use of the novel 2.5 MV beam for stereotactic treatment applications.

The purpose of this thesis was to investigate a novel 2.5 MV low-Z sintered diamond target beamline on the TrueBeam platform. The implementation of the sintered diamond target was carried out in two distinct phases using: (i) a preliminary experimental setup utilizing a target placed in the carousel of the linac and (ii) a clinical MV beamline setup with the target placed in the target arm. Due to the increased population of low-energy photons in our beam, we hypothesized that our novel beam would offer dual image quality and dosimetric benefits in terms of improved CNR in MV beam's-eye-view imaging and sharper dose fall-off in stereotactic treatments compared to commercially available beams. Contained in this thesis is an anthology of three manuscripts examining the image quality and dosimetric benefits of the novel beam; specifically quantifying the improvement in image quality compared to commercially available beams as well as the dosimetric advantages of the experimental low-energy beam in stereotactic treatments. These broad objectives were addressed as follows in the enclosed manuscripts.

The first manuscript is provided in Chapter 3, addressing the preliminary carousel-mounted target beam setup, the design and installation of the low-Z target placed in the target arm of the linac, and the **planar** image quality characteristics of the novel beam. While low-Z targets have been extensively studied on previous platforms, this study marks

the first implementation of a low-Z target on a TrueBeam unit. The corresponding citation to this manuscript is:

Borsavage, J.M., Cherpak, A., Robar, J.L., Investigation of planar image quality for a novel 2.5 MV diamond target beam from a radiotherapy linear accelerator. *Physics and Imaging in Radiation Oncology*, vol. 16, pp. 103-108, 2020.

The second manuscript is included in Chapter 4. Manuscript 2 presents an organic continuation of the previous, addressing the **volumetric** image quality characteristics of the 2.5 MV low-Z beam. In addition to conventional volumetric imaging which captures the full field of view, this article examines the improved image quality and dose sparing capabilities of volume-of-interest imaging which collimates the beam to only the relevant anatomy for the image guidance task. The corresponding citation for this manuscript is:

Borsavage, J.M., Cherpak, A. J., Robar, J. L., Improving image quality and reducing dose with 2.5 MV diamond target volume-of-interest cone beam CT imaging. *Medical Physics*, vol 49., no. 12, pp. 7661-7671. 2022.

The third manuscript is presented in Chapter 5, addressing the therapeutic potential of the novel 2.5 MV low-Z target beam. This manuscript investigates the dosimetric characteristics of the 2.5 MV low-Z beam in small stereotactic fields and the dose-sparing advantages of 2.5 MV low-Z SRS/SRT compared to standard treatment beams. Using a 4 mm stereotactic cone and comparable MLC field for collimation, this article examines the clinical implications of reducing the radiological and/or geometric components of

penumbra via Monte Carlo methods to simulate treatments of ocular melanoma and trigeminal neuralgia. This manuscript, titled 'Investigation of a novel 2.5 MV sintered diamond target beam for intracranial linac-based stereotactic treatments' has been accepted for publication in the journal Biomedical Physics & Engineering Express.

Chapter 2 Theory

2.1 Megavoltage photon beam production and shaping in c-arm linear accelerator

A linear accelerator (linac) is a radiation producing device used in radiation therapy to deliver an external beam of ionizing radiation to treat cancers as well as benign conditions. Beams are generated by accelerating electrons to high megaelectron volt (MeV) energies using high power microwaves through a linear accelerating waveguide. The linac can be used to treat superficial lesions using an electron beam, or for treatment at depth using a photon beam. Photon beams are generated through a process known as bremsstrahlung, by bombarding a high atomic number target with high energy electrons, which will be discussed in greater detail in the following subsection.

The beam-forming components of a linac include a power supply, a microwave source, an electron gun, an accelerating structure, a beam transport system, and beam collimating systems[50]. A block diagram illustrating these components is provided in Figure 4 below.

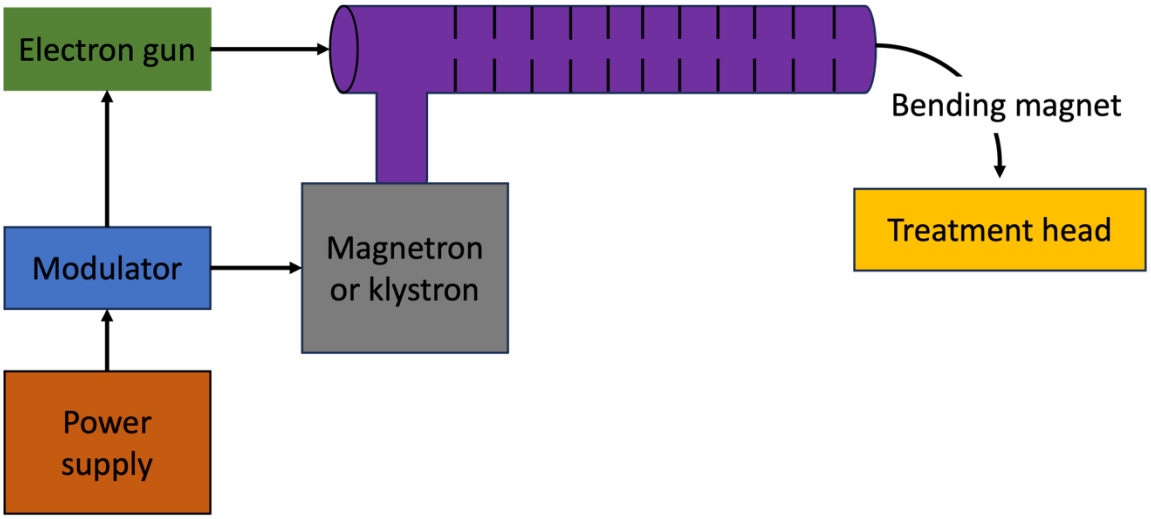

Figure 4. Block diagram of linear accelerator beam-forming components

The power supply provides DC power to the modulator, which contains the pulse-forming network that manages the timing schedule of microwave and radiation injection into the accelerating structure. This network produces simultaneous short, high-voltage, DC pulses supplied to both the magnetron/klystron and electron gun. The pulsed voltage to the magnetron or klystron produces pulsed microwaves which are transmitted to the accelerating structure via the waveguide. The electron gun produces a stream of electrons through thermionic emission, whereby electrons are boiled off a heated filament. These electrons are pulse injected into the accelerating waveguide, synced with the pulse injection of microwaves, as timed by the modulator. In the accelerating waveguide, the electrons are accelerated by the sinusoidal electric field of the high frequency microwaves. The beam of electrons emerging from the accelerating waveguide is deflected using a bending magnet to direct the beam towards the beam shaping structures contained in the treatment head[51]. In the case of photon radiotherapy and MV

imaging, as is the focus of this thesis, the bent beam is focused onto a target for photon production before propagating through the collimation systems in the treatment head.

A linac is composed of five major components, including the gantry, gantry stand, modulator cabinet, treatment couch and control console[50]. The gantry stand performs two major functions, serving as a physical anchor for the rotating gantry as well as housing the microwave power generator used in particle acceleration. The gantry rotates around a horizontal axis which coincides with the positioning of the treatment couch. The collimators which shape the beam rotate in a vertical axis as the gantry rotates. The point at which these two rotational axes intersect describes the isocenter. The treatment couch, upon which the patient is setup, translates in 3 dimensions and rotates around the central axis of the treatment beam. The modulator cabinet contains the power supply circuity which powers the linac. Located outside of the treatment room is the control console, the area which is occupied by the radiation therapists to enable treatment delivery[51]. An image of a linac including the gantry, gantry stand and treatment couch is provided in Figure 5.

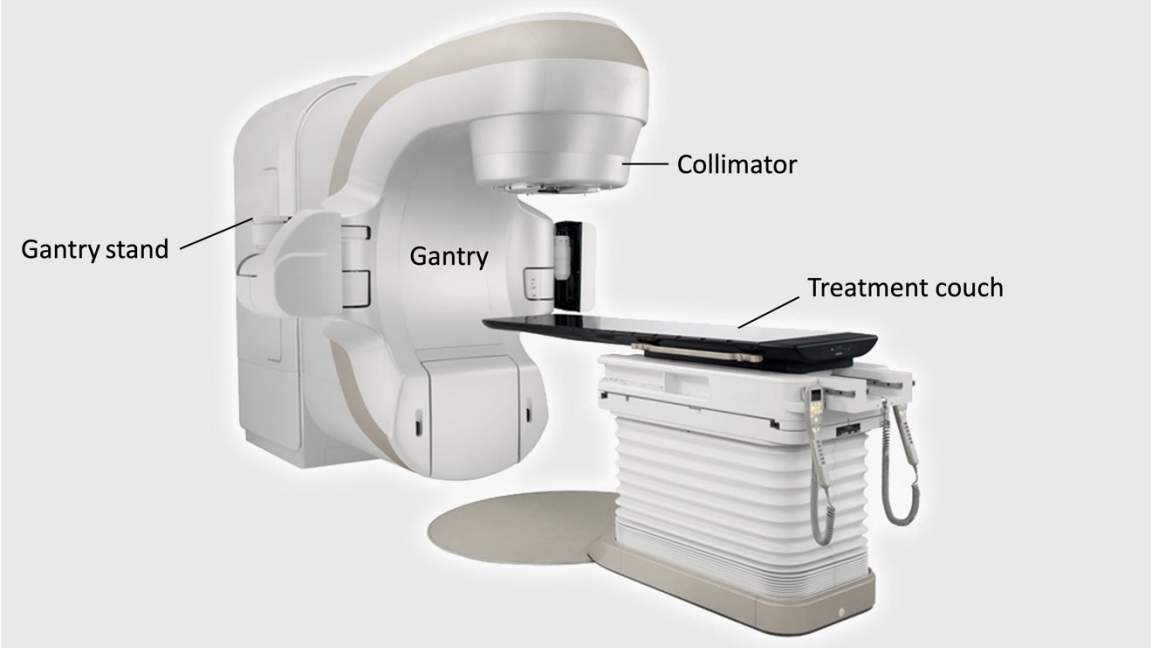

Figure 5. Image of a typical linear accelerator illustrating the gantry, gantry stand, collimator and treatment couch (image adapted from IAEA[52])

2.1.1 Bremsstrahlung x-ray production

Megavoltage photon beams are produced in the treatment head of a linear accelerator by a process known as bremsstrahlung, which translates from German to "braking radiation". Bremsstrahlung is a radiative process resulting from electrostatic interactions between incident high-energy electrons and the nuclear field of atomic nuclei[53].

The conditions under which bremsstrahlung becomes relevant requires that the impact parameter, which describes the proximity of the incident electron to the target nucleus, must be less than the atomic radius. Under these circumstances, bremsstrahlung is possible but rarely occurs (i.e. 2-3% occurrence). Roughly 98% of the time the electron will undergo an elastic scattering event[50]. The kinetic energy lost by the electron is

emitted as a photon[53], as demonstrated by Figure 6. In a linac, a beam of electrons is accelerated to a desired MeV energy before being bombarded into a bremsstrahlung target. Due to the coulombic interactions between the incident electrons and the nuclei of the target material, a beam of photons emerges from the downstream side of the target.

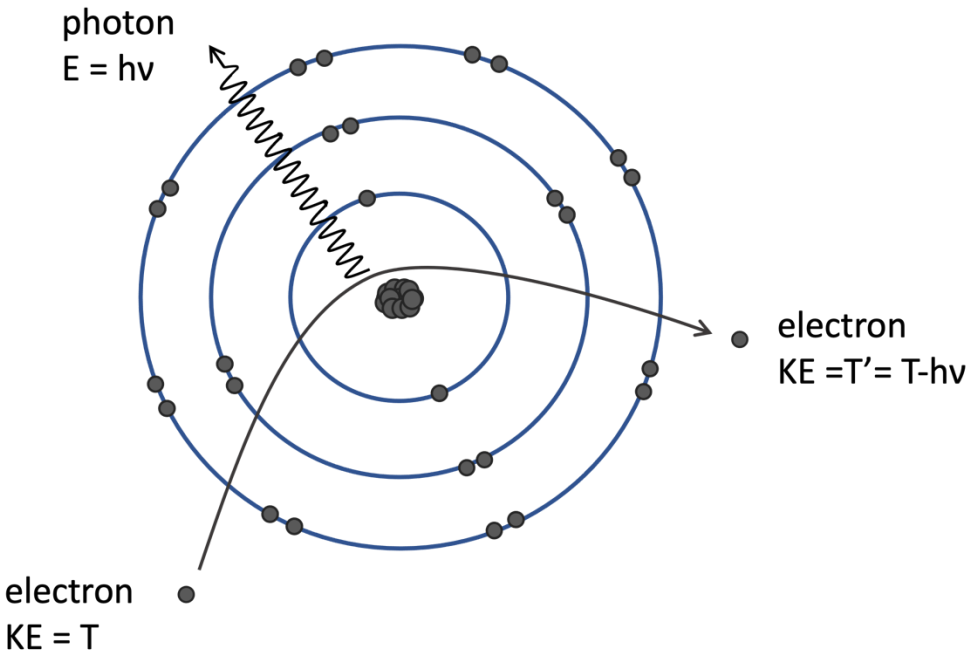

Figure 6. Illustration of bremsstrahlung process

The composition of these bremsstrahlung photons forms a beam containing a continuous spectrum of photon energies ranging from 0 to the energy of the incident electrons. The amount of energy transferred from the electron undergoing a bremsstrahlung event is related to the size of the impact parameter. The smaller the impact parameter, the more energy transferred in a bremsstrahlung event, producing a higher energy photon[50]. The energy spectrum and angular distribution of bremsstrahlung photons exiting the target is

characteristic of the energy of the incident electron beam and the target material. In general, the bremsstrahlung production cross section is proportional to Z^2E, meaning that the x-ray yield increases for higher atomic number materials and greater incident energy[53]. While this Z^2 dependence is observed for the overall bremsstrahlung production (i.e. across all solid angles), the bremsstrahlung efficiency in the forward 0-15° range is roughly independent of atomic number [54].

2.1.2 Treatment head components and photon beam shaping

The treatment head of the linac refers to the beamline components downstream of the accelerating waveguide. The treatment head components are illustrated in the diagram in Figure 7. As discussed in the previous section, a photon beam is produced in a linac via bremsstrahlung by bombarding high energy electrons into a target. The photon target is positioned at the top of the treatment head, immediately downstream from the waveguide, from which the high energy electrons emerge. The components of the treatment head situated below the target are mainly involved in dose monitoring and beam shaping.

The dimensions of the photon beam exiting the target depend on the focal spot size of the electron beam incident on the target and the target thickness. In general, MV beams are forward peaked, possessing a larger abundance of photons along the central axis of the beam compared to the periphery[55]. Upon exiting the target, the photon beam is transmitted through the conically shaped primary collimator which defines the maximum

dispersion angle of the beam. Due to the forward-directed distribution of bremsstrahlung photons, the photon beam exiting the target has differential energy fluence across its profile. To create a more uniform beam, the treatment beamline may contain a conical flattening filter, which acts to preferentially absorb more photons in the center of the beam than at the edges. Situated downstream from the flattening filter, the monitor unit (MU) chamber serves as a dose monitoring system[55]. The MU chamber monitors the delivered dose, relative to the machine calibration, in real-time while also serving to monitor the flatness and symmetry of the beam. The MU chamber provides feedback to stop the beam when the desired dose is met or if it detects deviations from calibrated values[50]. Before exiting the treatment head, the photon beam is shaped by a series of collimators, including the jaws and/or multileaf collimators (MLCs). These collimators are made of high-Z material, designed to attenuate the portion of the beam they obstruct. The treatment head contains two sets of parallel jaws, which shape the beam in the x (crossline) and y (inline) directions creating a rectangular shaped field. The MLCs are positioned downstream in the beamline, as the tertiary collimating system. The MLCs consist of two opposing rows of tungsten leaves which move independently to allow complex beam shaping before exiting the treatment head. In addition to the collimation systems housed within the treatment head of the linac, stereotactic cones may also be employed for generating small circular fields in stereotactic treatments. Stereotactic cones are externally mounted to the treatment head placing the collimator close to the surface of the patient[51]. The collimation systems in a linac provide means of shaping the radiation field incident on the patient to specify the delivery of dose to the treatment

volume. At any given gantry angle, the shape of the field formed by the collimators is based on the beam's-eye-view perspective of the treatment anatomy with respect to the surrounding healthy tissues. The aperture formed by the collimators is designed such that the collimators block the healthy tissue while transmitting the radiation toward the treatment volume.

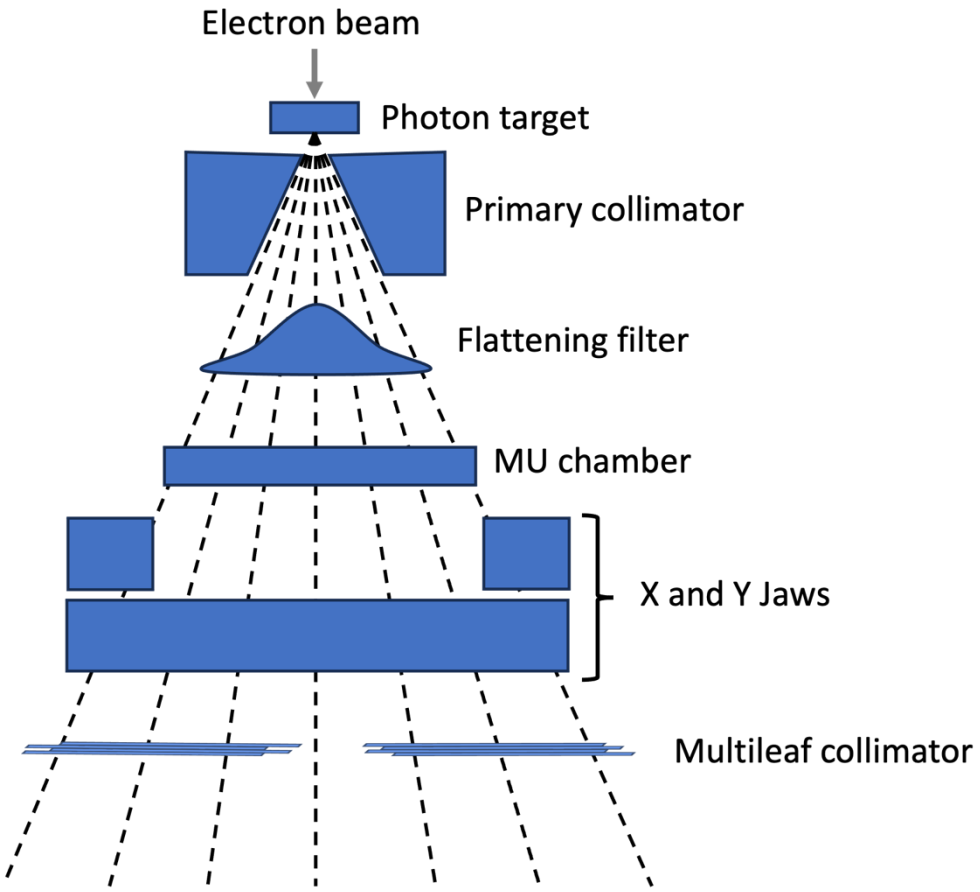

Figure 7. Illustration of the treatment head components in an MV photon beamline of a linac

2.2 TrueBeam imaging systems

TrueBeam (Varian Medical Systems) units are equipped with two imaging systems including MV and kV x-ray imaging. The MV system utilizes the treatment head as an x-ray source with a corresponding digital detector oriented parallel to the treatment head from which the beam emerges. The auxiliary kV source and detector are mounted on the sides of the gantry positioning the kV beam perpendicular to the treatment beam[51]. Modern TrueBeam units feature a designated 2.5 MV imaging beam. With lower energy than the available treatment beams, this beam provides improved contrast-to-noise ratio compared to 6 MV[13,56]. Both x-ray imaging systems are capable of planar imaging, the kV system is also used for volumetric imaging (i.e. cone beam computed tomography (CBCT))[51]. While MV CBCT is theoretically possible, the low detector quantum efficiency (DQE) of the MV imaging panel necessitates a higher dose per projection compared to kV imaging, to achieve useful image contrast and is therefore not used clinically. With the ultimate goal of maximizing image quality and minimizing imaging dose, kV imaging is more commonly used in the clinical workflow of image guided radiotherapy. Despite the advantageous image quality versus dose characteristics of the kV system, the ancillary system introduces increased cost and maintenance[57], and prohibits imaging from the treatment beam's-eye-view. The beam's-eye-view provides a valuable viewpoint in image guidance as it allows visualization of the treatment anatomy with respect to the collimation of the treatment beam[27].

2.3 Image formation and detection in digital projection imaging

The basic components of a modern x-ray imaging system consist of a bremsstrahlung x-ray source and a digital detector. X-rays are emitted from the source and cast on the patient directed toward the anatomy of interest. As the x-rays pass through the patient, they interact with tissues resulting in the partial attenuation of the beam. The beam is attenuated more or less by different tissues (i.e. more so in dense materials like bone than air) creating a differential photon fluence exiting the patient which is characteristic of the tissues through which the beam traversed[58]. The underlying physical mechanisms by which the photons are attenuated are governed by the interaction cross sections of a given material. These cross sections depend on the energy of the particles as well as the atomic number of the material, as explained in the following section. The photon fluence exiting the patient is detected, forming an image representing the tissues through which the beam was transmitted.

The image receptor that detects the exiting fluence can be a direct or indirect detector, utilizing either the primary or secondary fluence, respectively, to generate the resultant image. Direct detectors form an image using the primary fluence exiting the patient (i.e. photons). Indirect detectors utilize an intermediate step to produce charged particles using a scintillator which are then detected for image formation. In digital detectors, this incident fluence is converted into an electrical current by the electronics contained within individual detector elements (dexels). The amount of signal produced in each dexel is proportional to the dose deposited. This signal is read out and represented as

corresponding gray-scale intensity values in the pixels of the image[59]. A cross-sectional schematic of the detector elements in the aS1000 (Varian Medical Systems) flat panel imaging detector used in the MV image acquisitions of this work is included in Figure 8. The aS1000 is an indirect detector composed of a copper conversion plate, a scintillator, and an array (1024x768) of photodiodes with corresponding thin-film transistor (TFT) attached to a glass substrate. Photons incident on the metal conversion plate undergo Compton interactions, producing Compton recoil electrons[60]. The electrons interact with the scintillator to produce visible light which is detected by the photodiode creating a current. The charge is collected and readout when the TFT switch is activated. The amount of collected charge is representative of the dose deposited within each dexel, represented by a grayscale value. The composition of the array of grayscale values forms the image[59].

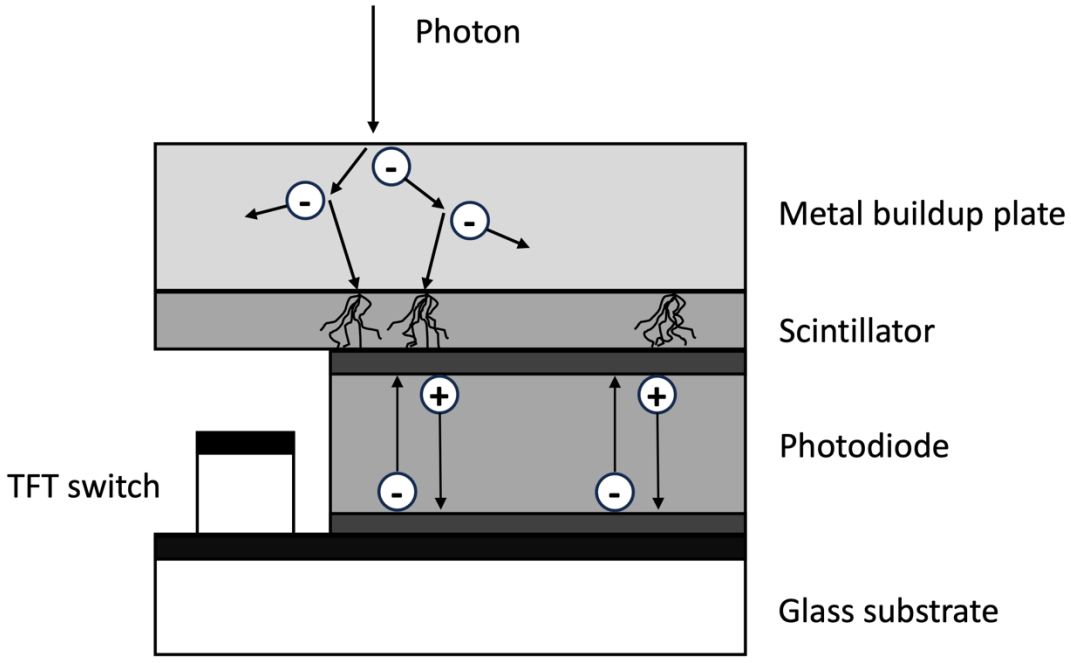

Figure 8. Cross-sectional view of individual detector elements in aS1000 (Varian Medical Systems) detector.

2.4 Photon interactions

As a photon beam traverses a medium, it interacts with the constituent atoms and electrons of the material resulting in the partial attenuation of the beam and the subsequent generation of charged particles. The fraction of photons which are attenuated by a given thickness of material is characterized by the linear attenuation coefficient, μ, expressed in units of inverse centimeters (cm^{-1}) [53]. Since the number of interactions is relative to the number of atoms or electrons present in a given material thickness, the linear attenuation coefficient depends on the density of the material[58]. A more useful representation of attenuation is the mass attenuation coefficient, which is calculated by normalizing the linear attenuation coefficient by the density of the material, μ/ρ and is expressed in units of cm^2/g. The mass attenuation coefficient presents a more convenient metric, as it is constant for a particular element or compound regardless of density (e.g. ice, water and water vapor have different linear attenuation coefficients but the same mass attenuation coefficient). This metric describes the interaction probability within a certain mass thickness of a given material. With units of cm^2 per gram, the mass attenuation coefficient is often interpreted and referred to as a cross section[58], reflecting the effective area of the interaction 'target'[50] seen by the incoming photon. There are several mechanisms by which photons can interact with their surroundings, and thus the mass attenuation coefficient reflects the sum of the partial cross sections contributed by each interaction type.

The main photon interactions that occur in the megavoltage energy range are photoelectric effect, Compton scatter, and pair production. The occurrence of any of these events is stochastic in nature and are thus governed by well-defined probability functions (i.e. cross sections)[53]. The probability of interaction depends on the incident photon energy and the atomic number of the attenuating medium[50]. Figure 9 demonstrates the relative importance of each interaction type as a function of photon energy and atomic number in the ranges of 0.001-100 MeV and 1-100, respectively. The plotted lines in this figure represent the conditions under which the probabilities of interaction types are equivalent, specifically, $\tau=\sigma$ indicates equal probability of photoelectric and Compton events, and $\sigma=\kappa$ indicates equal probability of Compton and pair production events. The regions enclosed by these equal probability lines define the ranges of photon energy and atomic number for which each interaction type pre-dominates. Generally, the photoelectric effect is dominant for low energy photons, Compton dominates at medium energies, and pair production at higher energies[53]. While cross-sections describe the probability of occurrence, each interaction can also be described kinematically, to relate the energies and angles of the participating particles which undergo the interaction[53]. The kinematic descriptions of these interactions are contained in the subsections below.

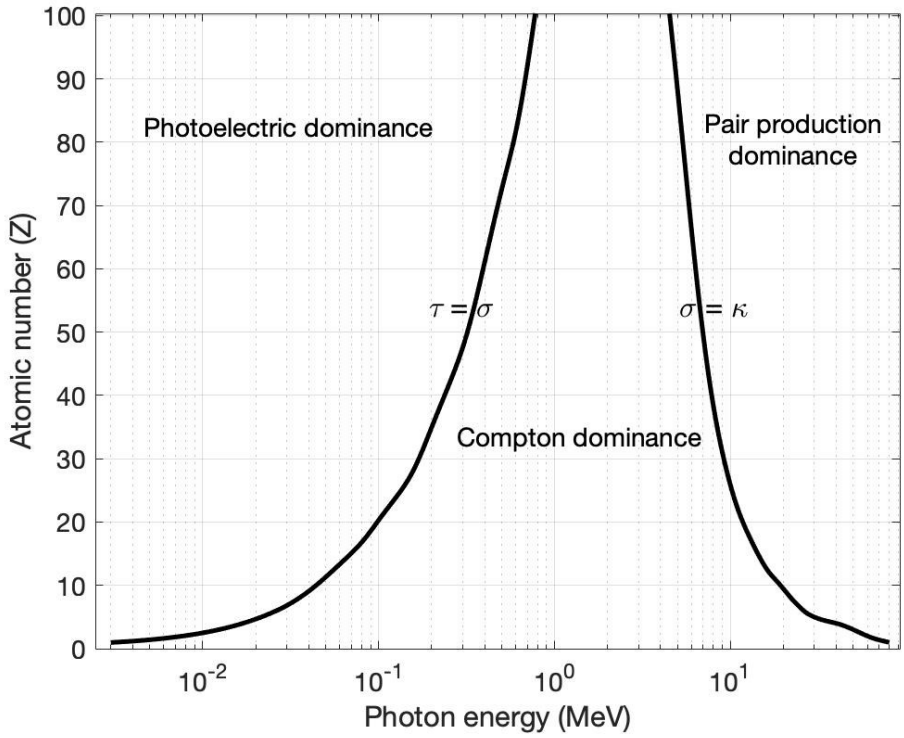

Figure 9. Relative importance of photon interaction types as a function of photon energy and atomic number, demonstrating photoelectric, Compton, and pair production dominant regions. Plotted curves correspond to combinations of hν and Z with equivalent probabilities for photoelectric and Compton interaction (τ=σ) and Compton and pair production (σ=κ).

2.4.1 Photoelectric effect

In the photoelectric effect, a photon interacts with a bound atomic electron causing the photon to be absorbed and the electron ejected from the atom with kinetic energy equal to the incident photon energy minus the electron binding energy (i.e. KE = hν - E_b). The ejected electron, called a photoelectron, travels away from the interaction site at an angle θ, relative to the incident photon's direction[53]. The kinematics are illustrated in Figure 10 below. The photoelectron creates a vacancy in the shell from which it was ejected, which is filled by an electron from a higher energy level. The excess energy, resulting from the difference in binding energies between the two shells, is emitted via fluorescence or

transferred to an outer shell electron. In the case of fluorescence, the atom emits a photon, known as a characteristic x-ray, with quantum energy equal to the difference between the binding energies of the outer and inner shells. If the energy is transferred to an outer shell electron, known as an Auger electron, it is ejected from the atom with energy equal to the energy lost by the electron which transitioned to fill the vacancy (i.e. difference in binding energies between the two shells), minus the binding energy of the ejected electron.

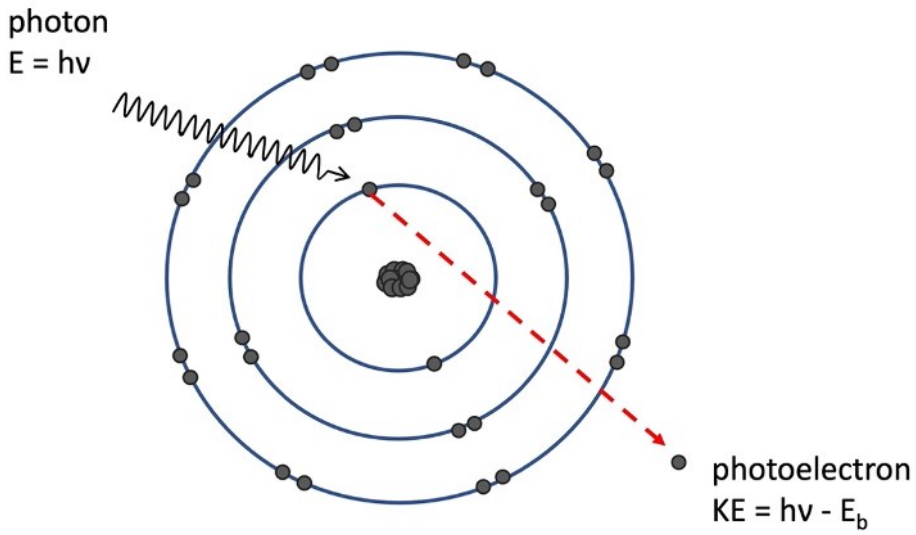

Figure 10. Illustration of the photoelectric effect

The probability of photoelectric interaction depends strongly on both the incident photon energy and the atomic number of the absorbing material. The photoelectric cross section, denoted τ/ρ, is proportional to $(Z/h\nu)^3$; [53] therefore the probability of photoelectric interaction is higher for high atomic number materials and low energy photons. These dependencies are exploited in x-ray imaging which operates in the kilovoltage (kV) energy

range. Due to the Z^3 dependence, tissues with a higher atomic number will attenuate more photons by photelectric interaction than those with lower atomic number, producing contrast between bone and soft tissue.

2.4.2 Compton scatter

Compton scatter describes the process by which an incident photon interacts with a stationary unbound electron, whereby the photon energy is partially transferred to the electron and the rest is scattered. The electron is ejected from the interaction site at an angle, θ, and the photon scattered at an angle, ϕ. The kinetic energy, T, of the electron is equal to the difference between the incident and scattered photon energies (i.e. $T=h\nu-h\nu'$)[53]. The kinematics of Compton scatter are demonstrated in Figure 11 below. Due to the laws of conservation of energy and momentum, the scattering angles and energy transferred from Compton scatter events are confined within theoretical limits. The range of scattering angles for Compton scattered photons and electrons are $0-\pi$ and $0-\pi/2$, respectively[50]. The minimum energy transferred to the electron occurs in a grazing hit, in which the photon continues traveling in the forward direction and the electron is scattered at 90°. For high energy incident photons, the energy of a 90° Compton scattered photon approaches 511 keV. The maximum energy transferred in a Compton interaction is observed in a direct hit. In a direct hit, the electron is set in motion in the forward direction (i.e. $\theta = 0°$) and the photon is backscattered (i.e. $\phi = 180°$). For high energy incident photons, the energy of the scattered photon approaches 255 keV[53]. The solution to the Compton kinematics can be described by three equations which relate the energies

and scattering angles of the particles, as demonstrated in Equations 1-3 below, where m_0c^2 is the rest mass of the electron.

$$h\nu' = \frac{h\nu}{1+(h\nu/m_0c^2)\,(1-cos\phi)} \quad (1)$$

$$T = h\nu - h\nu' \quad (2)$$

$$cot\theta = (1 + h\nu/m_0c^2)\,tan\left(\frac{\phi}{2}\right) \quad (3)$$

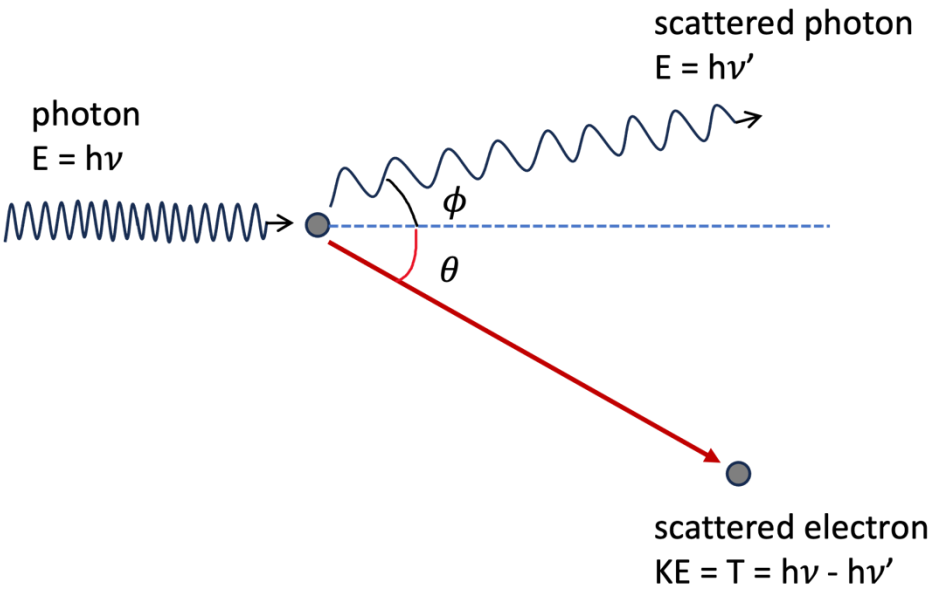

Figure 11. Illustration of Compton scatter

The Compton mass attenuation coefficient, σ/ρ, is independent of Z,[53] as demonstrated in Figure 12, which compares mass attenuation coefficients of water and bone. Unlike the photoelectric effect, the probability of Compton interaction increases with increasing incident photon energy. While Compton scatter is the dominant process in soft tissue in the range of 20 keV-30 MeV[53] (i.e. encompassing the diagnostic energy range), the

Compton mass attenuation coefficient is independent of Z; therefore, tissues of different atomic composition with equal density thickness will attenuate the beam in a nearly identical fashion. Consequently, Compton interactions do not contribute to contrast in x-ray imaging.

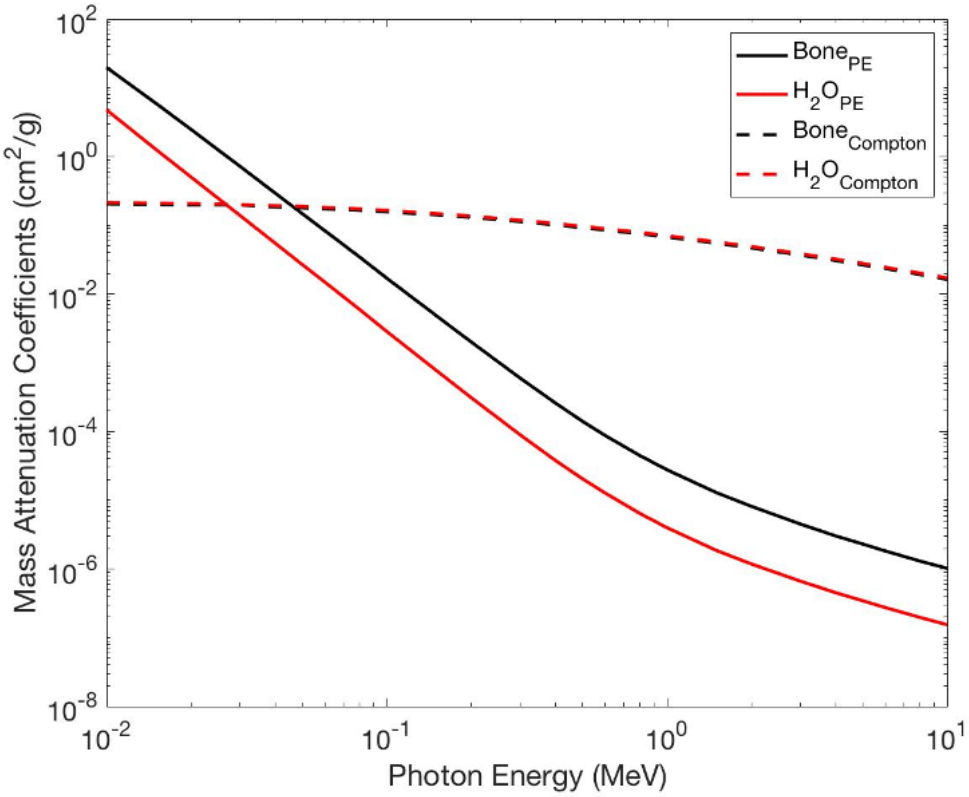

Figure 12. Mass attenuation cross section of water and bone for photoelectric absorption (PE) and Compton scatter across the energy range of 10 keV - 10 MeV.

2.4.3 Pair production

In pair production, an incident photon interacts with the Coulomb field of an atomic nucleus resulting in the total absorption of the photon's quantum energy and the creation of an electron positron pair. The charged particles are ejected from the interaction site creating excitations and ionizations in the medium through which they traverse until they

lose all their kinetic energy and come to rest. Due to the high affinity of these matter and antimatter particles, the positron will combine with an electron and annihilate forming two photons. These two photons are ejected 180 degrees apart from one another, each with energy equal to the rest mass of an electron, m_0c^2 = 511 keV. Due to the conservation of energy, it can be seen that the minimum threshold for pair production is $2m_0c^2$, meaning pair production is not possible for photon energies less than 1.022 MeV[53]. The kinematics of pair production is demonstrated in Figure 13.

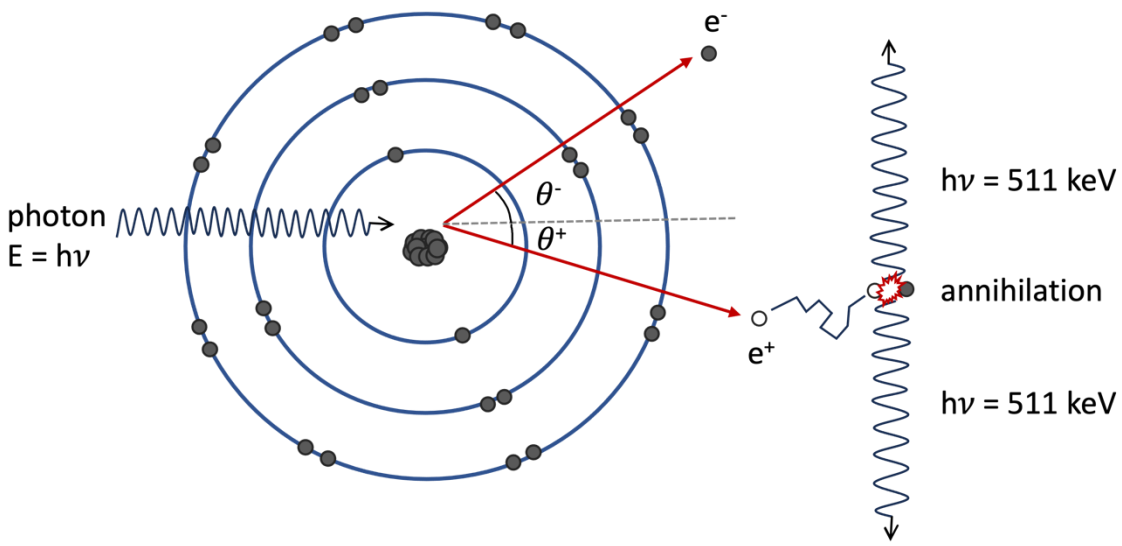

Figure 13. Illustration of pair production kinematics

Though less probable than pair production, this absorption process can also take place in the Coulomb field of an atomic electron, known as triplet production. In triplet production, the target electron is ejected from the atom along with an electron positron pair. The threshold for triplet production is $4m_0c^2$ or 2.044 MeV[53].

The mass attenuation coefficient for pair production, κ/ρ, is approximately proportional to Z. The probability of interaction for a given material increases as the logarithm of the incident photon energy above the threshold. The mass attenuation coefficient for pair production represents the total attenuation coefficient for nuclear and electronic interactions (i.e. $(\kappa/\rho)_{pair} = (\kappa/\rho)_{nuclear} + (\kappa/\rho)_{electron}$) [53].

2.5 Image quality characteristics

The quality of a radiographic image can be characterized in terms of contrast, noise, and spatial resolution. These metrics quantify the visibility of different anatomical structures based on their intensity (i.e. gray-level value) relative to the background and their size. In a diagnostic setting, image quality is an important consideration, as the conspicuity of anatomical features directly impacts the staging of disease and treatment course decisions. While there are many modalities which are used in the field of diagnostic imaging and IGRT, this section is focused on image quality characteristics in radiographic imaging, as is relevant to this thesis.

2.5.1 Contrast

Contrast describes the ability to distinguish anatomical features relative to the surrounding background medium[61]. The contrast in an x-ray image arises from the different attenuation properties of tissues with different atomic compositions (i.e. atomic number and density). Adjacent tissues which are more different in composition will display more contrast – for example, bone versus lung compared to adjacent abdominal

organs. This contrast arises from the difference in photoelectric absorption between materials of differing composition, as explained in the previous section. As such, the average energy of the photon beam is most influential factor which affects contrast[62]. Scattered radiation degrades contrast[62]. In digital radiography, the display contrast can be altered by specifying window level and width to scale pixel intensities for visualizing specific anatomies[61]. The contrast between two regions can be calculated as the difference in the average pixel intensities, as demonstrated by Equation 4, where I is the average intensity in the pixels corresponding to the background (bg) and region of interest (ROI).

$$Contrast = I_{ROI} - I_{bg} \quad (4)$$

2.5.2 Noise

In radiography, noise refers to the information contained in an image which obscure visualization of anatomy or pathology[61]. It appears as random distributions of lighter and darker pixels within an area of uniform material, presenting as a grainy texture in the image[62]. Noise can be quantified as the standard deviation of neighboring pixel intensities within a uniform region[58,61,62]. Image noise is contributed by numerous factors which can be summarized as four major components: structure noise, radiation noise, receptor noise and quantum mottle. Quantum mottle is random, owing to the random variations of photons incident on the detector across the field-oview[61]. These random variations arise from the underlying stochastic nature of x-ray production, interactions, and detection[62], and ultimately results from the finite number of x-rays used to capture an

image[63]. As such, quantum mottle can be reduced by increasing the number of x-rays used to capture an image[61–63]. However, this comes at the cost of increased dose to the patient and should be implemented with caution considering this trade-off. Structure noise arises from the interference of different tissues such as overlapping objects, obstructing the visualization of anatomical features. Structure noise can be reduced by strategic patient setup in 2D radiography or by implementing tomographic modalities. Radiation noise is caused by the detection of unintentional variations in fluence other than quantum mottle, which do not contribute to the usefulness of the image. Where quantum mottle is due to the finite number of photons used to acquire an image, radiation noise results from the detection of scatter. Receptor noise is produced by nonuniformities in the sensitivity of the image receptor across the active detector surface[63]. While there are ways to reduce the contributions of noise in radiography, noise will always be present due to the stochastic nature of the underlying particle physics[58].

2.5.3 Contrast-to-noise ratio (CNR)

To best describe the visibility of a given feature, it is helpful to quantify contrast with respect to the noise present in the image using the contrast-to-noise ratio[62]. This commonly used metric considers the difference in pixel intensities between two regions relative to the noise contained within each, as described by Equation 5 where *ROI* is a region of interest in the image, *bg* represents a region of uniform background material, *P* is the average pixel intensity and σ^2 represents the variance in the corresponding regions.

$$CNR_{ROI} = \frac{|\bar{P}_{ROI} - \bar{P}_{bg}|}{\sqrt{\sigma_{ROI}^2 + \sigma_{bg}^2}} \quad (5)$$

Since quantum mottle decreases with increased photon fluence, the achievable CNR increases with dose. While it is be possible to improve CNR with increased dose, the goal is to avoid unnecessary radiation dose to the patient following the concept of ALARA (as low as reasonably achievable) to prevent radiotoxicity in radiographic procedures. Radiographic techniques are selected to provide the best balance between imaging dose to the patient while maintaining sufficient penetrability and image quality required for diagnosis. In MV imaging, CNR can be improved by implementing a low-Z target to increase the proportion of diagnostic energy photons, thereby exploiting the Z^3 dependence of the photoelectric effect cross section.

2.5.4 Spatial resolution

Spatial resolution describes the ability of an imaging system to reliably reproduce two discrete adjacent objects. Resolution can be measured by imaging a bar phantom which contains a series of alternating high- and low-density line pairs capturing a range of spatial frequencies[62]. The highest frequency pattern that is faithfully reproduced in the image defines the spatial resolution of the system expressed in line pairs per mm (lp/mm), thus representing the smallest object which can be detected by that system. The spatial resolution of an imaging system may be degraded or blurred by several factors including geometric contributions, detector blurring, and motion. The geometric contributions to blurring arise from the finite size of the focal spot and the configuration of the system

with respect to the patient as well as the detector[61]. The focal spot of a radiographic beam describes the area of the anode struck by electrons[59]. The effective focal spot characterizes the size of the projected beam which possesses a region of penumbra at the edges[50]. This penumbra arises due to x-rays arriving from slightly different locations in the focal spot as a result of divergence[61]. Focal spot blur increases with increasing focal spot size. Detector blurring describes the contribution of the finite dimensions of a radiation detector on the ability to resolve small objects. Motion blur is caused by movement during image acquisition which distorts the appearance of the object being imaged. Motion blur can be caused by internal motion such as a heartbeat or from gross patient movement, which can be reduced using immobilization techniques[61]. The modulation transfer function (MTF) is a comprehensive measure of the spatial resolution of a radiographic imaging system that defines the response of the system as a function of input frequency. The MTF is calculated as the ratio of output to input signal modulation, whereby the output signal is degraded due to focal spot blur, motion, and detector blur[61]. Lower spatial frequencies will have higher MTF than higher frequencies. The frequency at which the MTF drops to 50% of that for the lowest frequency is denoted by f_{50}.

2.6 Image guided radiotherapy

Image guided radiation therapy (IGRT) involves the use of one or more imaging modalities to aid in the localization of the target volume and alignment of the patient before or during radiotherapy treatment. In the planning stages of radiotherapy treatment, imaging is employed for delineating treatment volumes and corresponding OARs, to inform

planning decisions and calculate dose[51]. At the time of treatment, pre-treatment images are acquired to help align the patient according to the treatment plan. These pre-treatment images are registered to the planning dataset to identify daily variations in patient setup and/or anatomy and to compensate as necessary[51]. The most commonly prescribed modern IGRT procedure is the acquisition of planar and/or volumetric images prior to daily treatment to verify accurate patient positioning. IGRT is also used intrafractionally (i.e. during treatment) to track motion and automate dose delivery when the treatment volume is in the desired position (e.g. in free breathing treatments for lung cancer). While there are numerous image guidance systems available, the following section will focus specifically on the comparison between MV and kV imaging systems and their applications in IGRT, as applicable to the motivation of this thesis.

2.6.2 MV versus kV imaging systems for IGRT

The earliest form of image guidance for patient setup utilized the MV treatment beam to acquire portal films of the patient[64]. Once developed, the portal films were manually compared to kV radiographs using rulers or templates to determine the necessary shifts in patient positioning. This process was expensive, time consuming, and error prone, driving the development and commercialization of the electronic portal imaging device (EPID) for digital MV imaging in the 1980s and 1990s[64]. Despite the advancement to digital acquisition technology, early EPIDs suffered from extremely low detector quantum efficiency (DQE) (<<1 %), where DQE describes the fraction of incident quanta contributing to the output signal. The low DQE of early EPIDs produced images with high

noise and low signal to noise ratio (SNR)[65], a measure of the average pixel intensity relative to the noise. This issue regarding DQE was improved 10 years later, by the commercial adoption of amorphous silicon (aSi) detectors, currently used today[64]. The DQE of modern aSi EPIDs is roughly 1-2%[66]. The kilovoltage imaging system was incorporated onto linacs in the early 2000s, offering improved contrast characteristics, lower imaging dose and the ability to acquire cone beam CT (CBCT) volumetric image data.

Within the past three decades, many other efforts were made to improve the achievable image quality of the on-board imaging system, including the use of low-Z targets in MV imaging beamlines, and the addition of the auxiliary kV imaging system[65]. While the new kV system improved image quality, it also introduced increased cost and maintenance, as well as additional uncertainties due to the difficulty in aligning imaging and treatment isocenters[57]. Another drawback to the kV system is the inability to acquire beam's-eye-view images, which prevents visualization of the target volume and surrounding structures relative to the collimation of the treatment beam, as the patient is treated[27]. In addition to the geometric advantage, MV imaging demonstrates less susceptibility to high-Z artifacts[51] due to the Compton cross section independence on Z. MV imaging could also provide benefit in the adaptive radiotherapy workflow, which involves the online (i.e. while the patient is on the treatment couch) generation of a treatment plan. Due to the direct correlation between the HU numbers contained in MV images and electron density[51], MV imaging could present an efficient and accurate means of calculating

treatment dose in an adaptive therapy setting. While the kV system offers improved contrast characteristics, the various advantages of the MV system motivate the continued development of MV image guidance.

2.7 Improved MV image quality using low-Z targets

Low-Z targets have been implemented experimentally in MV beamlines to improve the contrast in MV imaging. The achievable contrast in MV imaging is significantly lower than kV imaging due to the higher photon energy spectrum. In radiography, the contrast between tissues of different atomic composition is due to the differential attenuation of the photon beam, resulting in heterogeneous fluence exiting the patient[59], as described in section 2.5.1. The two main interactions by which the beam is attenuated are Compton scatter and the photoelectric effect, with Compton scatter being the dominant interaction in soft tissue across the applicable energy range (i.e. 25 keV- 6 MeV). Since the Compton mass attenuation coefficient is independent of Z, tissues of different atomic compositions but equal density thickness have nearly identical Compton scatter attenuation, as demonstrated by the mass-attenuation coefficients of water and bone in Figure 12. The photoelectric mass attenuation coefficient, however, depends on Z^3, therefore contributing the majority of the contrast between different tissues in x-ray images. Due to the inverse cubic dependence on photon energy, the relative amount of photoelectric interactions that occur in tissue for photons in the MV range is much less than those at kV energies[51] (see Figure 12).

Although MV treatment beams utilize a high-Z target, low-Z targets are advantageous in MV imaging beamlines due to the increased contrast in planar and volumetric imaging compared to a high-Z alternative[14–24]. This improvement in contrast is explained by the increased proportion of diagnostic energy (25 – 150 keV)[17] photons in the beam due to decreased photoelectric absorption within the target. Since the photoelectric mass attenuation coefficient depends on Z^3, the diagnostic energy photons produced in the top of a low-Z target are more likely to exit the target before being attenuated, resulting in a greater yield of kV photons than a beam exiting a high-Z target[25].

Due to the forward-directed angular distribution of bremsstrahlung in MV photon beams, conventional MV treatment beamlines contain a conical flattening filter to preferentially attenuate more low energy photons at the center of the beam than at the periphery, producing a uniform intensity[50,51]. For the purpose of MV imaging, uniform intensity is not of concern; in fact, the heavy filtration of the low energy photons is detrimental to the overall image quality for three key reasons:

1. Diagnostic energy photons have a larger photoelectric interaction cross-section than MV photons; thus, filtering them from the beam results in decreased contrast.
2. Diagnostic energy photons are detected with higher efficiency than MV photons[67]; therefore, the signal-to-noise ratio (SNR) and contrast-to-noise ratio (CNR) will be greater for an unflattened beam than a flattened beam given the same patient dose.

3. The flattening filter is a major source of scattered radiation contributing to the overall image noise and degrading spatial resolution[68].

As such, the ideal low-Z target imaging beamline should be flattening filter free to maximize image quality while minimizing patient dose and exposure times[19].

Prior to the adoption of on-board imaging systems, verification of patient setup was achieved by acquiring portal films using the MV treatment beam. Due to the low detection efficiency of MV photons, and the intrinsically low MV contrast, many efforts were made to enhance portal setup image quality[65]. In 1989 Galbraith introduced a low-Z target into an MV beamline as one of the earliest attempts to improve portal imaging quality[15]. Since 1989, a variety of low-Z targets have been extensively investigated for improved image quality in MV imaging. In 1998, Ostapiak et. al. modified a 6 MV beamline on a Siemens MXE Mevatron unit to implement thin Be and C experimental targets positioned at the top of the X-HI primary collimator. Compared to the conventional 6 MV beam, Ostapiak et. al. demonstrated improvements in contrast by factors of up to 2 times for phantoms less than 15 cm thick, concluding that the low-Z imaging technique is most advantageous in thin imaging geometries such as head and neck. In addition to this groups experimental work, this study investigated the spectral characteristics of low-Z target beams for different target materials including Be, C and Al compared to the target in the commercial beamline. Compared to the low-Z targets, Ostapiak et al. observed a decrease in the energy fluence below 100 keV by two orders of magnitude for the commercial target. Among the low-Z targets, calculated spectra demonstrated the greatest fluence of

photons with energy less than 300 keV for the Be target. However, the effects of this increased fluence diminished with increasing phantom thicknesses; beyond 6 cm thickness Be and C targets produced images with similar contrast. Based on these findings, Ostapiak et al. concluded that carbon would be preferrable to beryllium due to material cost as well as toxicity considerations[17]. A few years later, Flampouri et. al. used Monte Carlo to identify the optimum target for maximizing image quality on an Elekta SL25 unit utilizing a 4 MV beam. This computational study investigated a variety of low- and high-Z target materials including beryllium, graphite, aluminum, titanium, silver and tungsten with CSDA thicknesses, as well as varying thicknesses of aluminum to determine the effect of target thickness on image contrast. Flampouri et. al. observed a decrease in the average energy with decreasing Z, noting that these spectral changes resulted in increased contrast for a phantom thickness of 10 cm. This effect diminished with increasing phantom thickness due to beam hardening. Due to the higher Z, the authors found the aluminum target to be more efficient than lower Z alternatives of the same radiological thickness. Flampouri et. al. concluded that the target thickness had less of an impact on contrast than on bremsstrahlung efficiency. Since contrast improvements for the Be and C targets compared to aluminum were minimal, Flampouri et al. prioritized the gain in efficiency and selected a thin (6 mm) aluminum target for experimental installation. Compared to the conventional 6 MV beam, Flampouri et al. demonstrated an improvement in contrast for the 4 MV aluminum target beam by a factor of 5 times for 1 cm bone in 5 cm water and 3 times for 1 cm bone in 15 cm water [21,22].

In 2009, Orton and Robar investigated 6 MeV electrons incident on a 1 cm aluminum target in the carousel of a Varian 2100 EX platform. The configuration of their experimental beamline on this platform placed the target 9 mm from the Be exit window of the primary collimator. Unlike earlier studies which utilized film/screen imaging detectors, this study investigated low-Z image quality using an a-Si electronic portal imaging device (EPID) for image formation. This work demonstrated an improvement in contrast of up factors ranging from 1.6 +/- 0.1 to 2.8+/- 0.2 across various materials, for the 6 MV low-Z target beam compared to the therapy beam. They additionally calculated contrast as a function of thickness at air/bone interface, noting that though the relative improvement decreases with increasing thickness, at 16 cm depth the low-Z target outperformed the therapy beam, producing images with improved contrast by a factor of 1.7 +/- 0.1. Using Monte Carlo, they calculated spectra for 4 and 6 MeV beams incident on Al and Be targets for comparison with the commercial 6 MV beam. The yield of diagnostic energy (i.e. 25-150 keV) photons calculated from these spectra were 29% for the 6MV/Al beam and 40% for the 4 MV/Be, compared to only 0.3% for the 6 MV therapy beam. Based on Monte Carlo findings, the authors note that the low-Z contrast can be further improved by an additional factor a 1.3 +/- 0.2 by decreasing the incident energy to 4 MeV and removing the Cu conversion layer in the EPID[16] .

Robar et. al. continued the investigation on the 2100EX implementing an additional lower energy 3.5 MV beam generated using a 0.67 cm Al target. This 3.5 MV beam was evaluated against a 6 MV low-Z beam and a conventional 6 MV beam to determine

advantages in volumetric imaging. The 3.5 MV low-Z beam was created by tuning the nominal 4 MV beam to produce the desired energy for photon production. This study demonstrated increases in the contrast-to-noise ratio by factors up to 2.4 and 4.3 for 7 MV and 3.5 MV beams compared to 6 MV in CBCT, with similar improvements in planar imaging. In accordance with other previous studies, the authors reported a significant loss in the low-Z contrast advantage with increasing phantom diameter due to beam hardening. This effect was most significant for the 3.5 MV beam, with the explanation that this was due to the 3.5 MV low-Z beam containing the highest proportion of diagnostic energy photons compared to the other beams, and therefore undergoing the most significant beam hardening. Despite the decreased improvement factor, the authors noted that an advantage remained for the 3.5 MV beam at 25 cm phantom diameter, which displayed contrast improvements by factors of 1.5 and 3.4 for bone and lung inhale regions, respectively, compared to 6 MV. The authors explain that the contrast advantage diminishes with increasing thickness due to beam hardening, owing to the 3.5 MV beam containing the highest proportion of diagnostic energy photons and therefore, the most significant beam hardening. In addition to CNR, this study reported a slight increase in the spatial resolution for low-Z beams which was measured to be 0.5 lp/mm compared to 0.4 lp/mm for 6 MV. The study concluded that the low-Z target approach is expected to be most beneficial for anatomical regions of smaller separation to reduce beam hardening effects. Based on their findings, the authors proposed investigation of lower energy beams to determine achieve further CNR improvements, noting that the design of the waveguide may impede the generation of such a beam[24]. Complimentary to the

investigation of contrast characteristics of low-Z target beams on the 2100EX, Connell and Robar investigated the effect of target atomic number, thickness and incident electron energy on the spatial resolution compared to the 6 MV beam. This study involved the experimental implementation of beryllium, aluminum and tungsten targets with thicknesses corresponding to 20, 60 and 100% CSDA range in each material for both 4.5 and 7.0 MeV incident electron energies. Using Monte Carlo, this group simulated additional thicknesses (10-100%) to determine the effect of target thickness on the achievable spatial resolution. They reported a decrease in f_{50} of the 4.5 MeV/W by 10.4% compared to 6 MV. They expanded their study to include an investigation of a more clinically realistic target placed in the target arm, to decrease focal spot blurring which occurs due to the electron beam traveling through air before impinging on the target. Doing so resulted in increases in f_{50} by 14.5% and 21.5% for the 7 and 4.5 MeV beams with the target placed in the target arm compared to the external target setup. Of all the parameters investigated, the authors found that the positioning of the target within the vacuum system produced the largest improvement in spatial resolution compared to target parameters and incident energy. Connell and Robar suggested that target material should be chosen based on contrast advantages, which favor lower Z materials, rather than spatial resolution considerations, because all target parameter combinations produced comparable spatial resolution to 6 MV[25].

Unlike previous studies which utilized a graphite target, Sawkey et. al. investigated the use of a higher density, sintered diamond target for its dual use with 4 and 6 MV beams.

Their rationale was that the higher density of the sintered diamond would introduce the possibility of using the same target for both beams while maintaining low electron transmission. This study compared the image quality of 4 and 6 MV beams generated using the sintered diamond target to a 4 MV graphite target beam. For low contrast materials, such as trabecular bone and soft tissues, the acquired images demonstrated similar CNR among all three beams. In comparing the two beams generated with the sintered diamond target, Sawkey et al found that the lower energy 4 MV beam produced better CNR than 6 MV. Specifically, Sawkey et al. reported a 25% increase in the CNR of dense bone and lung for the 4 MV beam compared to 6 MV at doses less than 10 cGy. The CNR of dense bone and lung favored the 4 MV graphite target beam over the diamond target beam across the range of doses. However, the three beams produced similar CNR for soft tissue and trabecular bone. Despite the slight differences in the population of diagnostic energy photons among the 4 MV diamond and graphite target beams, the authors conclude that the diamond target provides similar image quality to graphite[18].

Expanding on previous work on the 2100EX, Parsons and Robar examined 2.35 and 1.9 MeV electrons incident on thick aluminum and carbon targets; concluding that the experimental photon spectra contained approximately 50% of diagnostic energy photons, compared to only 0.3% [16] for the clinical 6 MV beam. Percent depth dose measurements for 2.35 MV low-Z beams demonstrated a shift in the depth of maximum dose, d_{max}, by 0.2 cm towards the surface for the carbon target beam compared to aluminum, indicating the creation of a softer photon spectrum. This increase in low energy photons resulted in

an increased CNR ranging from factors of 6.2 to 7.4 for cortical bone and from 3.7 to 4.3 for a thin and a thick phantom, respectively, compared to the 6 MV therapy beam for both experimental target beams[23]. While this group anticipated the greatest CNR improvements for the lowest energy and atomic number target combination, they observed no measurable difference with reducing the energy from 2.35 MV to 1.90 MV or between target materials. Based on their findings, Parsons and Robar suggest the use of a 2.35 MV carbon target beam for further low-Z target investigation[23].

In 2013, Varian proposed a 2.5 MV 'low-X' imaging mode for the TrueBeam 2.0 platform as a commercial solution to improve MV image quality. Before the release of the new platform, Parsons et al. evaluated the proposed low-X imaging beam against two 2.35 MV carbon target beams on the TrueBeam and Clinac platforms using Monte Carlo simulations in VirtuaLinac[69] (Varian Medical Systems) and BEAMnrc (National Research Council of Canada)[70]. Compared to the 2.35 MV carbon target beam on the Clinac platform, Parsons et al. observed a decrease in the relative fraction of diagnostic energy photons by 10% and 28% for the 2.35 MV carbon target and 2.5 MV low-X beams, respectively, on the TrueBeam. The harder photon energy spectra decreased contrast by factors of 1.1 and 1.4 (thin phantom) and 1.03 and 1.4 (thick phantom), for the 2.35 MV carbon target and low-X beams, respectively, compared to the 2.35 MV carbon target Clinac beam[14]. Despite the advances made to the portal imaging system, these recent findings suggest that the current MV image contrast could be further improved; motivating experimental implementation of low-Z targets for the TrueBeam platform.

Review of these low-Z target studies points to low energy electron beams and low-Z materials being preferable in the production of optimal beams for MV imaging. While an imaging specific beam has been commercialized to improve the achievable image quality compared to available treatment beams, Parsons and Robar demonstrated that this beam could be further improved by replacing the copper target with a low-Z (i.e. Z<13) alternative[23]. While carbon has been extensively studied and proposed as the ideal material, Sawkey et al. demonstrated similar contrast characteristics between beams generated with carbon or denser sintered diamond targets. Due to the higher density, sintered diamond offers the advantage of a more compact target which may provide decreased focal spot blur over a thicker carbon substitute[18].

2.8 Radiation dosimetry

Radiation dosimetry involves the quantification of ionizing radiation at a point in terms of absolute dose or related quantities using a radiation-sensitive device known as a dosimeter. Dosimetry is applicable in both imaging and radiotherapy settings. In imaging, dose is managed to provide the necessary image quality for identifying pathology while following the principle of ALARA (i.e. as low as reasonably achievable) to reduce radiotoxicity. In radiotherapy treatment, dosimetry is used for acquiring data used in commissioning treatment planning systems and maintaining machine calibrations, for example, as well as a variety of clinical scenarios to verify dose delivery.

In acquiring dosimetric measurements, the dosimeter is placed at the point of interest, causing a displacement of the surrounding medium in which dose is being measured. Due to the finite size of the detector and the resultant displacement from its insertion at the point of measurement, the dosimeter serves as a surrogate for the medium in which the desired dose is being measured; necessitating means for relating dose in the dosimeter to that in the medium of interest[50]. The fundamental quantities of radiation dosimetry, the basic properties of dosimeters, and the theoretical basis for calculating dose using dosimeters are discussed in detail in the following sections.

2.8.1 Fundamental dosimetric principles

Ionizing radiation interacts with the medium through which it passes, transferring energy to the constituent atoms or molecules. The energy transferred to the medium can be transported away from the interaction site via secondary particles or absorbed locally[58]. The local absorption of energy represents the deposition of radiation dose, where dose is the mean energy imparted within a volume, V, with mass, m, and is expressed in units of Gray (Gy) where 1 Gy = 1 J/kg [50]. Ionizing radiation can be either directly or indirectly ionizing, classified based on the mechanisms by which it deposits energy to its surroundings. Indirectly ionizing radiation refers to uncharged particles such as photons and neutrons, whereas directly ionizing radiation refers to charged particles (i.e. electrons, protons, heavy ions)[71]. This lack or presence of charge influences the behavior and frequency of interactions the particle will experience as it traverses through matter. Electrons, possessing a negative charge, have a high affinity to the Coulomb fields in the

surrounding medium, and therefore undergo many small electrostatic interactions as they traverse matter. Electrically neutral photons are less susceptible to the Coulomb forces of atoms in the surrounding medium and interact less frequently with sizeable distances between interaction sites[72]. Photons interact via photoelectric absorption, Compton scatter or pair production, as described in detail in section 2.4. Each of these interactions results in the partial or total transfer of the photons kinetic energy to a secondary electron generated in the interaction. This secondary electron is responsible for the majority of the energy transferred to the medium, via numerous soft and hard collisions until it loses all its kinetic energy and comes to a stop[53]. The amount of energy transferred to charged particles and subsequently absorbed by a medium is proportional to the number of photons which traverse the medium, as characterized by the fluence, Φ. Likewise, the energy of the incident particles is also influential to the amount of energy transferred and absorbed. The energy fluence, Ψ, describes the amount of energy which passes through an area[58].

Charged particles interact via a series of collisional interactions, where the type of interaction is characterized by the size of the impact parameter, b, relative to the atomic radius, a, of the constituent atoms of the medium. The impact parameter describes the distance between the electron's trajectory and the atomic nucleus. When the impact parameter is much larger than the atomic radius (i.e. b>>a), the electron undergoes a 'soft' collision. A soft collision is an electrostatic interaction between the charged particle and the atom as a whole, causing excitations and sometimes ionizations. In this process,

the charged particle transfers a small amount of energy on the order of a few eV to the atom. Soft collisions are the most probable charged particle interaction; while the net energy transferred in a single interaction is small, soft collisions account for approximately half of the energy transferred to the medium. Hard collisions occur when the impact parameter is comparable to the atomic radius (i.e. b~a). In this case, the incident charged particle interacts with a single atomic electron, resulting in the production of a delta ray (i.e. the electron is ejected from the atom). Though hard collisions occur less frequently than soft collisions, charged particles transfer an appreciable amount of energy per interaction, contributing the same amount of dose to the medium as soft collisions[53].

Photons impart energy to their surroundings in two distinct steps (i.e. indirectly), where energy is first transferred to secondary charged particles as kinetic energy via photoelectric, Compton or pair production, and the charged particles impart energy to the medium via soft and hard collisions[50]. This energy transferred to charged particles via photon interactions is termed KERMA (kinetic energy released per unit mass). The transferred KERMA can be expended by charged particles in two ways, via collisional and radiative interactions. KERMA can therefore be expressed in terms of radiative and collisional contributions depending on how the energy is expended[53]. Collisional interactions produce ionizations and excitations in the surrounding medium, resulting in the local absorption of energy, whereas radiative interactions result in the production of secondary uncharged particles which are transported out of the volume. The energy

imparted to a volume represents the net energy entering said volume minus the energy which leaves the volume, considering mass-energy conversions. In the case of charged particle equilibrium, which exists when an equal number of charged particles are entering a volume as are leaving, absorbed dose is equal to the collision KERMA[53].

While the mass attenuation coefficient describes the probability of interaction for a given photon energy in a particular medium, the mass energy transfer coefficient, μ_{tr}/ρ, describes the fraction of energy transferred to secondary charged particles resulting from a given interaction[51]. KERMA is equal to the product of the energy fluence and the mass energy transfer coefficient, as demonstrated in Equation 6. While this equation is specific to a monoenergetic beam, the principle is the same for a polyenergetic beam, whereby the differential distribution of energies $\Psi'(E)$ is integrated over the range of energies contained in the spectrum.

$$K = \Psi \cdot \left(\frac{\mu_{tr}}{\rho}\right)_{E,Z} \tag{6}$$

Secondary charged particles are responsible for the majority of the dose delivered by photons; however, they do not necessarily impart all of their energy locally, due to radiative losses such as bremsstrahlung or in-flight annihilation. The fraction of energy transferred to secondary charged particles which is locally absorbed is characterized by the mass energy absorption coefficient, μ_{en}/ρ.[51] The collision KERMA can be calculated as the product of the energy fluence and the mass energy absorption coefficient, as shown in Equation 7. The collision KERMA for a polyenergetic beam can be calculated as previously described for the total KERMA, by integration [53].

$$K_c = \Psi \cdot \left(\frac{\mu_{en}}{\rho}\right)_{E,Z} \quad (7)$$

Stopping power describes the expenditure of energy by charged particles per unit pathlength, expressed in MeV/cm. The related quantity, mass stopping power, can be calculated by dividing the stopping power by the density of the medium, producing units of MeV cm^2/g. Stopping power can be subdivided to specify the mechanism of energy loss by the particle, into collision stopping power and radiative stopping power components[53]. The mass collision stopping power is an important dosimetric quantity, as it describes the amount of energy spent by charged particles in collision interactions which are responsible for the majority of the dose deposited by photons.

2.8.2 Basic cavity theory

As mentioned in the previous section, the displacement of the medium resulting from the insertion of a dosimeter necessitates the means of relating the dose measured within the detector's active volume to that in the surrounding medium in which dose is being measured[50]. This issue is addressed via cavity theory, which is employed to determine dose at the point of interest in the absence of the dosimeter[53]. Typically, dose measurements are made using an ion chamber which contains a cavity of air or tissue-equivalent material. Within the cavity is a central electrode which collects the charges liberated by ionizations within the cavity medium. This current is transmitted from the central electrode to an electrometer for readout.

Several cavity theories have been developed to address dose measurement for different cavity sizes, where the size is defined relative to the ranges of secondary charged particles compared to the dimensions of the cavity[53]. Bragg-Gray cavity theory was the first theory developed, which applies specifically to small cavities (i.e. the range of secondary electrons is large compared to the size of the chamber). The two conditions under which Bragg-Gray cavity theory applies are:

1. The cavity must be small compared to the range of incident charged particles to avoid perturbation of the fluence of charged particles in the medium.
2. The absorbed dose in the cavity is contributed exclusively by the charged particles which are crossing it.

The first condition can only be true under CPE or transient charged particle equilibrium (TCPE), and the second assumes that all electrons which contribute to the ionization of the gas originate outside the cavity and completely cross the cavity[50]. Given these two conditions are satisfied, dose to the medium can be calculated using the ratio of unrestricted stopping powers to relate dose to the cavity to that in the medium. This relationship is demonstrated in Equation 8 below, where D_{med} is the dose to the medium, D_{cav} is the dose measured in the cavity and $\left(\frac{\bar{S}}{\rho}\right)_{med,cav}$ is the ratio of stopping power in the corresponding media[50].

$$D_{med} = D_{cav}\left(\frac{\bar{S}}{\rho}\right)_{med,cav} \tag{8}$$

Where Bragg-Gray cavity theory does not account for secondary charged particles created within the cavity, Spencer-Attix cavity theory was developed to address these

contributions. Spencer-Attix requires the same conditions as Bragg-Gray, which under Spencer-Attix cavity theory both apply to the secondary particle fluence as well as the primary fluence. To account for the secondary particle fluence, Spencer-Attix theory makes use of the restricted stopping power instead of the unrestricted stopping power used in Bragg-Gray. The restricted stopping power is smaller than the unrestricted stopping power due to the consideration of an energy cutoff which accounts for delta rays which escape the cavity (i.e. do not deposit their energy locally)[53].

2.8.3 Properties of dosimeters

While there are many types of commercial dosimeters available for use, the physical characteristics of these devices vary widely and must be carefully considered in determining suitability for any given measurement. The six major properties of a dosimeter to consider in selecting a measurement device are: [50]

1. accuracy and precision
2. linearity
3. dose rate dependence
4. energy response
5. directional dependence
6. spatial resolution

The accuracy and precision of a dosimeter refer to the uncertainty attached to a measurement obtained with the device. A device with high precision produces small deviations between measurements and high accuracy ensures measured values are close

approximations of the true value[50]. Linearity describes the proportionality of the measurement quantity to the dosimetric quantity of interest. An ideal detector would provide a linear response across a continuum; however typical dosimeters only display linearity over a defined range of dose. The dose rate dependence of a radiation detector describes the response of an integrating system as a function of the rate of the quantity being measured. It is desirable that the detector's response is dose rate independent such that the ratio of the measured value, M, to the true quantity, Q, is constant. Energy dependence defines the variation of the detector's response to different incident beam energies. The energy dependence is especially important for absolute dose measurements since detectors are calibrated to a standard beam quality and used clinically to calculate dose for different qualities[50]. While there are numerous different dosimeters utilized in radiotherapy, the following section focuses on the operation of the dosimeters used in this thesis, including film, ion chambers, and scintillation detectors.

Film contains photosensitive emulsion which darkens as a result of ionizations produced by radiation interactions. This darkening changes the optical density of the film, which is a measure of the light transmission through the film. The optical density is a function of the dose deposited in the photosensitive emulsion. Typically, film demonstrates linearity over a range of doses which can be determined by creating a sensitometric curve, capturing the change in optical density across a range of known doses. The latitude of film describes the range of dose for which the sensitometric curve demonstrates a linear relationship with dose. The latitude should be considered for the given exposure

conditions to provide contrast across all optical densities[50]. Historically, radiographic film was used for dosimetry purposes, requiring processing to develop and fix the latent image. Radiochromic film is a newer alternative to radiographic film which is self-developing, eliminating the need for darkroom processing. This film contains a photosensitive dye which polymerizes as a result of radiation exposure. Like radiographic film, the polymerization which occurs in radiochromic film changes the optical density of the film as a function of dose. Both radiographic and radiochromic film can be analyzed using a densitometer to measure the spatial distribution of optical densities. This density map can be converted to dose using the sensitometric curve to relate optical density to dose. With proper calibration, radiochromic film provides better than 3% uncertainty in dose calculations[50].

Scintillation detectors are made of photosensitive material which produce visible light as a result of photoelectric interactions within the material. The scintillator is coupled to an optical fiber which transmits the light to the readout electronics. The optical fiber outputs to a photmultiplier tube which converts the visible light signal to electrical output. Contained in the photomultiplier tube is a series of dynodes which act to amplify the signal. The amplified signal is collected by the anode and transmitted to the electrode for scoring[58]. The electron fluence emerging from the photosensitive layer is proportional to the amount of energy absorbed by the scintillator, and thus the size of the electrical signal collected by the electrode is proportional to the energy of the photon which was absorbed by the scintillator. As such, scintillation detectors are capable of distinguishing

between photons of different energy[58]. Commonly, the scintillator used in such detectors are made of plastic which match the radiological characteristics of water within ±2% for clinical beam energies. Plastic scintillator detectors are roughly energy independent and can be made small (i.e. diameter in the mm range) to provide high special resolution[50]. Ion chambers come in a variety of shapes and sizes, but regardless of design, ion chambers commonly possess a gas or liquid filled cavity surrounded by an outer conductive wall. Within the cavity is a central electrode which acts to collect and transmit the measured signal[50]. Secondary electrons entering the cavity produce ionizations within the material occupying the cavity, liberating charges that are collected by the central electrode. The amount of charge collected is proportional to the amount of energy absorbed. The current produced within the central electrode is proportional to the dose deposited, which is readout by an electrometer[53].

2.9 Stereotactic radiosurgery/radiotherapy and radiological penumbra

Although minimized through collimation, dose deposition outside of the treatment volume is unavoidable, due to the entry and exit paths of the beam and the penumbra. The beam penumbra can be defined as the distance between the 80% and 20% or 90% and 10% isodose in a lateral beam profile at a specified depth in water[50]. One factor contributing to the overall beam penumbra is the radiological penumbra, caused by the lateral scatter of primary and secondary particles[58]. Due to the loss of lateral charged particle equilibrium at the field edges, more electrons are scattered outside the field than are scattered inside, as demonstrated in Figure 14.

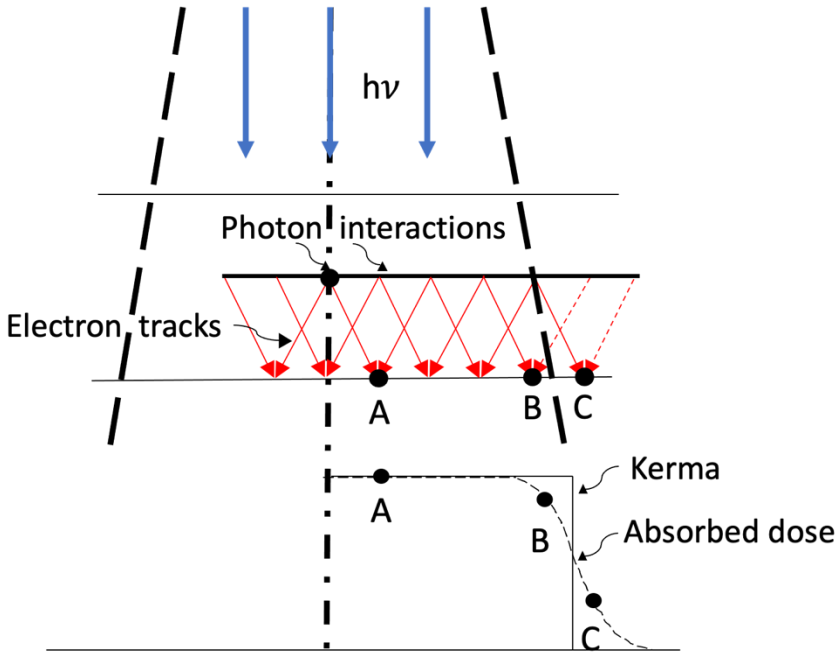

Figure 14. Illustration of the loss of lateral charged particle equilibrium in small fields resulting in increased dose outside of the geometric field and decreased dose at the field boundary.

The lack of CPE results in decreased dose deposited within the field at the boundary, and consequently increased dose deposited outside the geometric field[73]. For standard radiotherapy field sizes, it has been shown that increasing the photon energy from orthovoltage to megavoltage reduces the radiological penumbra due to increased forward scatter[58]. However, for small fields used in stereotactic treatments, the main contribution to the dose deposited is due to the secondary electrons generated by the primary beam. Therefore, by reducing the energy of the primary photons, the range of the secondary electrons is also reduced, resulting in less lateral scatter and sharper radiological penumbra[29,32,73]. This concept has been experimentally validated using a 1 MV treatment beam, in which Keller et al. reported a fourfold reduction in radiological penumbra of a single 5 x 5 mm^2 field, when compared to the clinical 6 MV beam. Keller

et al. expanded their work to examine a complex 18 beam treatment, concluding that the reduced radiological penumbra resulted in superior dose distributions compared to 6 MV in terms of dose fall-off, homogeneity, and conformality[29].

The introduction of the 2.5 MV beam on the TrueBeam platform sparked the interest of several groups on the application of this beam in radiotherapy treatment. While this beam was commercialized with the intention of imaging, the dosimetric characteristics of the 2.5 MV beam motivated the investigation of its use in stereotactic treatment. Using Monte Carlo, Ding and Homann[35] compared dose distributions for identical stereotactic plans delivered with different beam qualities, including 2.5 MV, 6 MV, 6 MV FFF, 10 MV and 10 MV FFF. Due to the reduced range of secondary electrons generated by the 2.5 MV beam, this group demonstrated sharper dose fall-off in a thalatomy case, noting a reduction in the dose to the brainstem by 37% compared to the clinical 6 MV beam[35]. Khaledi et al. investigated the use of the 2.5 MV beam in both standard and stereotactic treatments. Compared to the clinical 6 MV beam, this group observed reduced OAR dose while providing adequate PTV coverage with the 2.5 MV beam[36]. Following the same motive, the recently commercialized Zap-X platform utilizes a 3 MV beam for intracranial SRS. This novel treatment platform is self-shielded and gyroscopic, enabling isocentric intracranial treatment across a 2π steradian solid angle[74]. The Zap-X platform utilizes a rotating collimator system equipped with circular collimators forming field sizes of 4, 5, 7.5, 10.0, 12.5, 15, 20, and 25 mm diameter. Zap-X operates at 1500 MU/min, corresponding to 1500 cGy/min at d_{max} for the largest (i.e. 25 mm) field size[75]. The

reduced energy combined with the shortened source to axis distance of 45 cm of the Zap-X platform provides improved dose fall-off compared to a conventional 6 MV beam. With similar beam quality to Co-60[76], the 3 MV beam demonstrates reduced radiological penumbra compared to 6 MV without the recurring cost of replacing a Co-60 source. Contrary to the convention that 6 MV is the ideal radiotherapy treatment energy[31], lower energy photons may be advantageous in SRS applications due to the reduced penumbra and therefore improved sparing of adjacent healthy tissues.

2.10 Monte Carlo methods

2.10.1 Definition

The Monte Carlo method describes a computational process for modeling probabilistic outcomes of stochastic events using random number sampling of probability distribution functions[77–79]. In the context of radiation therapy, Monte Carlo is used to simulate radiation transport through media, enabling the calculation of macroscopic dosimetric quantities resulting from millions of microscopic interactions[78]. The Monte Carlo framework provides a probabilistic approach to solving numerical integrals which would be impossible to solve with analytical means. The stochastic nature of particle interactions complicates the analytical calculation of particle transport outcomes for three main reasons:

1. The interaction type and outcome of each interaction event is stochastic.
2. Interactions can generate secondary particles, creating more particles to model/track.

3. Each particle can interact numerous times while traversing a medium.

While the underlying particle physics is well understood, the immensity of the problem makes analytical solutions computationally expensive for outcomes of particle transport in radiation therapy applications[77]. Instead, the Monte Carlo method uses random numbers to sample the probability density functions which characterize the likelihood of particle interactions in a given material. This powerful tool allows the simulation of random particle trajectories, or histories, to determine macroscopic outcomes from a cumulation of many particles such as: average distance traveled before interacting in a given medium, the relative occurrence of a given interaction type, dose to a medium for a given beam of particles, etc[77].

The framework for simulating radiation transport using the MC method includes[80]:

1. A random number generator
2. Accurate geometric definition of transport medium
3. Physics input (interaction cross-sections as function of energy and medium)
4. Means of tracking/accumulating results

A random number generator is used to produce the sampling points at which the probability density functions are queried, representing the stochastic nature of particle interactions. The transport medium must be defined spatially and in terms of material composition, specifically the atomic composition of the material as well as it's physical density. The geometric information is required for sampling distance to interaction points, whereas the material composition is used to determine the outcome of any given particle

interaction as dictated by the cross section. Since particle trajectories through the geometry are calculated individually, data logging throughout the simulation is essential to produce cumulative results at the end of the simulation[80].

With these tools, the generic process for MC modelling of radiation transport can be summarized in four steps[81]:

1. Sample random distance to the next interaction site in the current medium from the probability distribution function
2. Transport particle to interaction site (considering geometric boundaries)
3. Sample interaction cross sections to determine interaction type corresponding to most probable event
4. Sample energies and angles of scattered particles to determine next step (if particle is absorbed, repeat 1-4 with next history, if not, repeat 1-4 to simulate trajectories of scattered particles)

This process is repeated for as many histories as defined by the user. Due to the probabilistic nature, results from Monte Carlo calculations represent an approximation of the true value, averaged over the number of histories, including the associated variance. According to the central limit theorem, as the sample size increases (i.e. the number of particles), the distribution of the sample mean approaches a normal distribution[79,81]. Applying this theorem in Monte Carlo methods indicates that increasing the number of simulated particles (i.e. the sample size) decreases the variance, and thus the calculated outcome more accurately represents the true value[80,81]. While it is possible to improve accuracy by increasing the number of histories, the statistical uncertainty decreases with

the square root of the sample size[81–83]. Since calculation time increases proportionally with the number of simulated histories[81–83], increasing the number of histories to achieve the desired uncertainty may not be realistic. To avoid impractically long simulation times, variance reduction techniques (VRTs) may be employed to improve statistical uncertainties without introducing systematic error or increasing the calculation time[77,80]. VRTs improve the efficiency of a simulation, as described by Equation 9 below, where σ^2 represents the variance and T represents the time.

$$\epsilon = \frac{1}{[\sigma(N)]^2\, T(N)} \tag{9}$$

Examples of common VRTs include Russian roulette, bremsstrahlung splitting, and range rejection. In Russian roulette, a survival probability defines a threshold which determines the fate of a given particle type (i.e. photon or charged particle)[81,83]. When such a particle is created, it is assigned a random number between 0 and 1[83]. If the assigned number lies above the threshold probability, the history is terminated without scoring; otherwise, it survives and the particle's statistical weight is divided by the survival probability to avoid introducing bias[81,83]. In bremsstrahlung splitting, each bremsstrahlung photon is 'split' into several independent photons, as defined by the user input splitting number, N_{split}. The statistical weight of each split photon is equal to the incident electron's weight divided by N_{split} to preserve the total weight[83]. Range rejection is a VRT that only applies to charged particles due to their definitive range in any given media (i.e. CSDA range). When implementing range rejection, the maximum range of a given particle in the material being traversed is compared to the shortest distance to the region boundary[83,84]. If the particle's maximum range is smaller than the distance to the boundary then the

history is terminated and scored in the current region. While Russian roulette and bremsstrahlung splitting are true VRTs, range rejection introduces approximations because it does not account for possible bremsstrahlung photons which could have been generated along the electrons path[83,84].

2.10.2 VirtuaLinac

Several standalone Monte Carlo packages are available for modeling radiation transport, including VirtuaLinac[85] (Varian Medical Systems) and EGSnrc (National Research Council of Canada) used in this work. VirtuaLinac is a cloud-based software available (with permissions from Varian Medical Systems) via a secure shell connection to a private Amazon Machine Image launched through Amazon Web Services. VirtuaLinac contains a verified geometric model of the field-independent portion of two commercially available models of Varian linear accelerators, including the Clinac and TrueBeam units. The field-independent portion of the beamline describes the components upstream from the beam-shaping collimators (hence, field independent), from the bremsstrahlung target to a plane above the rectangular jaws. This cloud-based setup allows the maintenance of proprietary design specifications while allowing accurate simulation of beam production on Varian's commercial platforms. The user defines simulation parameters including incident particle, energy, spot size, custom target specification, etc. The output from VirtuaLinac is an IAEA phase space positioned above the jaws, 73.3 cm from isocenter. While the field-independent geometry is exclusive, the geometry of the field-dependent components of the beamline are available through MyVarian[69]. Phase space data

obtained through VirtuaLinac simulations can then be propagated through a subsequent model of the remaining treatment head components and dosimetry media using other Monte Carlo software, such as EGSnrc (National Research Council of Canada) to specify unique transport geometries. This workflow is demonstrated in Figure 15.

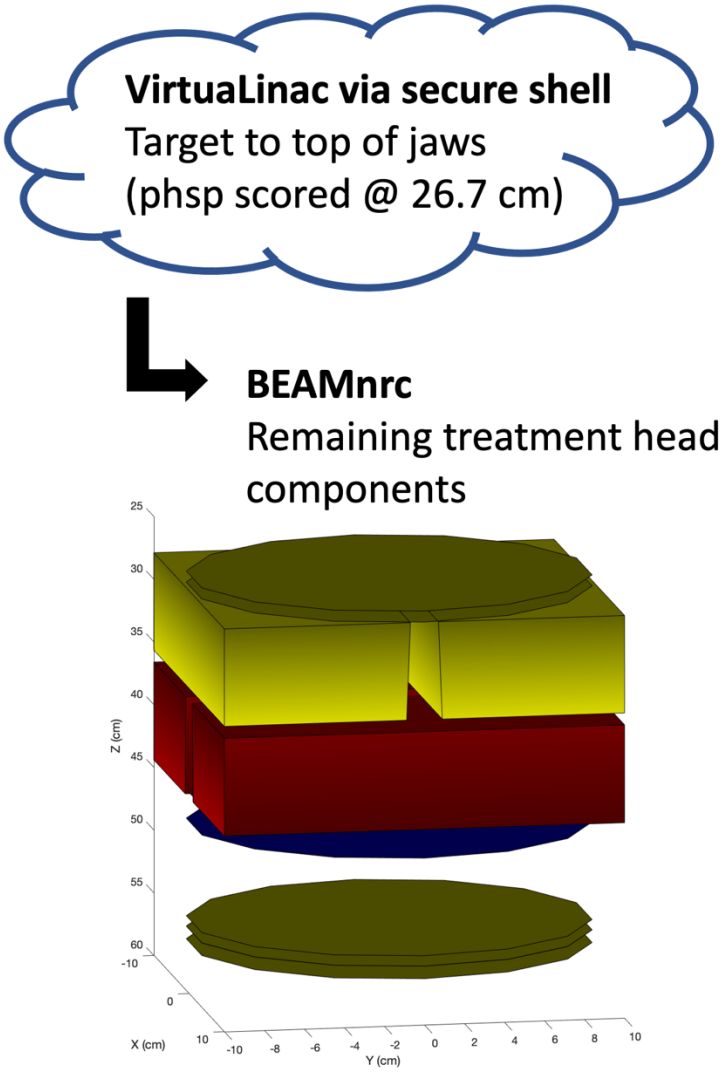

Figure 15. Illustration of Monte Carlo modeling workflow using VirtuaLinac and BEAMnrc.

2.10.3 EGSnrc

EGSnrc is an open-source software for Monte Carlo modeling of radiation transport developed at the Stanford Linear Accelerator Center and maintained by the National Research Council Canada. This software is composed of source files and utilities for constructing geometries, modeling particle transport, scoring outcomes, and analyzing results. In these applications, EGSnrc is capable of simulating particles with energies ranging from a 1 keV to 100 GeV[86]. The subroutines contained in the EGSnrc package define the methods for sampling probability distribution functions which determine probabilistic trajectories and outcomes resulting from radiation interactions which occur as a result of radiation transport through the corresponding geometries. EGS stands for electron gamma shower, alluding to the transport of radiation. The implementation of EGSnrc requires user construction of user code, which may be facilitated by graphical user interfaces. The user code consists of a main program, a scoring routine (referred to as AUSGAB in EGSnrc), and two subroutines defining the geometrical information (HOWFAR and HOWNEAR)[86]. Due to the large number of interactions by which electrons interact with media, EGSnrc implements a condensed history technique[87], which groups several interactions into a single step to improve efficiency. Energy cutoff variables, ECUT and PCUT, define the finite electron and photon energies in which the simulation stops tracking particles. In addition to ECUT and PCUT variables, particle transport is also managed by the PEGS4 material data set which contains the cross section information for particle interactions[88].

The EGSnrc user codes that apply to this work include BEAMnrc and DOSXYZnrc. BEAMnrc is an environment which allows simulation of treatment head configurations using a variety of independent component modules[70]. The results from a BEAMnrc simulation are compiled into a file called a phase space. Phase space data is recorded for each particle which crosses the scoring plane, as defined by the user. The particle energy, position, direction, weight, and site of last interaction is recorded for each particle in the resultant phase space[70]. Phase space data can be used as input to subsequent simulations for dose calculation using the user code, DOSXYZnrc. The dose is calculated in a user defined voxelized phantom, which allows specification of the density and material in each voxel[89]. Phantoms can be constructed to mimic dosimetric setups, such as a water tank or detector, or to replicate anatomy using the user code ctcreate to transform CT data into a voxelized anatomical phantom. A diagram illustrating the workflow in EGSnrc is provided in Figure 16.

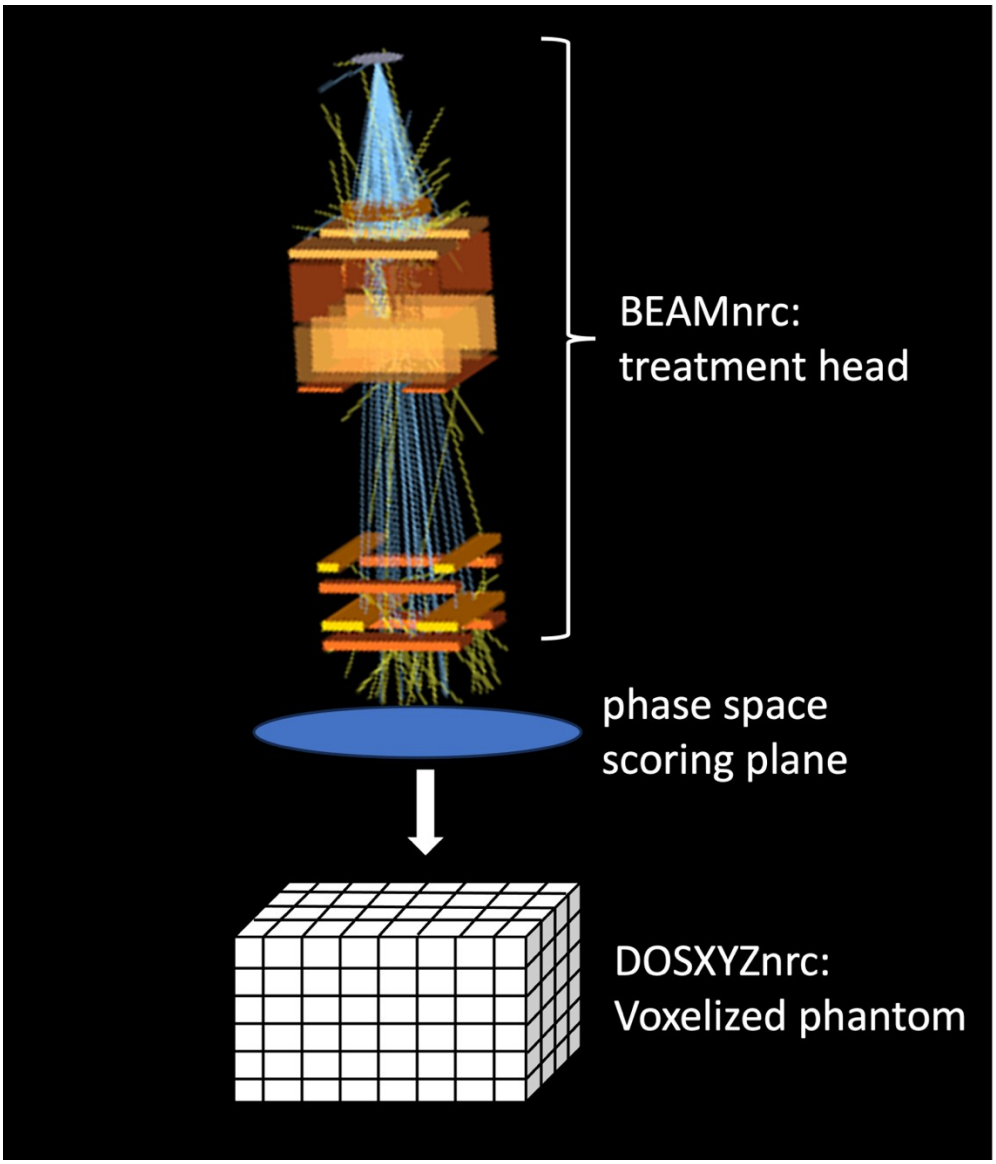

Figure 16. Diagram of EGSnrc Monte Carlo workflow illustrating the simulation of particle transport through the treatment head in BEAMnrc and subsequent dose calculation in a voxelized phantom in DOSXYZnrc (adapted from BEAMnrc manual[90]).

Chapter 3: Investigation of planar image quality for a novel 2.5 MV diamond target beam from a radiotherapy linear accelerator

3.1 Prologue

This manuscript describes the modification of a commercial 2.5 MV radiotherapy beamline to implement a novel sintered diamond target for improved image quality. Two beamlines were constructed including a preliminary external target setup following from previous work by Parsons et. al., and a clinically realistic setup with the target placed in the target arm. Image quality was assessed in comparison to the commercial 2.5 and 6 MV beams in terms of the spatial resolution and contrast-to-noise ratio. This work highlights the need for improved MV image guidance with respect to the auxiliary kV system, and presents a cost effective, simple solution.

This manuscript was published in the ESTRO highlights special issue of Physics and Imaging in Radiation Oncology:

Borsavage, J.M., Cherpak, A., Robar, J.L., Investigation of planar image quality for a novel 2.5 MV diamond target beam from a radiotherapy linear accelerator. *Physics and Imaging in Radiation Oncology*, vol. 16, pp. 103-108, 2020.

Minor additions were made to the methodology section of the approved version of this manuscript to provide more details regarding mode up and operation of the low-Z target, and to clarify the composition of materials used in CNR versus dose evaluation. Section 3.8 was added to the manuscript text to provide supplemental figures.

3.2 Abstract

Purpose: A commercial 2.5 MV beam has been clinically available for beam's-eye-view imaging in radiotherapy, offering improved contrast-to-noise ratio (CNR) compared to therapeutic beams, due to the softer spectrum. Previous research suggested that imaging performance could be improved using a low-Z diamond target to reduce the self-absorption of diagnostic energy photons. The aim of this study was to 1) investigate the feasibility of two 2.5 MV diamond target beamline configurations and 2) characterize the dosimetry and planar image quality of these novel low-Z beams.

Material and methods: The commercial 2.5 MV beam was modified by replacing the copper target with sintered diamond. Two beamlines were investigated: a carousel-mounted diamond target beamline and a 'conventional' beamline, with the diamond target in the target arm. Planar image quality was assessed in terms of spatial resolution and CNR.

Results: Due to image artifacts, image quality could not be assessed for the carousel-mounted low-Z target beam. The 'conventional' 2.5 MV low-Z beam quality was softer by 2.7% compared to the commercial imaging beam, resulting in improved CNR by factors of up to 1.3 and 1.7 in thin and thick phantoms, respectively. In regard to spatial resolution, the 'conventional' 2.5 MV low-Z beam slightly outperformed the commercial imaging beam.

Conclusion: With a simple modification to the 2.5 MV commercial beamline, we produced an improved energy spectrum for imaging. This 2.5 MV diamond target beam proved to be an advantageous alternative to the commercial target configuration, offering both superior resolution and CNR.

3.3 Introduction

High atomic number (Z) targets have proven unfavorable in megavoltage (MV) imaging beamlines due to self-absorption of diagnostic energy photons (i.e. in the range 25–150 keV)[17]. Consequently, MV imaging is associated with poor image contrast characteristics due to the Compton dominant interactions of photons in the MV spectrum. Image quality has been further compromised by the low efficiency of typical MV detectors, which is on the order of 1–2%[66]. Kilovoltage (kV) on-board imaging systems offer substantially better image quality than MV; however, these auxiliary systems introduce increased cost and maintenance, additional uncertainties[57], and prevent visualization of the treatment volume relative to the collimation of the beam during treatment[27].

While the kV system has provided superior image quality, the drawbacks of the system, as well as the potential for improved beam's-eye-view (BEV) image guidance, motivated the continued development of MV beams, such as the introduction of a commercial 2.5 MV FFF beam. With a lower nominal energy, this 2.5 MV beam contains a greater proportion of diagnostic energy photons compared to a 6 MV therapy beam, for example,

comprised 22% of photons in the diagnostic range[14] versus less than 1% for 6 MV[16]. This increased proportion of diagnostic energy photons resulted in increased contrast by factors of 2.5 to 3.6 times compared to 6 MV. Previous studies have suggested that this 2.5 MV low-X beam could be improved by replacing the current high-Z copper target with low-Z sintered diamond to further soften the spectrum[14,18]. The softer spectrum of the 2.5 MV low-Z beam should increase the absolute contrast between tissues and the achievable contrast-to-noise ratio (CNR), due to the $(h\nu)^{-3}$ dependence of the photoelectric mass attenuation coefficient[51]. Additionally, the CNR per unit dose should increase due to the increased detection quantum efficiency (DQE) of the diagnostic energy photons in the MV spectrum. Parsons *et al.* previously evaluated the commercial 2.5 MV low-X beam against a low-Z 2.35 MV carbon target beam using Monte Carlo simulations in VirtuaLinac[91] and EGSnrc[92]. Compared to the 2.5 MV low-X beam, this group observed an increase in the relative fraction of diagnostic energy photons by 10%, resulting in increased contrast by factors of 1.28 and 1.35 for thin and thick phantoms, respectively[14].

A variety of low-Z targets have been previously implemented on several treatment platforms[16,17,19,23,25], but this study marks the first installation on a modern linac. The aim of this study was twofold: 1) to investigate the feasibility of two 2.5 MV sintered diamond target beamline configurations; and 2) to characterize the dosimetric and image quality characteristics of the novel 2.5 MV low-Z target beams in comparison to the commercial 2.5 MV low-X beam. Due to the photoelectric absorption dependence on Z^3, we

hypothesized that replacing the 2.5 MV low-X copper target with low-Z sintered diamond would reduce the self-absorption of diagnostic energy photons, producing a softer beam with improved planar CNR.

3.4 Material and Methods

The low-Z target material used in this work was thermally stable polycrystalline (TSP) sintered diamond, a synthetic diamond selected for its low atomic number ($Z \approx 6$) and high melting point. Two low-Z target beamlines were investigated in this work, including: an external target setup with the diamond target mounted in the carousel of the linac, and a more 'conventional' beamline setup, with the diamond target machined into the target arm. Both targets were installed on a TrueBeam STx (Varian Medical Systems, Palo Alto, CA) C-arm linac.

3.4.1. Carousel-mounted target beamline

The preliminary beamline involved an external target mounted in the carousel of the linac, modeled after targets previously investigated on the Clinac platform[16,23,25]. The target assembly was manufactured to mimic the shape of a flattening filter, allowing for placement of the target as close to the exit window as possible. The cylindrical sintered diamond target was 3.1 mm thick (77% of the continuous slowing down approximation (CSDA) range of incident 2.5 MeV electrons) and 11 mm in diameter, which was maximized given the physical constraints of the beamline geometry. The design for the target assembly was determined by first optimizing the shape of a nylon mockup in an

empty port, ensuring adequate clearance during manual rotation of the carousel. Once machined, the target was installed and a procedure was established for operating the 2.5 MV beam with the target arm retracted and the carousel-mounted target in the beamline. Implementation of this beamline required manual mode up in service mode prior to operation of the custom beam, as outlined in the standard operating procedure outlined in Appendix B. To ensure the integrity of clinical beams following operation of the 2.5 MV carousel mounted target beam, necessary dosimetric and mechanical quality assurance was carried out before returning to clinical operation.

Unlike experiences with analogous beamlines on previous platforms, image quality could not be assessed for our low-Z carousel-mounted target beam due to the presence of a circular artifact in all images acquired with the MV detector (Fig. 4d). The source of the artifact was investigated by examining the integrity of the sintered diamond target, possible detector saturation, resultant dark current in the EPID from successive acquisition, and the incident electron beam spot size. The beam spot size was measured at various locations in the beamline including: the base of the carousel, the front face of the target, and at 75 cm SSD using sub-MU exposures on radiochromic film.

3.4.2 'Conventional' low-Z target beamline

3.4.2A Target arm machining and installation

The TrueBeam target arm was modified to replace the commercial copper target with a disk of TSP sintered diamond (13.44 mm in diameter, 5 mm thick). The thickness of the

diamond disk was selected to be 1.1 times the CSDA range[25] of 2.8 MeV electrons; optimized to account for uncertainties in the incident electron energy, eliminate transmission electrons and filter out photons with energy lower than 25 keV that would contribute increased dose to the patient[17]. Prior to machining, the distance between cooling lines in the arm (~ 1.7 cm) was measured based on an MV image of the target arm to ensure suitability of the target diameter. The copper target was milled out and the diamond disk secured in place by a lip on the underside of the target and using a mechanical press from the top face to ensure permanent installation (Figure 17). Prior to installation, the target arm was externally connected to the TrueBeam cooling system to confirm integrity of the cooling lines. All necessary quality assurance measures were carried out before and after installation to verify consistency of clinical beams. For safety reasons, the 2.5 MV beam was removed from clinical service and assigned solely for research.

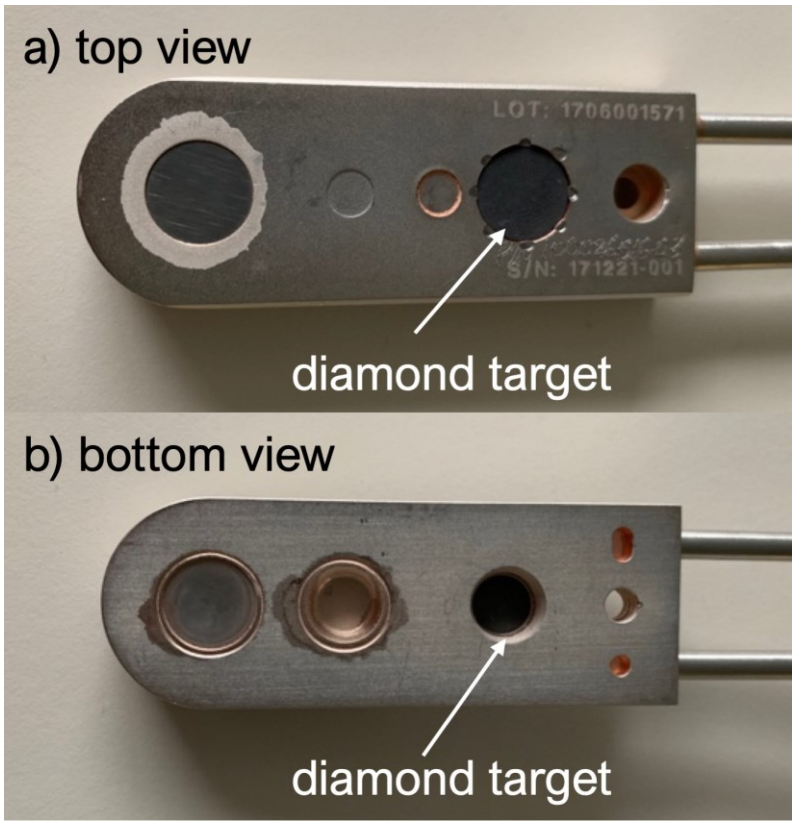

Figure 17. a) Top view and b) bottom view of experimental TrueBeam target arm showing the sintered diamond target secured into the fourth target position, replacing the low-X copper target.

3.4.2B Planar image quality characterization

Planar image quality was characterized in terms of spatial resolution and CNR. Spatial resolution was evaluated using the relative modulation transfer function (RMTF), following the methodology proposed by Rajapakshe *et al.*[93]. This method utilized the QC3 phantom (Figure 18a), which contains alternating pairs of high and low-density bars, forming line pair regions of the following spatial frequencies: 0.1, 0.2, 0.25, 0.4 and 0.75 line pairs per mm (lp/mm). For each input square wave frequency in the phantom, the calculated RMTF describes the degree of output signal modulation relative to the lowest spatial frequency. The QC3 phantom was setup to 99 cm SSD, held at a 45° with respect to the axial plane using an acrylic jig to avoid aliasing (Figure 18b). The phantom was

imaged at a gantry angle of 90° with a 14x14 cm^2 field using a SID of 150 cm. Multiple images were acquired for each beam to estimate uncertainty in RMTF calculations.

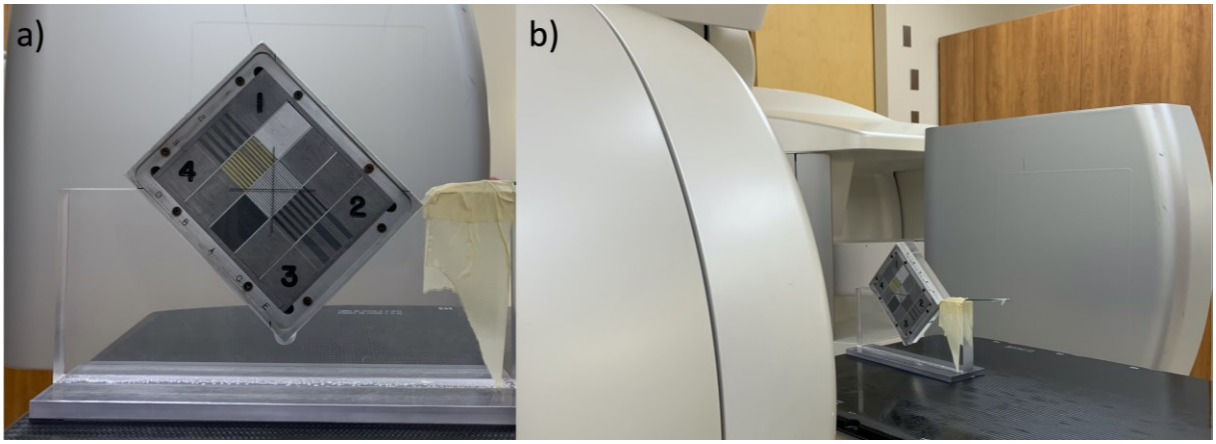

Figure 18. a) The QC3 phantom containing regions of various frequency bar patterns and b) the QC3 phantom setup at 99 cm SSD, at 45 with respect to the axial plane, for RMTF calculations

RMTF was calculated using Equation 10, where *M(f)* is the modulation of a given spatial frequency, *f*, and $M(f_1)$ is the modulation of the lowest spatial frequency (i.e. 0.1 lp/mm).

$$RMTF(f) = \frac{M(f)}{M(f_1)} \tag{10}$$

As suggested by Droege and Morin[94], signal modulation was calculated using Equation 11, where $\sigma_m^2(f)$ is the total variance in a given line pair region and $\sigma^2(f)$ is the variance due to random noise within the same region.

$$M^2(f) = \sigma_m^2(f) - \sigma^2(f) \tag{11}$$

The contributions due to random noise were removed from the signal modulation by subtracting sequential images. Since the variances of the two subtracted images are assumed equal, the variance due to random noise was calculated using Equation 12, as outlined by Rajapakshe *et al.*

$$\sigma^2(f) = \frac{\sigma^2_{sub}(f)}{2} \tag{12}$$

CNR was evaluated using an in-house phantom containing low- to high-contrast tissue equivalent inserts (Gammex, Middleton, WI), including brain, breast, CB2-30%, and cortical bone for thin (4 cm) and thick (20 cm) phantoms (Figure 19a)[23]. The CB2-30% material represents a formulation of CB2 resin mixed with 30% calcium carbonate by weight to replicate bone with a physical density of 1.33 g/cm^3 and electron density (relative to water) of 1.262 [95]. The inserts were arranged in a 14 cm-diameter circle centered on an inscribed crosshair on the top face of the solid water phantom (30x30x2 cm^3) for alignment with the beam's central axis. Two phantom thicknesses were constructed by wedging the contrast phantom between equivalent thicknesses of solid water to constitute the total phantom thickness (i.e. 4 and 20 cm). The phantoms were setup isocentrically and imaged at a gantry angle of 90^o to avoid contributions of couch scatter to acquired images (Figure 19b).

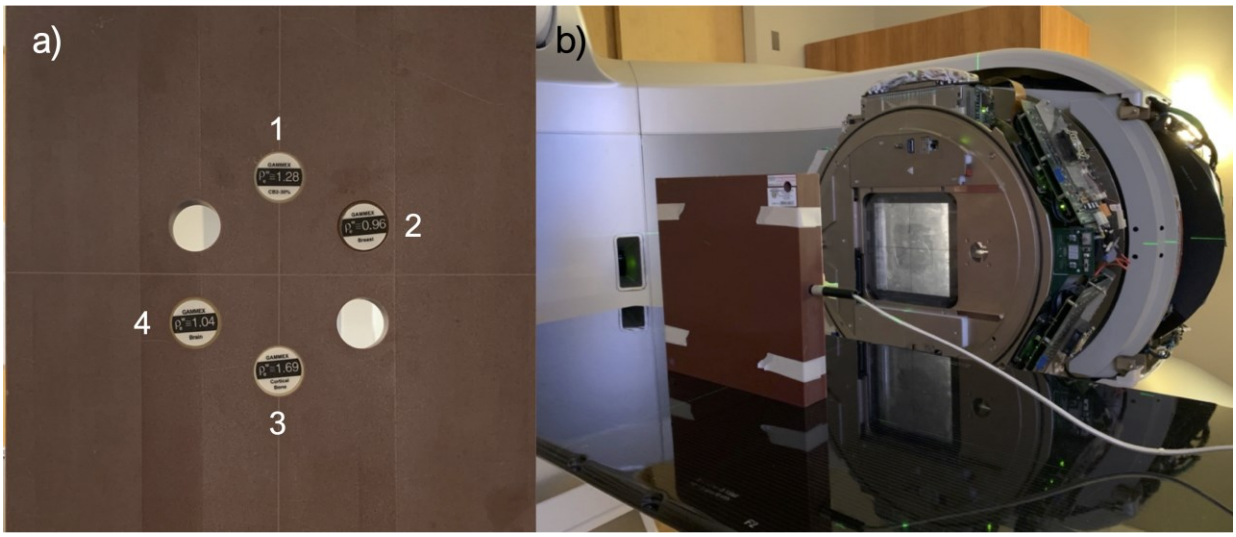

Figure 19. a) In-house contrast phantom containing 1) CB2-30% 2) breast 3) cortical bone 4) brain tissue equivalent inserts and two voids for additional materials and b) thin contrast phantom imaging setup at 98 cm SSD.

3.4.2C Imaging dose calculation

The 2.5 MV low-Z and 2.5 MV low-X beams were calibrated using the American Association of Physicists in Medicine's Task Group 51 formalism[96]. PDD curves were acquired for 10x10 cm^2 fields at 100 cm SSD to determine beam quality. In a previous study investigating 2.5 MV low-X imaging dose, Ding and Munro[56] calibrated the 2.5 MV low-X output using k_Q = 1.00. Assuming negligible differences between the chamber perturbation factors of the 2.5 MV beam and Co-60, they calculated k_Q as the ratio of Spencer-Attix water-to-air stopping-power ratios (SPR) for the two beam energies. The study reported less than 0.1% difference between the SPR of the 2.5 MV low-X beam and Co-60 at the recommended calibration depth of 10 cm[56], thus concluding k_Q = 1.00. Based on Ding and Munro's study[56], and the fact that our measurements found similar beam qualities for the 2.5 MV low-X and 2.5 MV low-Z beams (i.e. 52.85% and 50.15%, respectively), k_Q = 1.00 was assumed for both beams.

Dose per MU was calculated for the 2.5 MV low-X and 2.5 MV low-Z beams under reference conditions using an isocentric setup (i.e. 10x10 cm^2 field, 90 cm SSD, 10 cm depth). Point dose measurements were performed in water using a calibrated Exradin A12 (Standard Imaging, Middleton WI) ion chamber. Output factors and corresponding TPR measurements were made for a 20x20 cm^2 field for both 2.5 MV low-X and 2.5 MV low-Z beams to calculate imaging dose for thin and thick phantom setups. Imaging doses for the 6 MV beam were calculated by modeling the thin and thick solid water phantoms in the treatment planning system (Eclipse version 13.6, Varian, Palo Alto, CA).

3.5 Results

3.5.1 Carousel-mounted target beamline

Removal of the carousel-mounted target confirmed that the target was intact (Figure 20a). Film irradiated at 75 cm SSD verified that the circular artifact was due to the incident electron beam and unrelated to the EPID (Figure 20c). The film irradiated at the base of the carousel revealed that the full-width-half-maximum (FWHM) of the spot size was 23.5 mm; more than twice the diameter of the diamond target (Figure 20b). The dose on the periphery of the film irradiated at the level of the target was 58% of that on the central axis; confirming that the electron beam spot size was larger than the target. This was deemed an insurmountable limitation of this approach to introducing a diamond target, given that the physical constraints of the installation limit further increase of the target diameter. Furthermore, it would be physically impossible to move the target closer to

the exit of the electron beam from the vacuum, where the electron beam might be sufficiently narrow to create a useful focal spot for imaging.

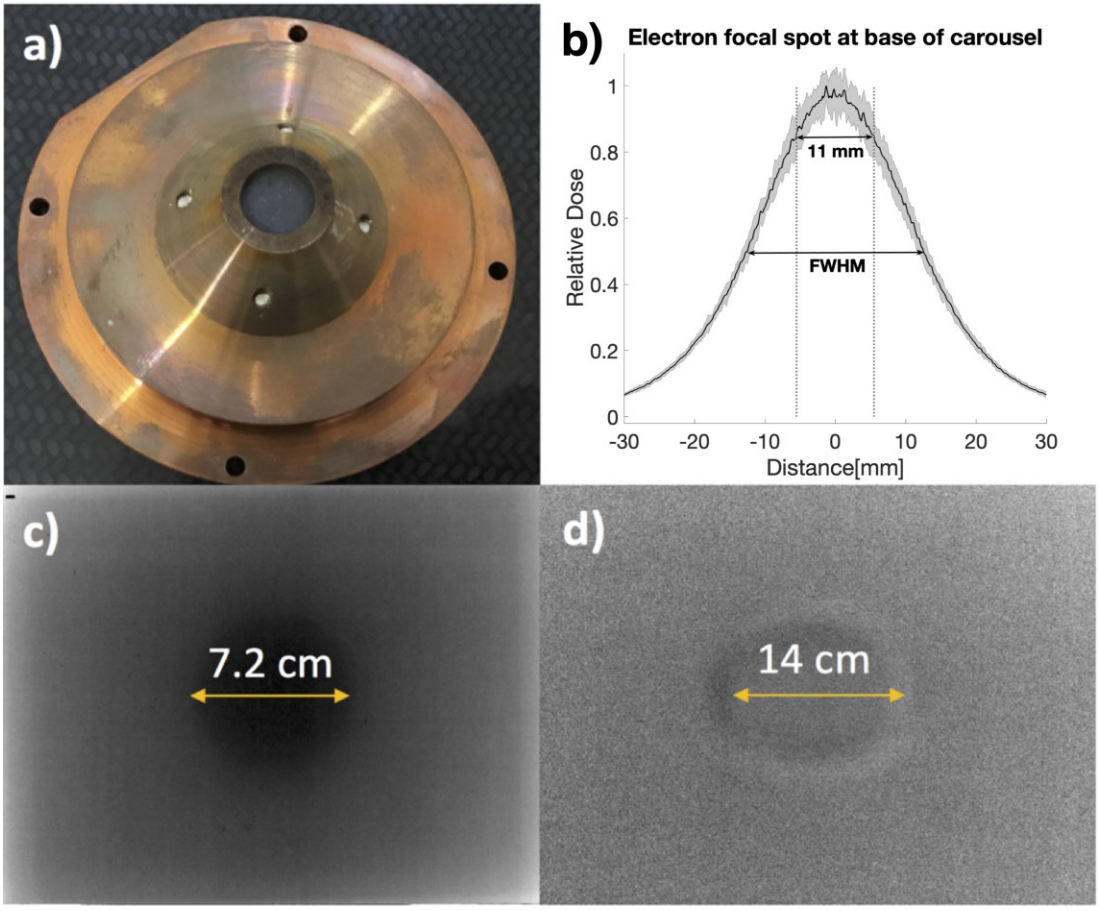

Figure 20. Pictorial representation of circular artifact investigation a) Intact carousel mounted target assembly b) Electron focal spot measured with radiochromic film below the target plane showing the diameter of the exposed sintered diamond target (11 mm) and the corresponding FWHM c) Radiochromic film image acquired with 2.5 MV diamond target beam at 75 cm SSD d) EPID acquired test image with 2.5 MV diamond target beam at 150 cm SID.

3.5.2 'Conventional' low-Z target beamline

3.5.2A Planar image quality characterization

The calculated RMTF, derived from images of the QC3 phantom, shows that our experimental 2.5 MV low-Z beam outperforms the commercial 2.5 MV low-X and 6 MV beams in terms of spatial resolution (see Figure 21). We observed increases in F_{50}, the frequency at which the RMTF decreases to 50%, by 22.7% and 12.5% for the 2.5 MV low-

Z and 2.5 MV low-X beams, compared to 6 MV. This translated to an increase of approximately 0.5 lp/mm, and 1 lp/mm for the 2.5 MV low-Z beam compared to the 2.5 MV low-X and 6 MV beams, respectively. The improved spatial resolution was likely due to reduced extra-focal radiation resulting from the absence of a flattening filter in the 2.5 MV beamlines.

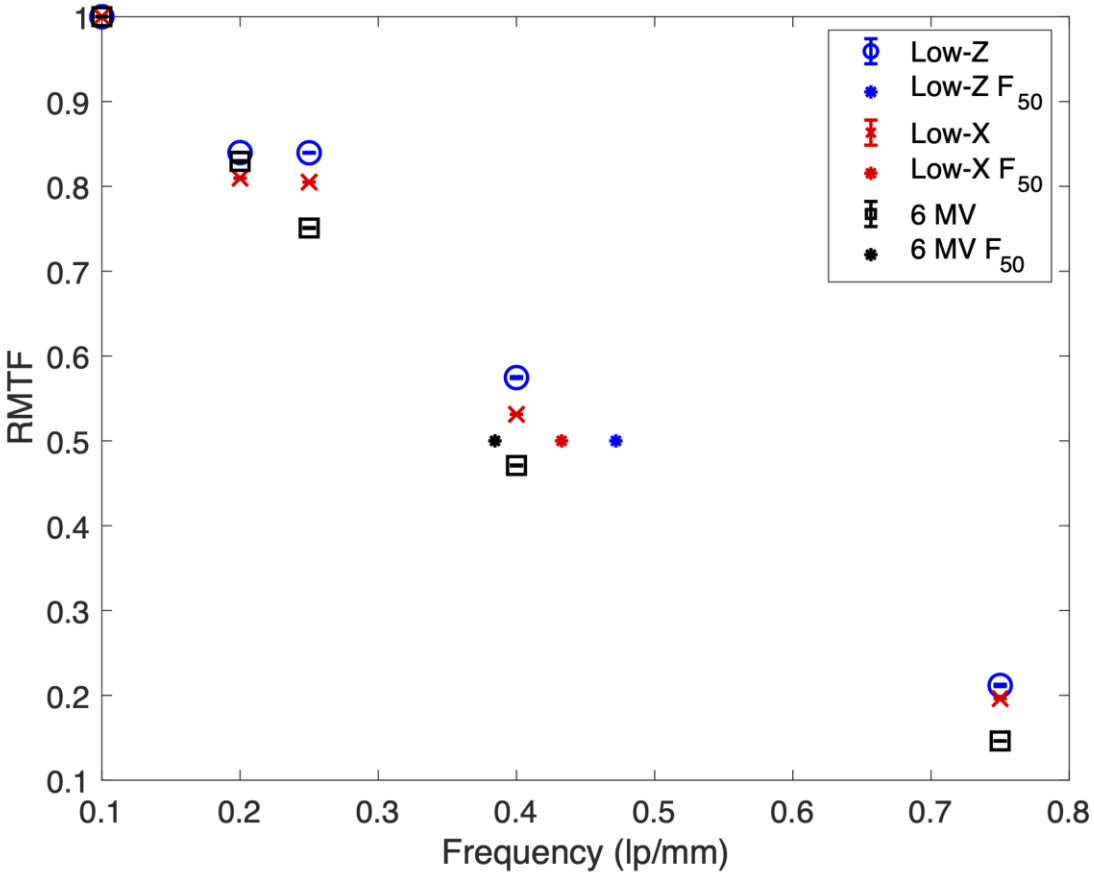

Figure 21. Relative modulation transfer function of 2.5 MV low-Z, 2.5 MV low-X and 6 MV beams

The CNR versus dose results presented in Figure 22 demonstrate a clear advantage for the 2.5 MV low-Z beam at imaging doses above 1 mGy in the thin phantom and above 3 mGy in the thick phantom, compared to the 2.5 MV low-X beam. At doses above 3 mGy,

the CNR of each material in the thick phantom was greater for the low-Z beam than the low-X beam, by factors of 1.4-1.7 for breast, and 1.1-1.3 for cortical bone. The same trend was observed for materials in the thin phantom above 1 mGy, excluding cortical bone. Increases in CNR were observed in breast and CB2-30% in the thin phantom by factors of 1.2-1.3 and 1.2-1.4, respectively. Unlike the other materials in the thin phantom, the difference in the CNR of cortical bone between the low-Z and low-X beams is negligible across all doses. At doses less than 1 mGy, the difference in CNR between images acquired with low-Z and low-X beams were negligible for breast and cortical bone in the thick phantom.

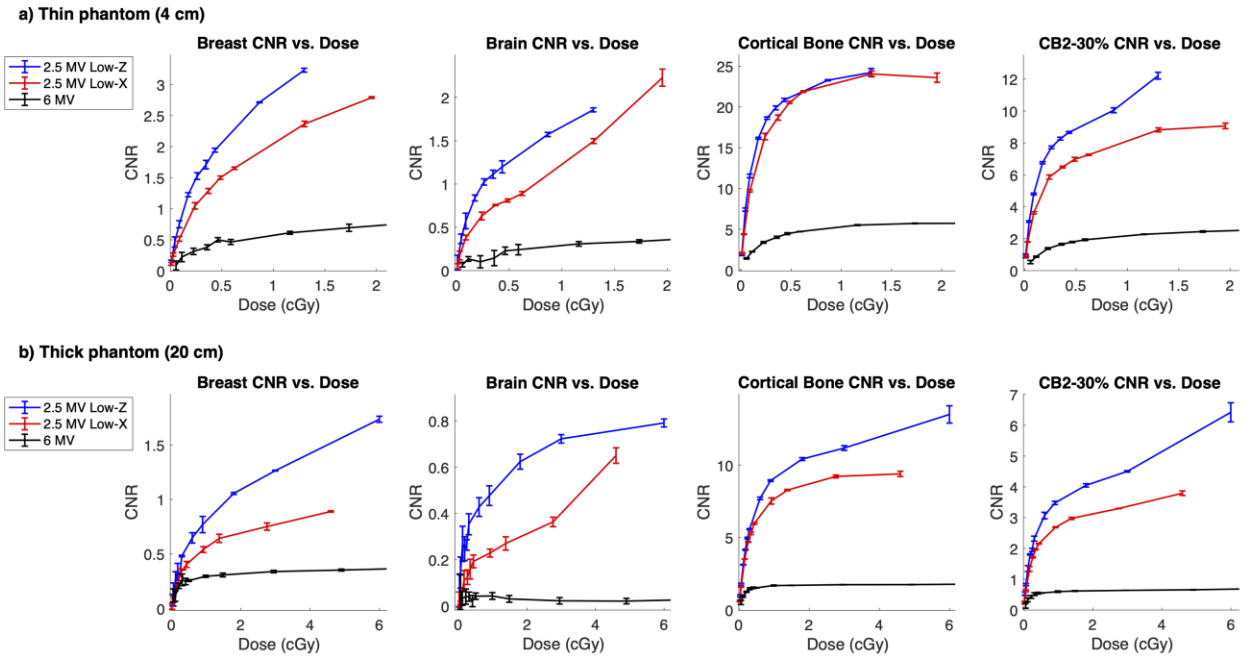

Figure 22. CNR versus dose for breast, brain, cortical bone, and CB2-30% tissue equivalent inserts in a) thin (4 cm) and b) thick (20 cm) phantoms

3.6 Discussion

This work marks the first implementation of a low-Z diamond target beam for 2.5 MV imaging on a modern linac platform. In our investigation, we implemented two beamline geometries including (i) a carousel-mounted target design, and (ii) a 'conventional' setup with the target in the target arm.

Based on our thorough investigation of the carousel-mounted target beamline, we have concluded that the large electron spot size impinges on the copper housing of the target assembly, causing a non-uniform photon fluence below and the appearance of a circular artifact in images acquired by either film or the EPID. This is caused by the geometry of the carousel relative to the exit window, such that the electron scatter in air produces a large focal spot incident on the upstream surface of the target. While the carousel-mounted target design has been used successfully on a previous platform[16,23,25], the redesign of the beamline in the current platform precludes this carousel-mounted target design.

On the other hand, a viable approach is installation of a diamond target in the target arm (our 'conventional' setup), and for this configuration we have evaluated planar image quality compared to the commercial 2.5 MV low-X beam. As hypothesized, replacing the high-Z copper target with low-Z sintered diamond in the 2.5 MV beamline produced a softer beam, as demonstrated by the 2.7% reduction in PDD(10 cm) for the 2.5 MV low-Z beam compared to 2.5 MV low-X. We found similar beam quality to the 2.35 MV carbon

target beam modelled by Parsons *et al.*, although our 2.5 MV low-Z PDD(10 cm) was greater by 1.6%. This is likely due to the small difference in nominal energy as well as the presence of high-Z sintering materials in our target. Compared to the commercial 2.5 MV low-X beam, the softer low-Z spectrum resulted in improved CNR by factors of up to 1.7, at clinically relevant MV imaging doses. This permits either improved CNR for the same dose, or conversely, decreased imaging dose for the same CNR. We observed advantages of the low-Z beam over the commercial 2.5 MV low-X beam for both thin and thick phantoms, except for cortical bone in the thin phantom and in cases where CNR itself is very low (< 1) for all beams, i.e., where the objects were essentially indistinguishable from background.

While this study has focused solely on planar imaging with the low-Z beam, in concept the same beam could be used for cone-beam CT acquisition, and even volume-of-interest CBCT using the MLC for collimation according to the relevant anatomy for the given image guidance task[97]. Although kV imaging provides superior image quality to MV per unit imaging dose, image guidance from the BEV is valuable in the delivery of precision radiation therapy. With a simple modification to the 2.5 MV low-X beamline, we produced a softer energy spectrum for imaging, which improves BEV imaging with better spatial resolution and CNR. We anticipate that additional modifications to the low-Z beamline could further improve the CNR versus dose characteristics of 2.5 MV BEV imaging. One such alteration, to be examined in forthcoming work, is the removal of the 0.81 mm brass cover-plate from the carousel of the 'conventional' 2.5 MV low-Z target beamline, to

further reduce the self-absorption of diagnostic energy photons within the treatment head. Another feasible approach involves modifying the EPID to increase the DQE, such as the integration of a thick CsI flat-panel detector[98].

This study concludes our initial characterization of this novel 2.5 MV diamond target beam for BEV imaging. We demonstrated the ease of installation of a low-Z sintered diamond target beam on a modern linac, and the consequent improvements in CNR as a function of dose compared to the current low-X mode. We suggest sintered diamond as a favorable alternative to the current copper target in the 2.5 MV low-X beamline.

3.7 Additional Material

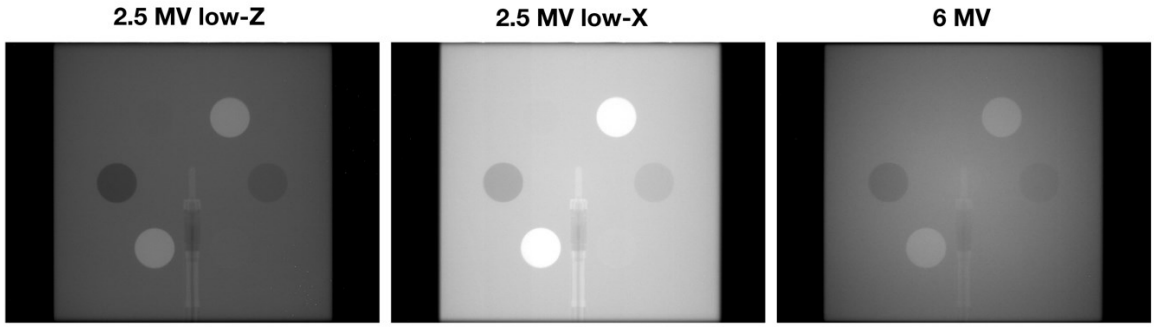

Figure 23. Qualitative demonstration of planar CNR phantom images acquired with 2.5 MV low-Z, 2.5 MV low-X and 6 MV beams using 1 cGy imaging dose. Digital contrast settings (i.e. window width and window level) maintained between images acquired with each beam for meaningful comparison.

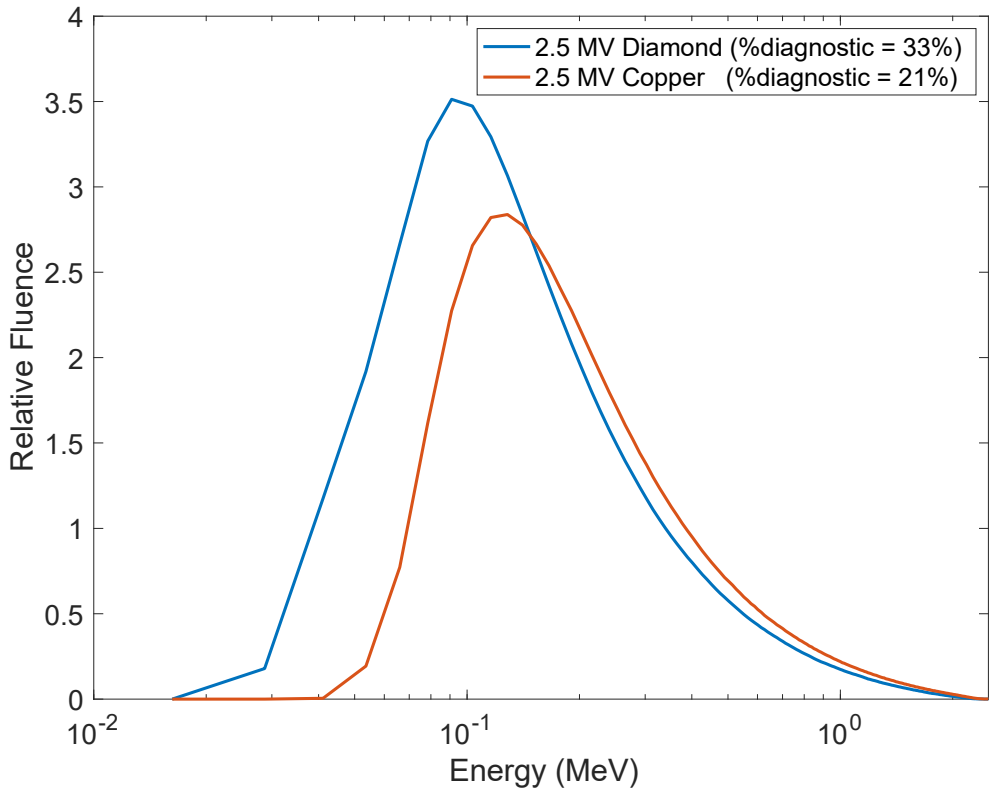

Figure 24 Representative Monte Carlo derived spectra for 2.5 MV diamond and copper target beams demonstrating increased yield of low-energy photons recovered by diamond target beam compared to copper target beam.

Chapter 4: Improving image quality and reducing dose with 2.5 MV diamond target volume-of-interest cone beam CT

4.1 Prologue

Expanding on the work detailed in Chapter 3, this manuscript examines the image quality in volumetric image acquisitions for the 2.5 MV sintered diamond target beam compared to the commercial 2.5 MV beam. In addition to full field of view CBCT, this work investigates the use of volume-of-interest CBCT for potential dose sparing and improved image quality. This manuscript highlights the process of VOI CBCT acquisition and image processing, as well as the improved image quality of the novel 2.5 MV in both full field and VOI volumetric imaging.

This manuscript was published in Medical Physics:

Borsavage, J.M., Cherpak, A. J., Robar, J. L., Improving image quality and reducing dose with 2.5 MV diamond target volume-of-interest cone beam CT imaging. *Medical Physics*, vol 49., no. 12, pp. 7661-7671. 2022.

Minor additions were made to the approved version of this manuscript to reference Figure 31 in the text. The tabulated values in Table 4 were updated for significant digits.

4.2 Abstract

Purpose: Over the past decades, continuous efforts have been made to improve megavoltage (MV) image quality versus dose characteristics, including the implementation of low atomic number (*Z*) targets in MV beamlines and the development of more efficient detectors. Recently, a diamond target beam within a commercial radiotherapy treatment platform demonstrated improved planar contrast-to-noise-ratio (CNR) per unit dose using a novel 2.5 MV sintered diamond target beam, which enabled image acquisition on the order of mGy. The present work assesses cone beam CT (CBCT) image quality characteristics for the novel 2.5 MV diamond target beam and the effects of volume-of-interest (VOI) collimation on the image quality and imaging dose distribution.

Methods: A sintered diamond target was incorporated into the target arm of the linear accelerator, replacing the 2.5 MV commercial copper imaging target. CBCT image quality was evaluated against the commercial imaging beam with regard to spatial resolution and CNR versus dose. In addition to full-field acquisitions, we investigated VOI techniques that collimate the imaging beam to preselected anatomy, to determine potential image quality improvements and dose sparing capacity. Using an anthropomorphic phantom, VOI regions were defined to encompass the maxillary and ethmoid sinuses and ranged in dimension from 3 cm to 4.85 cm equivalent radius. The MLC was fit to each VOI structure throughout a full CBCT arc and the corresponding MLC sequences were produced as XML

scripts for acquisition. Calibrated radiochromic film was used in phantom to measure cumulative axial dose distributions during each CBCT acquisition.

Results: In full-field CBCT, the 2.5 MV diamond target beam demonstrated improved CNR versus dose compared to the commercial imaging beam, by factors of up to 1.7. The calculated modulation transfer function (MTF) displayed an increase of nearly 30% in f_{50} for the 2.5 MV diamond target beam compared to the commercial beam. Using VOI techniques, CNR increased monotonically as a function of equivalent radius at the bone–tissue interface. At the bone–sinus interface, the CNR for the full-field case was slightly decreased compared to the largest VOI case. Imaging dose in the anteroposterior direction increased with increasing VOI equivalent radius.

Conclusion: The novel 2.5 MV sintered diamond target beam presents a simple modification to the commercial imaging beam which provides improved image quality in full-field CBCT and the potential for simultaneous dose sparing and CNR improvement at high-contrast interfaces using VOI acquisition techniques.

4.3 Introduction

Although megavoltage (MV) imaging was widely available well before the integration of kilovoltage (kV) systems to allow image guidance on modern linear accelerators, the use of MV image guidance is limited due to inferior image quality and higher imaging doses. Kilovoltage x-ray image guidance offers favorable image quality and dose characteristics,

but kV onboard imaging incurs increased cost, maintenance, and introduces its own uncertainties[57]; while for planar imaging, lacks the advantageous perspective of the treatment beams-eye-view[27]. Numerous efforts have focused on improvement of MV imaging systems with regard to both detectors and beam production, including the ongoing development of efficient multilayer detectors[99,100] and the recent installation of the 2.5 MV imaging beam on the modern TrueBeam (Varian Medical Systems, Palo Alto, CA) treatment unit.

Recently, and for the TrueBeam platform, it has been demonstrated that the 2.5 MV imaging beam could be improved significantly by implementing a low-*Z* target for photon production, specifically one made of sintered diamond.[101] Since sintered diamond has a lower atomic number than the commercial copper target (i.e., $z \approx 6$ versus $z = 29$), a 2.5 MV diamond target beam contains a higher percentage of diagnostic energy photons (i.e., 25–150 keV)[17] than the commercial beam, arising from a decreased photoelectric self-absorption of low energy photons within the target. Consequently, this 2.5 MV diamond target beam demonstrates improved contrast-to-noise ratio (CNR) versus dose characteristics compared to the commercial 2.5 MV copper target beam, by factors of up to 1.7 times in planar imaging[101].

This study examines the feasibility of MV cone-beam CT (CBCT) with this novel 2.5 MV diamond target beam. Although low-dose MV CBCT with standard MV therapy beams has been explored in experimental benchtop settings[98,100,102,103] the 1%–2% detective

quantum efficiency[66] of commercial detectors in combination with these beams has limited translation to the clinic. Due to its unique energy spectrum, the sintered diamond target beam permits 2.5 MV image acquisition with doses on the order of mGy per frame[101] and therefore may be comparatively advantageous for CBCT acquisition. In addition, MV imaging allows one to leverage the presence of the multileaf collimator (MLC) in the beamline through volume-of-interest (VOI) CBCT[97] acquisition. A VOI approach localizes the imaging dose on anatomy relevant for image guidance. Relative to full-field imaging, we expect the VOI technique to lower the imaging dose both within (due to scatter reduction) and outside of the imaging volume (due to shielding). In addition, we hypothesize that reducing VOI dimension may improve image quality per unit dose due to improving the primary-to-scatter characteristics of the beam[104].

This work demonstrates the use of low-*Z* target MV CBCT on a modern TrueBeam platform with realistic CBCT acquisition enabled by Developer mode, that is, not using an experimental benchtop rotational stage. Compared to previous studies on the Clinac platform[97,105] our methodology is more realistic in two respects. First, the sintered diamond target is located in the standard location within target arm of the linac, instead of being installed in the flattening filter carousel as in previous studies[97,105–107]. Second, the TrueBeam unit is equipped with Developer mode, a dedicated research platform which enables MV CBCT acquisition throughout a defined gantry arc, thus allowing realistic acquisition, rather than employing previous methods using a rotational stage to simulate gantry motion. This work presents the low-dose MV CBCT acquisition

methodologies and VOI techniques, characterizes 2.5 MV diamond CBCT image quality for full-field and VOI acquired datasets, and reports on the dose sparing potential of VOI CBCT techniques for this novel beam.

4.4 Material and Methods

4.4.1 Diamond target beam production

The sintered diamond target used in this study was composed of 99% diamond and 1% cobalt. The target, shown in Figure 25, was machined into the target arm replacing the copper target for the commercial 2.5 MV imaging beam. The modified arm was installed on a TrueBeam STx unit as described previously[101]. This simple hardware modification enabled the operation of the 2.5 MV diamond target beam, without the need for tuning a customized beam as was done for the 4.2 MV low-*Z* imaging beam on Siemens linacs[19]. The diamond target is 5 mm thick, corresponding to 1.2 times the CSDA range of 2.5 MeV electrons; a conservative choice to eliminate transmission electrons and filter out any undesirably low-energy photons (i.e., less than 10 keV). With an increased population of low-energy photons, the resultant beam, herein referred to as 2.5 MV diamond, is lower in quality with a depth of maximum dose of 4.8 mm compared to 5.8 mm for the commercial 2.5 MV beam, and percent depth dose at depth 10 cm of 50.15%, compared to 52.85%[101].

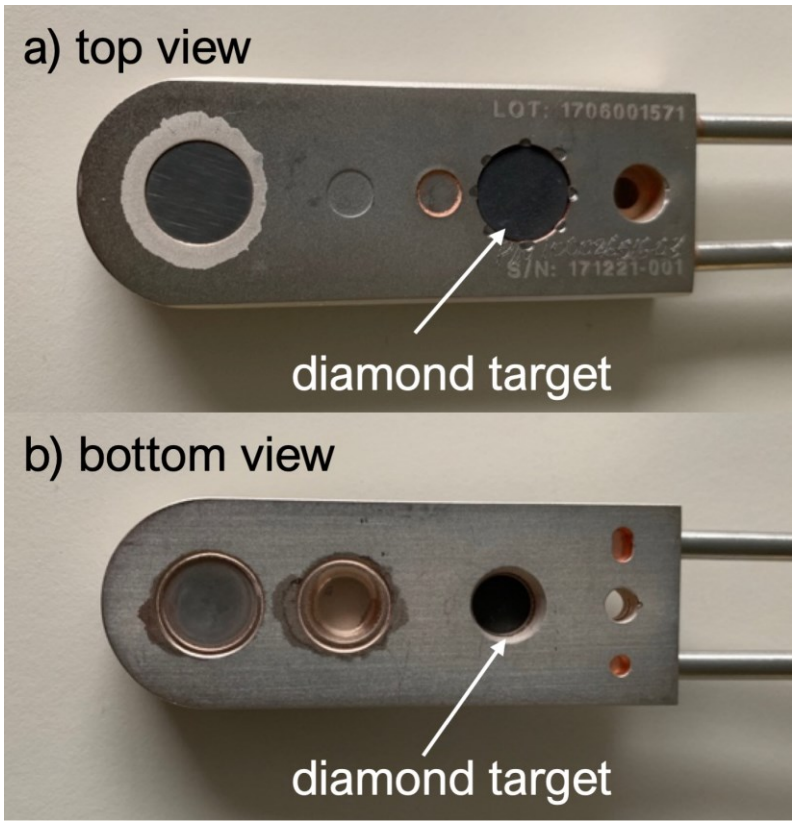

Figure 25. a) Top view and b) bottom view of experimental TrueBeam target arm showing the sintered diamond target secured into the fourth target position, replacing the commercial copper target.

4.4.2 Diamond target cone beam CT acquisition and reconstruction

All MV CBCTs in this study were acquired on a TrueBeam STx unit using Developer mode. Developer mode is a research platform available for the TrueBeam, which enables user-defined control of machine axes, imaging and beam parameters using XML scripting. Each CBCT was acquired using the high-quality MV imaging mode with continuous acquisition modified to acquire images at 6 frames/s. Since these customized settings differed from the calibrated high-quality mode defined on the machine, automatic corrections were not available. Instead, dark and flood calibration fields were acquired for each imaging session at a static gantry angle of 0°, using an acquisition rate of 6 frames/s, averaged over 100

frames. Each CBCT projection was post-processed in Matlab (Mathworks, Natick, MA) to apply offset, uniformity, and gain corrections using the averaged flood and dark field images. VOI projections were additionally processed to mitigate truncation artifacts using an extrapolation filling technique as described in section 4.4.4. All projections, both full field of view (FOV) and extrapolated VOI, were reconstructed with 2 mm slice thickness in iTools 2.0 (Varian Medical Systems, Palo Alto, CA) using Feldkamp–Davis–Kress (FDK) filtered backprojection. Reconstructed images were further processed in iTools to apply ring artifact suppression and to map pixel values to Hounsfield units (HU). To provide relevant clinical comparisons, additional kV CBCTs were acquired using predefined CBCT protocols on the TrueBeam (i.e., head, thorax, and pelvis large) as defined in the machine settings (see Table 2). All kV CBCTS were acquired in the treatment mode on the TrueBeam using default acquisition and reconstruction parameters.

Table 2 Kilovoltage (kV) cone beam CT (CBCT) acquisition settings

CBCT protocol	Beam energy	mAs	Trajectory	Fan type
Head	100	150	Half (200)	Full
Thorax	125	270	Full (360)	Half
Pelvis large	140	1687.50	Full (360)	Half

4.4.3 Cone beam image quality

The 2.5 MV diamond CBCT image quality was characterized in terms of CNR and spatial resolution compared to the 2.5 MV commercial imaging beam and kV CBCT protocols set on the TrueBeam (i.e., head, thorax, pelvis large). CNR was evaluated using the CIRS 062M electron density phantom (CIRS Inc., Norfolk, VA) which consists of two concentric solid water volumes, with cylindrical inner dimensions of 18 cm × 5 cm (diameter × height) and outer elliptic cylindrical dimensions of 33 cm × 27 cm × 5 cm (major diameter × minor diameter × height). Each cylindrical volume contains eight different tissue equivalent materials allowing imaging of thin and thick phantoms, for example, the inner cylinder or the ensemble, respectively. The phantom was imaged with both thin and thick configurations across a wide range of doses (e.g., 0.75–38 cGy) to determine CNR versus dose for each 2.5 MV beam. For realistic kV comparisons, the thin phantom was imaged with the kV 'head' protocol, and the thick phantom was imaged with additional 'thorax' and 'pelvis large' protocols. Imaging dose was measured at the center of the phantom using an Exradin A12 chamber for all MV and kV acquisitions. Imaging dose was calculated using previously established calibrations for 2.5 MV acquisitions, while kV imaging dose was determined using an interpolated chamber correction factor from a previous calibration report in the TG-61 formalism. CNR was calculated for the various tissue equivalent inserts, including lung (inhale), lung (exhale), liver, bone (800 mg/cm^3), and bone (200 mg/cm^3), using Equation 13, where P and σ are the average and standard deviation of pixel intensity in the region of interest (ROI) and background (bg). The

radiological properties of each insert are provided in Table 3. CNR was calculated and averaged for each insert in the central seven slices of the reconstructed volumes.

$$CNR = \frac{|\bar{P}_{ROI} - \bar{P}_{bg}|}{\sqrt{\sigma_{ROI}^2 + \sigma_{bg}^2}} \quad (13)$$

Table 3 Radiological properties of CIRS 062M tissue equivalent material inserts

Tissue equivalent material	Physical density (g/cm^3)	Electron density (×10^{23} electrons/cm^3)	RED (relative to H_2O)
Lung (inhale)	0.205	0.668	0.200
Lung (exhale)	0.507	1.658	0.496
Liver	1.07	3.516	1.052
Bone (800 mg/cm^3)	1.53	4.862	1.456
Bone (200 mg/cm^3)	1.16	3.730	1.117

*Values obtained from CIRS 062M manual.

Spatial resolution was characterized in terms of the modulation transfer function (MTF), derived from reconstructed images of the CTP528 line pair module of the Catphan 504 phantom. This module contains line pair regions with spatial frequencies ranging from 1 to 21 line pairs (lp)/cm. Using the central slice of the reconstructed volume, profiles were captured through each line pair region to quantify the variation of signal modulation as a function of spatial frequency[59]. Modulation was calculated for each profile as the ratio of

the difference between the maximum and minimum pixel intensity to the sum of the two values, as described by Equation 14, where I_{max} and I_{min} are the maximum and minimum pixel intensities through a line profile for a given frequency, f. MTF was calculated for each spatial frequency using Equation 15, where f_0 is the lowest frequency line pair region (i.e., 1 lp/cm).

$$Modulation\ (f) = \frac{I_{max} - I_{min}}{I_{max} + I_{min}} \tag{14}$$

$$MTF(f) = \frac{modulation(f)}{modulation(f_0)} \tag{15}$$

4.4.4 Volume-of-interest definition and acquisition

The anthropomorphic ATOM phantom (CIRS Inc., Norfolk, VA) was imaged to investigate the effects of VOI imaging parameters on CNR versus dose. The VOI for this case was defined as the region containing the maxillary and ethmoid sinuses. The process of defining the VOI regions and subsequently acquiring VOI images was analogous to the treatment planning and delivery workflow. It began with acquiring a CT scan of ATOM's head and neck which was used to delineate VOIs in the treatment planning system (TPS). We defined four VOIs encompassing the sinuses, of which the smallest conformed tightly to the sinus cavity and the additional volumes were defined by adding margins of 0.5, 1, and 1.5 cm, referred to herein as $VOI_{3\ cm}$, $VOI_{3.65cm}$, $VOI_{4.3\ cm}$, and $VOI_{4.85\ cm}$. The subscripts correspond to the equivalent sphere radius of each VOI, as calculated by the TPS. MLC sequences were determined by fitting the leaves to the beams-eye-view of each VOI

throughout a full 360° gantry rotation (see Figure 26). The DICOM plan files, containing the leaf positions at each control point for the four plans, were then used to construct XML scripts to drive image acquisition on the treatment unit. For each VOI, two image sets were acquired using a high- and a low-dose per frame setting of 1 and 0.1 MU, respectively. During the high-dose acquisitions, a sheet of calibrated radiochromic EBT3 film (Ashland Advanced Materials, Bridgewater, NJ) was placed between slices of the phantom to enable measurement of axial dose distributions throughout the VOIs and the peripheral anatomy. The high-dose per frame setting was selected to ensure the composite dose was within the dynamic range of the film. Full FOV image sets of the phantom's head were also acquired for both high- and low-dose settings, for our evaluation of image quality and dose sparing with the VOI technique. An additional kV CBCT was acquired using the TrueBeam 'head' protocol to provide a comparison to realistic clinically acquired images.

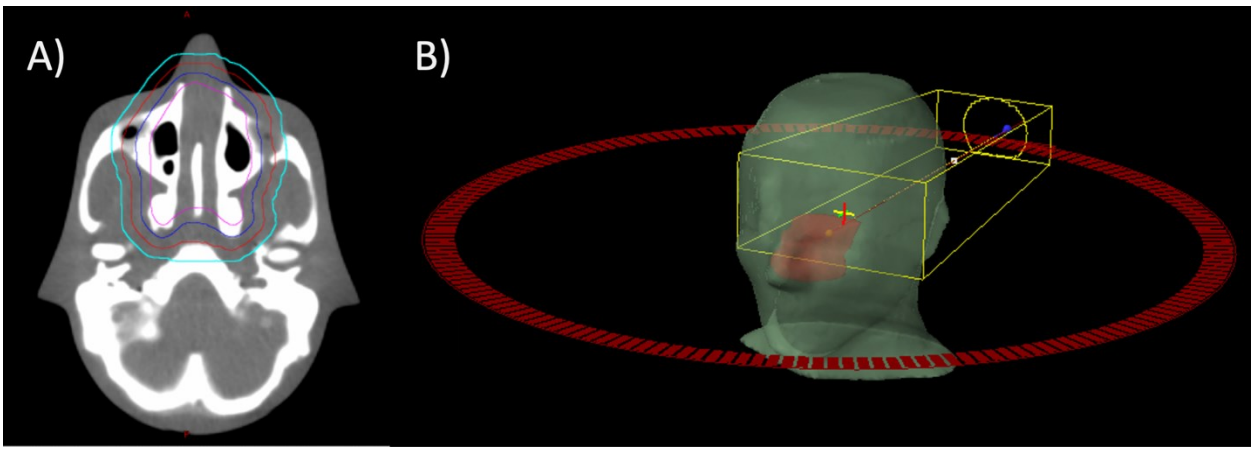

Figure 26 a) VOI contours in axial plane and b) beams-eye-view VOI aperture defined by MLC at start of 360 degree arc acquisition.

4.4.5 Volume-of-interest extrapolation filling

The purpose of the VOI acquisition was to selectively image a volume of the head as defined by the set of MLC apertures, however a known consequence of this technique is the occurrence of truncation artifacts which appear in the reconstructed volume as a dark ring around the truncated anatomy[108]. To reduce the presence of these artifacts, truncated projections were processed prior to reconstruction using an extrapolation filling technique. Using the methodology described by *Robar et. al.*[105], image data were extrapolated from the left and right boundaries of each truncated projection out to the edges of the image in a row-wise manner.

4.4.6 Diamond target beam VOI image analysis

Extrapolated VOI projections were reconstructed as described in section 2.2. CNR was calculated for user-defined regions of interest at bone-tissue and bone-sinus interfaces. ROIs were sampled from the central three slices of the reconstructed volume and CNR was calculated using Equation 13. CNR values were averaged across the three slices and reported as a function of the equivalent sphere radius of the VOI imaging field, as calculated from the TPS.

For 2.5 MV dose measurements, EBT3 films were digitized using an Epson 1000XL scanner at 72 dpi resolution after the recommended 24 hours post-exposure. The digitized films were analyzed in FilmQAPro software (Ashland Advanced Materials, Bridgewater, NJ) to convert optical densities to absorbed dose using triple-channel dosimetry[109]. Dose

profiles were captured along the anteroposterior (AP) direction of the head phantom along the center of each film image. To demonstrate the dose sparing abilities of the VOI technique, each MV VOI dose profile was normalized to the maximum dose for the full FOV image volume. Imaging dose for kV acquisitions was measured using optically stimulated luminescence detectors (OSLD) nanoDots to capture the same profile along the AP direction. To eliminate air gaps between adjacent phantom slices, small slits were machined in the phantom for insertion of the nanoDots, as demonstrated in Figure 27. The measured dose was read out using a microSTAR (Landauer Inc. Glendwood, IL) reader and dose was calculated using a previously established calibration[110] corresponding to a 100 kV beam on a Somatom Definition AS+ CT scanner (Siemens Healthcare, Erlangen, Germany). While this estimation may introduce error in dose calculations due to the difference in beam qualities (i.e. HVL of 7.6 mm versus 4.08 mm for the 100 kV CT and 100 kV CBCT beams, respectively), this error has been minimized by normalization; whereby the effects of the multiplicative energy-dependent correction factor calculated by Al-Senan and Hatab[111] are eliminated.

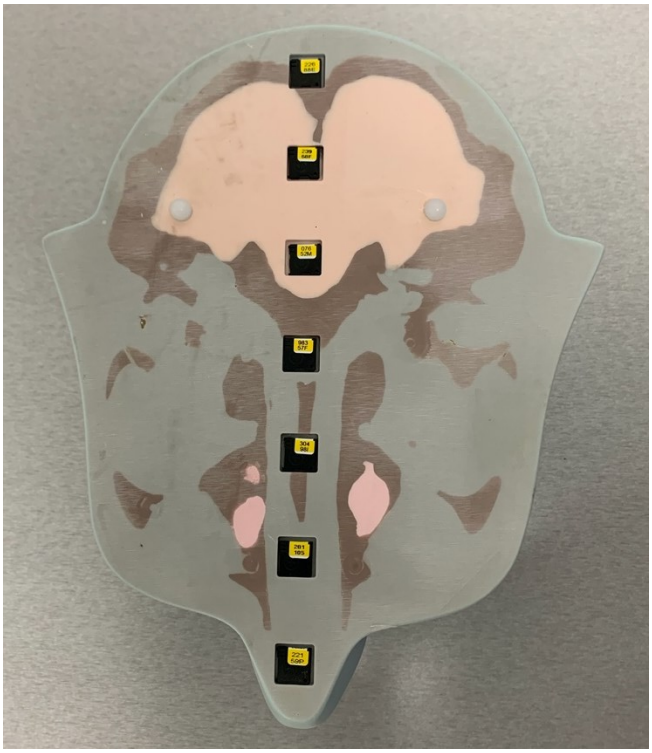

Figure 27. OSLD placement for kV acquisitions in VOI evaluation

4.5 Results

4.5.1 Diamond target beam CBCT image quality

For visual comparison of 2.5 MV diamond versus copper CBCT images, reconstructed slices of the CIRS 062M phantom are provided in Figure 28. CNR versus dose results for various tissue equivalent materials in thin and thick phantoms are provided in Figure 29 below. In these results, we consider a wide range of CBCT imaging dose, i.e., beyond that of interest clinically, to examine trends of the curves. Corresponding CNR values for kV acquisitions are provided in Table 4 for clinically realistic comparisons. In both phantoms, the lung (inhale) insert was the highest contrast material and liver displayed the least contrast across all imaging doses in MV acquisitions. CNR values for bone 200 mg/cc and

liver did not exceed unity in either phantom across the investigated MV dose range and therefore cannot be used to draw meaningful conclusions. The inconsistent behavior of the CNR curves for bone 200 mg/cc and liver in the thick phantom case likely result from combined effects of photon starvation and slightly different detector sensitivities between the two TrueBeam units used to acquire the 2.5 MV diamond target and 2.5 MV commercial target images. In the thin phantom, the 2.5 MV diamond beam demonstrated improvements in CNR for lung (inhale), lung (exhale) and bone 800 mg/cc inserts compared to the commercial imaging beam, across the entire dose range examined. Observed CNR improvements were greater at imaging doses less than 5 cGy in the thin phantom for MV acquisitions. The opposite trend was observed for the thick phantom, where the 2.5 MV diamond and commercial beam CNR curves for lung (inhale) and lung (exhale) inserts were nearly indistinguishable at doses below 5 cGy, however at greater dose values the 2.5 MV diamond beam produced improvements in CNR by factors up to 1.25. In the thin phantom, the 2.5 MV diamond CNR was greater than the commercial imaging beam by factors of up to 1.3 and 1.7 times for the lung and bone 800 mg/cc inserts, respectively, at doses of approximately 2 cGy, for example. At doses beyond 5 cGy, this CNR improvement factor reduced to between 1.15 and 1.25 for the lung and bone 800 mg/cc materials. While the 2.5 MV diamond target beam displays superior CNR compared to the commercial copper target beam, all of the kV acquired CBCTs demonstrated CNR values much higher than what was acquired with the MV beams for a small fraction of the dose (i.e. mGy versus cGy). Compared to the 4.2 MV graphite target beam investigated by Faddegon et al.[19], the CNR of the 2.5 MV diamond target beam was

inferior across all investigated tissue equivalent materials and imaging doses. Despite our comparatively favorable energy spectrum, these discrepancies likely arise from a difference in backscatter conditions, imaging detectors, and/or CNR calculation.

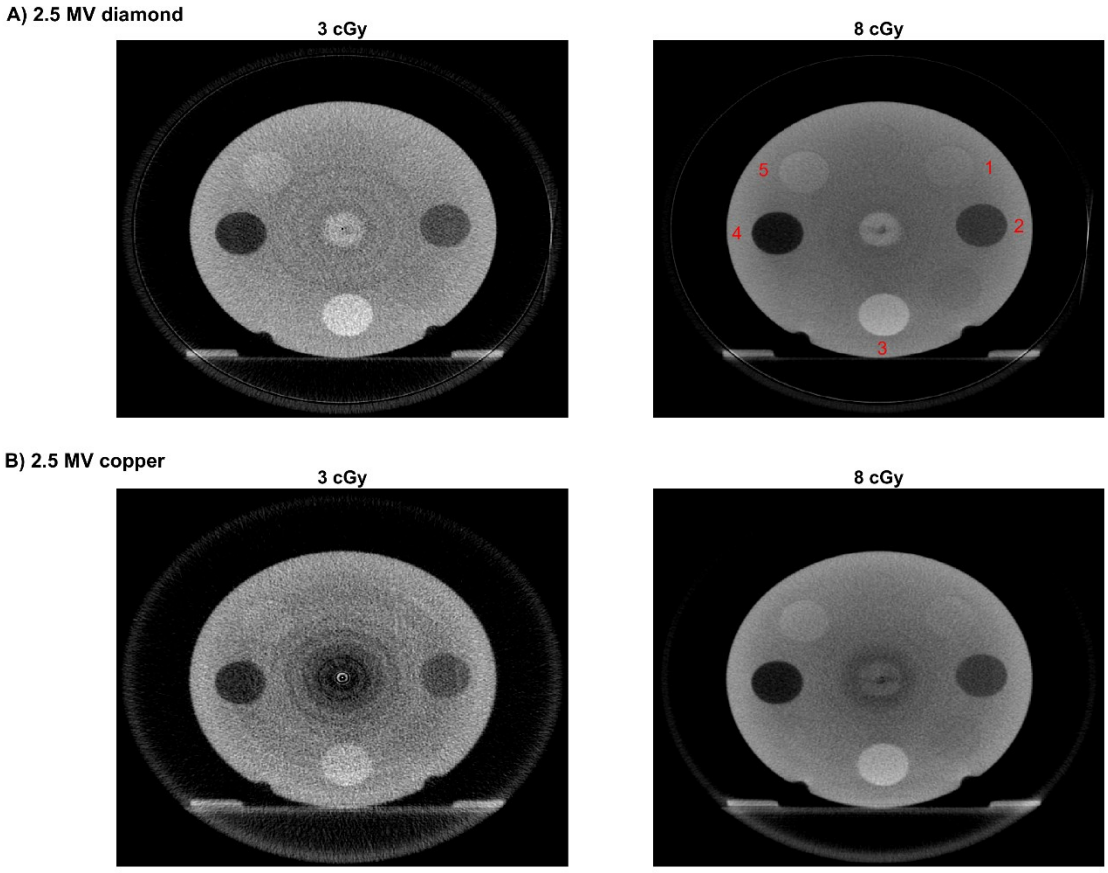

Figure 28. Reconstructed slices of thin CIRS 062M phantom acquired with the A) 2.5 MV diamond target and B) 2.5 MV copper target beams. Tissue equivalent inserts in top right image labeled as: 1) liver, 2) lung (exhale), 3) bone (800 mg/cc), 4) lung (inhale), 5) bone (200mg/cc)

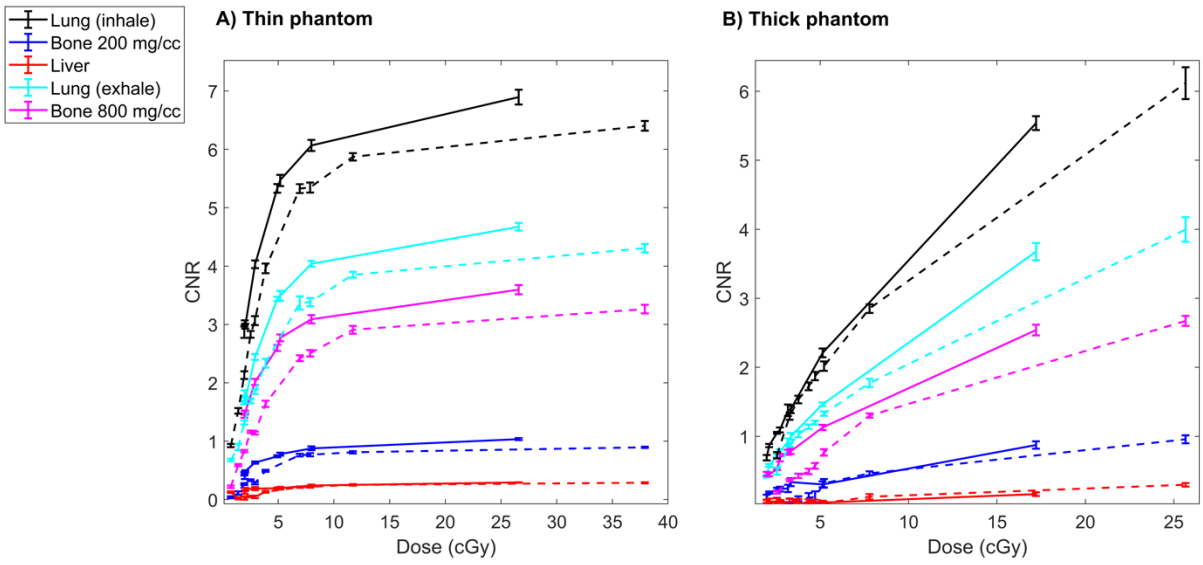

Figure 29. CNR versus dose for a) thin and b) thick phantoms imaged with the 2.5 MV diamond (solid lines) and commercial (dashed lines) imaging beams.

Table 4 CNR results and imaging dose from kV CBCT acquisitions

Imaging protocol	**CNR**					**Imaging dose (mGy)**
	Lung (inhale)	**Bone 200 mg/cc**	**Liver**	**Lung (exhale)**	**Bone 800 mg/cc**	
Head (THIN)	28.8 ± 0.3	11.3 ± 0.2	2.4 ± 0.1	19.9 ± 0.6	28.2 ± 0.2	2.2 ± 0.1
Thorax (THICK)	7.70 ± 0.03	2.70 ± 0.05	0.10 ± 0.01	7.7 ± 0.2	7.4 ± 0.2	2.5 ± 0.1
Pelvis large (THICK)	7.60 ± 0.05	2.50 ± 0.03	0.04 ± 0.02	9.8 ± 0.1	6.8 ± 0.2	22 ± 1

Findings from the spatial resolution analysis are displayed in Figure 30 where panels in A) demonstrate the spatial variation in pixel intensity across the line pair regions for 2.5 MV diamond and commercial reconstructions and B) provide a plot of MTF as a function of spatial frequency. Qualitative comparisons of the plots in panel A) demonstrate a visually larger difference between maximum and minimum pixel intensities for the 2.5 MV diamond profiles compared to the commercial imaging beam across all spatial frequencies. This improvement in modulation is reflected in the calculated MTF curves of panel B), where the 2.5 MV diamond MTF is greater than the commercial beam across all of the investigated spatial frequencies. The frequency at which the MTF drops to 50% of that for the lowest frequency (i.e. f_0), f_{50}, was calculated to be 0.45 lp/mm and 0.35 lp/mm for the 2.5 MV diamond and commercial imaging beams, compared to 0.51 lp/mm for the head protocol, and 0.33 lp/mm for both the thorax and pelvis large protocols.

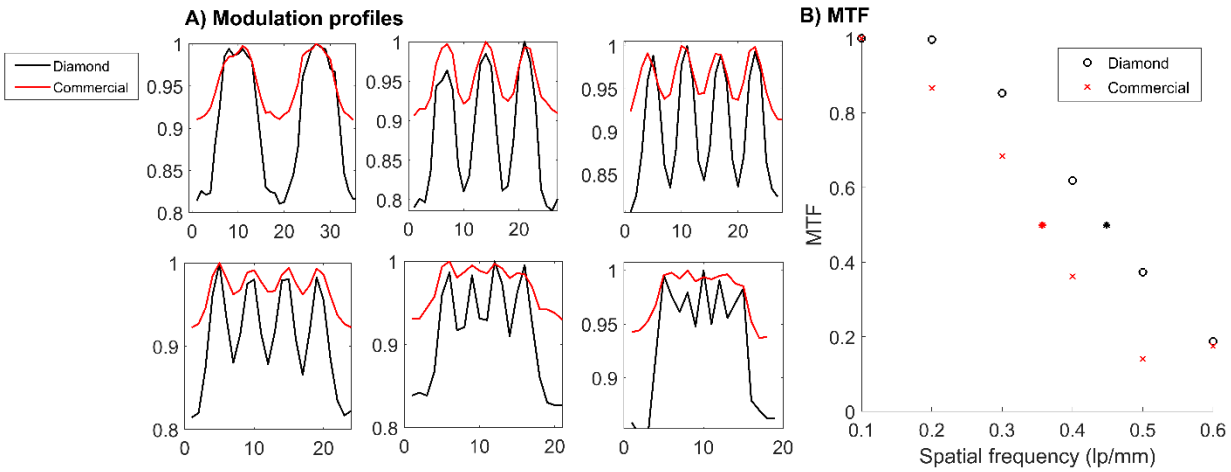

Figure 30. a) Line profiles through line pair regions (1-6 lp/cm) of the reconstructed Catphan CTP528 module acquired with the 2.5 MV diamond and commercial imaging beams and b) calculated MTF for CBCT with 2.5 MV diamond and commercial imaging beams.

4.5.2 Diamond target VOI image quality

Figure 32a) shows the measured CNR, at bone-tissue and bone-sinus interfaces, as a function of the VOI equivalent radius. The bone-tissue CNR increased as a function of VOI radius, from the smallest $VOI_{3\ cm}$ to the full FOV case. A similar trend was observed at the higher contrast bone-sinus interface, excluding the full FOV case which demonstrated decreased CNR compared to $VOI_{3.65\ cm}$, $VOI_{4.3\ cm}$ and $VOI_{4.85\ cm.}$ The difference in the CNR trends at both interfaces can be explained by the behavior of contrast and noise in panels b) and c) of Figure 32. While noise decreases monotonically at both boundaries, the contrast at each interface shows different trends. At the bone-tissue interface, contrast increases as a function of VOI radius and decreases slightly for the full FOV case to 92% of that for $VOI_{4.85\ cm}$. Whereas, at the bone-sinus interface, contrast reaches a maximum at $VOI_{4.3\ cm}$, then decreases as a function of VOI radius to 72% for the full FOV case compared to $VOI_{4.3\ cm}$. This significant drop in contrast accounts for the decrease in CNR at the bone-sinus interface for the full FOV case. The corresponding CNR for the kV acquisition was calculated to be 57.2 ± 0.7 and 21.0 ± 0.7 at the bone-sinus and bone-tissue interfaces, respectively. Figure 31 contains reconstructed axial slices at phantom isocenter for each VOI acquisition for qualitative demonstration.

4.5.3 Diamond target VOI dose analysis

Normalized relative dose profiles taken in the AP direction across each VOI are displayed in Figure 33. While MV imaging doses were normalized to the maximum dose in the full FOV MV acquisition, kV doses have been normalized to the kV dose at the location of the

maximum MV dose in the phantom (i.e. 2 cm from the tip of the nose) to allow both MV VOI profiles and kV measurements to be compared using the same scale. Each 2.5 MV profile was captured through the center of the anthropomorphic phantom in the digitized film images and normalized to the maximum dose in the full FOV profile. Compared to the full FOV profile, a decrease in imaging dose was observed for each of the four VOI cases in the anteroposterior direction. Imaging dose decreased as a function of VOI dimension, with dose reductions within the VOI ranging from 7% to 20%, compared to the full FOV case. Outside of the VOI, imaging doses decreased to 23%, 20%, 15% and 12% of the maximum dose in the full FOV profile. Unlike the MV profiles, kV imaging dose increases with depth in the AP direction, due to the half-trajectory acquisition. For reference, the maximum dose in the kV acquisition was 0.28 cGy.

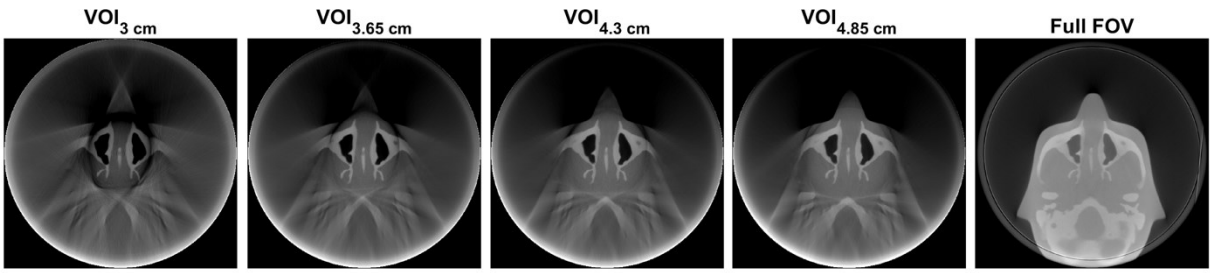

Figure 31. Reconstructed axial slices at phantom isocenter for each VOI acquisition.

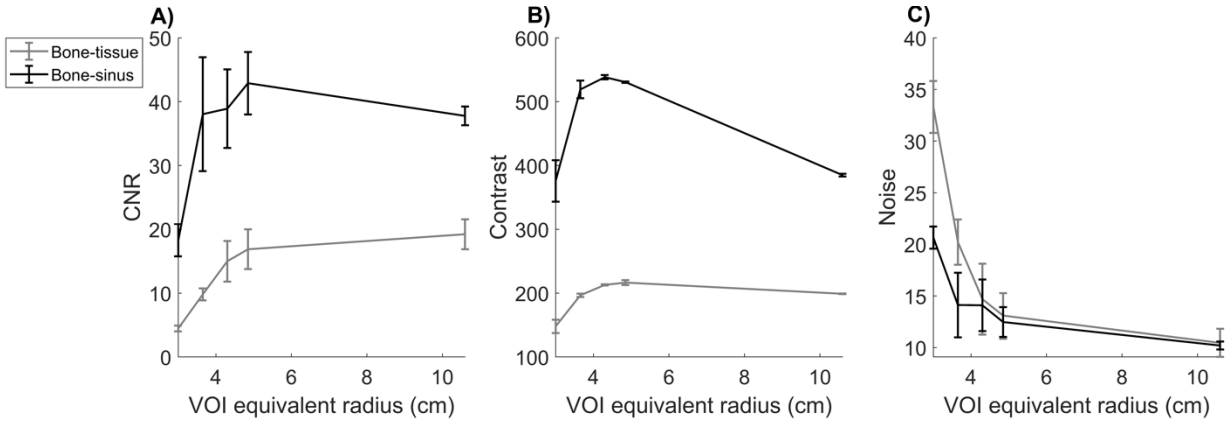

Figure 32. a) CNR, b) contrast, and c) noise versus VOI equivalent sphere radius for bone-tissue and bone-sinus interfaces in the anthropomorphic phantom.

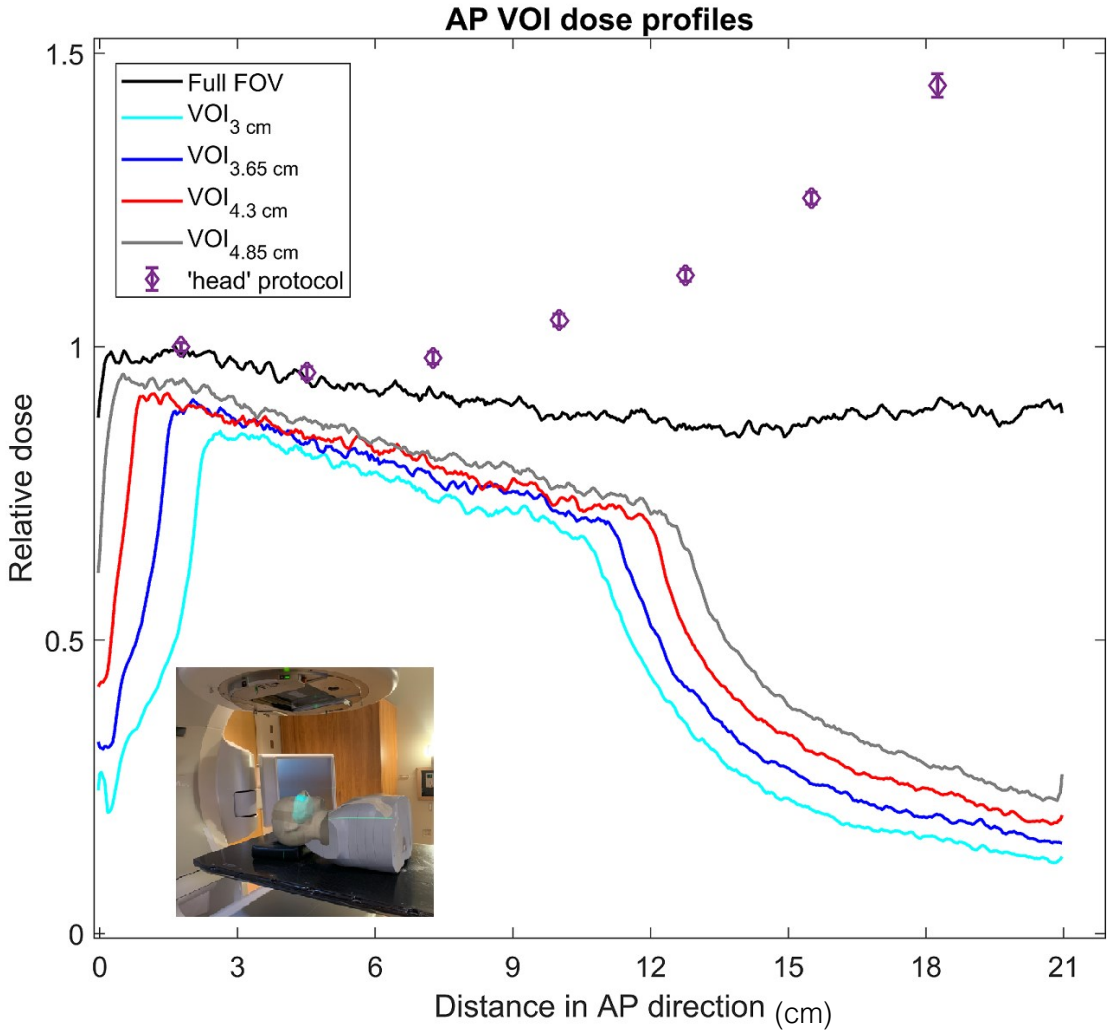

Figure 33. Normalized anteroposterior dose profiles measured from EBT3 film for each VOI, full FOV acquisition, and OSLD doses from kV head protocol acquisition. Distance in AP direction extends from the tip of the nose to the posterior aspect of the cranium. Phantom setup and delineated VOI demonstrated in inset photo in bottom left corner of plot.

4.6 Discussion

In this work we have examined potential advantages of 2.5 MV imaging beam produced with a novel sintered diamond target located in the target arm of a TrueBeam treatment unit. We hypothesized that this beam would provide advantages in terms of CNR per unit imaging dose when used for full-field CBCT imaging, and that further advantages may be realized through a VOI approach. The diamond target beam enables improved image quality in full FOV CBCT imaging, both in terms of CNR and spatial resolution characteristics compared to the commercial imaging beam. The 2.5 MV diamond beam demonstrated increased CNR per unit dose, particularly for the high contrast materials in the thin phantom. Larger improvements in CNR were observed at doses below 10 cGy in the thin phantom. Beyond this threshold CNR begins to saturate as improvements in contrast and noise become more gradual. Conversely, the contrast and noise characteristics in the thick phantom were such that CNR remains comparatively low at doses less than 10 cGy, and further improvements were seen with increasing dose. Due to the difference in CNR improvements with increasing phantom thickness, the 2.5 MV diamond target beam might be best suited for imaging smaller anatomy, such as the head or extremities. Investigation of MTF revealed an increase of nearly 30% in f_{50} for the 2.5 MV diamond beam compared to the commercial beam. These improved 2.5 MV diamond CBCT image quality results are consistent with those observed in planar imaging[101].

As hypothesized, VOI collimation provided peripheral dose sparing in MV CBCT acquisition. Imaging dose at the posterior edge of the $VOI_{3\ cm}$ and $VOI_{4.3\ cm}$ profiles was

reduced by nearly 80% and 65%, respectively, compared to the full FOV dose. Within the VOI itself, imaging dose reductions of up to 20% were observed for the smallest VOI, presumably due to reductions of collimator and patient scatter. In addition to the dose sparing benefits, reconstructed VOI images demonstrated improved CNR at the high-contrast bone-sinus interface compared to that acquired with a full FOV. These results contradict those previously reported by *Robar et al.* who found no significant improvement in CNR with reduced VOI dimension, however that work was conducted with a different target material, target geometry and detector[105]. Further exploration of the 2.5 MV diamond VOI technique could be carried out to determine consistency of these trends in other imaging applications, such as thicker anthropomorphic phantoms and more realistic anatomy, e.g., animal model or cadaver.

The VOI acquisition technique presented in this work could be easily incorporated into the treatment workflow to enable anatomy-specific image guidance, allowing imaging of only the anatomy relevant to the guidance task, while offering both improved image quality and reduced imaging dose. Using the tumor volume as a basis structure, generation of the VOI and corresponding MLC sequence could be automated as part of the setup procedure at the treatment unit. In this work, the VOI technique demonstrated an advantage in CNR at the high-contrast bone-sinus boundary, where the CNR of $VOI_{4.85\ cm}$ was 1.14 times greater than that of the full field case. As such, this technique could be valuable in clinical scenarios involving a clearly defined (i.e. high-contrast) VOI in the

anatomy surrounding the treatment site, e.g. peripheral lung lesions, lumpectomy cavity, or brain tumors where proximal anatomy allows accurate registration.

While this work demonstrates improved image quality per unit dose in MV imaging, our 2.5 MV diamond target beam is still inferior to kV clinical protocols in terms of CNR per unit dose. Due to the underlying physics of bremsstrahlung x-ray production and energy dependent photon interactions, this disparity is inevitable. Despite this physical limitation, this 2.5 MV diamond target imaging may present as a cost-effective solution for CBCT image guidance in emerging markets with limited access to state-of-the-art equipment with on-board imaging. In the modern image guidance workflow, the 2.5 MV diamond target beam could offer the potential for integrated kV and MV CBCT acquisition to reduce artifacts and/or directly measure attenuation maps for online dose calculations, or possibly pave the way for intra-treatment MV imaging using a fast-switching target[112], though this would involve significant engineering challenges. These possibilities motivate the continued development of this MV imaging technology.

Despite the low DQE of the standard as1000 flat-panel detector in the 2.5 MV beamline, current and previous results combined demonstrate improved CNR versus dose characteristics in planar, CBCT and VOI CBCT imaging compared to the commercial beam. It is anticipated that the CNR versus dose relationship could be further improved in all of these acquisition modes through the integration of a high-efficiency multi-layer detector in the 2.5 MV sintered diamond target beamline[99,102].

4.7 Conclusions

This study demonstrated improvements in the CNR versus dose relationships in both full FOV and VOI acquisitions with the 2.5 MV diamond beam compared to the commercial beam. At CBCT doses as low as 2 cGy, CNR improvements of up to 1.7 times were observed in the 2.5 MV diamond images compared to those acquired with the commercial 2.5 MV imaging beam. In addition to the improved contrast characteristics in 2.5 MV CBCT, the sintered diamond beam displayed superior spatial resolution, quantified by the nearly 30% increase in f_{50} compared to the commercial 2.5 MV beam. Volume-of-interest imaging approaches demonstrated some further CNR improvement as well as imaging dose reduction both within and outside of the VOI. In summary, the novel 2.5 MV diamond target beam presents a simple modification to the commercial 2.5 MV imaging beamline which improves image quality and supports the further clinical development of MV CBCT acquisition.

Chapter 5: Investigation of a novel 2.5 MV sintered diamond target beam for intracranial linac-based stereotactic treatments

5.1 Prologue

This manuscript investigates the novel 2.5 MV sintered diamond target beam developed in this thesis for potential applications in stereotactic treatment. Treatments of trigeminal neuralgia and ocular melanoma were simulated using Monte Carlo to determine the dose sparing effects compared to identical plans generated for a clinical 6 MV beam. This work highlights the benefit of the softer 2.5 MV low-Z target energy spectrum, demonstrating reduced penumbra and the effects on dose coverage and sparing in these treatment cases.

This manuscript was published in Biomedical Physics & Engineering Express.

Borsavage, J.M., Cherpak, A.J., Robar, J.L., Investigation of a novel 2.5 MV sintered diamond target beam for intracranial linac-based stereotactic treatments. Biomedical Physics & Engineering Express, vol. 10, 2024.

5.2 Abstract

Purpose: This work investigates the small-field dosimetric characteristics of a 2.5 MV sintered diamond target beam and its feasibility for use in linac-based intracranial stereotactic treatments. Due to the increased proportion of low energy photons in the low-Z beam, it was hypothesized that this novel beam would provide sharper dose fall-off compared to the 6 MV beam owing to the reduced energy, and therefore range, of secondary electrons.

Material and methods: Stereotactic treatments of ocular melanoma and trigeminal neuralgia were simulated for 2.5 MV low-Z and 6 MV beams using Monte Carlo to calculate dose in a voxelized anatomical phantom. Two collimation methods were investigated, including a 5x3 mm^2 HDMLC field and a 4 mm cone to demonstrate isolated and combined effects of geometric and radiological contributions to the penumbral width.

Results: The measured 2.5 MV low-Z dosimetric profiles demonstrated reduced penumbra by 0.5 mm in both the inline and crossline directions across all depths for both collimation methods, compared to 6 MV. In both treatment cases, the 2.5 MV low-Z beam collimated with the 4 mm cone produced the sharpest dose fall-off in profiles captured through isocenter. This improved fall-off resulted in a 59% decrease to the maximum brainstem dose in the trigeminal neuralgia case for the 2.5 MV low-Z MLC collimated beam compared to 6 MV. Reductions to the maximum and mean doses to ipsilateral and

contralateral OARs in the ocular melanoma case were observed for the 2.5 MV low-Z beam compared to 6 MV with both collimation methods.

Conclusions: While the low dose rate of this novel beam prohibits immediate clinical translation, the results of this study support the further development of this prototype beam to decrease toxicity in intracranial SRS treatments.

5.3 Introduction

A primary challenge in many modern stereotactic treatments is the dose fall-off immediately beyond the surface of the target volume. While this issue has always existed, high dose fall-off has become a limiting factor in improving the accuracy of high dose delivery in stereotactic radiosurgery (SRS), stereotactic radiotherapy (SRT), and stereotactic body radiotherapy (SBRT) due to the reduction of clinical treatment margins with improved image guidance. Dose fall-off immediately beyond the prescription isodose surface is dictated by two factors: i) geometric penumbra and ii) radiological penumbra[113]. The first contributor can be minimized using conical collimation which matches beam divergence or multileaf collimator (MLC) leaf design that reduces partial attenuation of the beam through the leaf end, as well as minimizing the distance from the collimator to the target[51]. The second factor is determined by the range of electrons set into motion, which broadens beam penumbrae[58]. For small fields used in stereotactic treatments, the radiological penumbra widens as photon energy increases due to the loss of lateral charged particle equilibrium (CPE) at the field edge. This lack of CPE results in

more secondary electrons being scattered outside of the field edge than those scattered inwards, resulting in decreased dose deposited inside the field edge and increased dose deposited outside of the geometric field[73]. Despite 6 MV being widely accepted as the ideal radiotherapy treatment energy[31], previous studies[29,32] have shown that for small fields, lower megavoltage energy beams have sharper radiological penumbra, which may be advantageous in the delivery of conformal stereotactic treatments. The recently commercialized Zap-X radiosurgical platform (Zap Surgical San Carlos, CA) exploits these advantages, utilizing a 3 MV treatment beam. Combined with the shortened source-to-axis distance (SAD) of 45 cm, the 3 MV beam offers reduced penumbra compared to a 6 MV conically collimated field[75]. At 5 cm depth, the 90%-10% penumbral width for the Zap-X beam collimated to a 4 mm diameter field is 1.78 mm[75] compared to 1.94 mm for a 4 mm conically collimated 6 MV beam on a TrueBeam[114].

Following the same rationale motivating the Zap-X platform, recent studies[34–36] have examined the use of the 2.5 MV beam on the TrueBeam platform for potential treatment applications in both standard and stereotactic treatment planning. Though this beam is dedicated exclusively for imaging, both studies concluded a dosimetric advantage in terms of sparing of organs at risk (OARs) for the 2.5 MV beam compared to identical plans generated for the 6 MV treatment beam, due to the decreased scatter of secondary electrons. Motivated by the results from these studies, our current work aims to investigate the use of a novel 2.5 MV low-Z sintered diamond target beam in linac-based intracranial stereotactic treatments. Owing to the decreased self-absorption of diagnostic

energy photons (i.e. 25-150 keV) within the low-Z target, the sintered diamond target beam yields a larger proportion of low-energy photons compared to the conventional 2.5 MV beam[23]. Previous work with this 2.5 MV sintered diamond target beam demonstrated improved contrast-to-noise ratio (CNR) versus dose compared to the commercial imaging beam, resulting from the softer low-Z spectrum[101,115]. We hypothesize that this novel 2.5 MV sintered diamond target beam would be advantageous in intracranial stereotactic treatments compared to the conventional 6 MV beam due to the decreased lateral scatter of lower energy secondary electrons, producing sharper penumbra and therefore improved dose fall-off. Due to the softer low-Z spectrum, it was reasoned that this novel beam would benefit peripheral dose fall-off compared to the conventional 2.5 MV beam, and therefore, the conventional 2.5 MV beam was excluded in this study. In addition to the effects of beam energy, this study examines two different collimation methods (i.e. stereotactic cone and MLC) to demonstrate the isolated and combined effects of reducing radiological and geometric penumbra contributions using Monte Carlo methods to simulate treatment of trigeminal neuralgia and ocular melanoma.

5.4 Material and Methods

5.4.1 Low-Z sintered diamond target

The low-Z target was assembled in-house and installed on a TrueBeam STx unit, as previously described[101]. The target is made of a disk of sintered diamond, 13.44 mm in diameter and 5 mm thick, with a density of 3.35 g/cm^3. Upon installation, the 2.5 MV

imaging beam was removed from clinical service and reserved exclusively for research purposes.

5.4.2 Stereotactic beams and collimation

Four stereotactic beams were investigated in this work including a novel 2.5 MV sintered diamond target beam (denoted as 2.5 MV low-Z, herein) and 6 MV, each with either conical or HDMLC collimation. This experimental design exemplifies the individual and combined effects of reducing the radiological and/or geometric contributions to penumbra. The smallest clinical stereotactic cone (i.e. 4 mm in diameter) was chosen to demonstrate the most significant case of lateral charged particle disequilibrium. To ensure fair comparisons between HDMLC and cone collimated fields, the HDMLC aperture was chosen to approximate the equivalent square field of the 4 mm circular field. This field was shaped by two opposing HDMLC leaf (2.5 mm wide) pairs forming a 5x3 mm^2 field, corresponding to an equivalent square field side of 3.75 mm versus 3.54 mm for the cone.

5.4.3 Relative Dosimetry

Each beam was characterized in terms of percent depth dose (PDD) at 90 and 100 cm SSD and off-axis profiles at various depths including: 0.2 cm, 0.5 cm, 1.5 cm, 5 cm, 10 cm, and 20 cm for 2.5 MV low-Z and 0.8 cm, 1.5 cm, 5 cm, 10 cm, and 20 cm for 6 MV. All profiles were measured with a PTW 61009 microdiamond detector (PTW Freiburg, Germany) with the detector face oriented parallel to the central axis. Off-axis profiles were also

measured with calibrated EBT3 film (Ashland Advanced Materials, Bridgewater, NJ) and spot-checked at 5 cm depth using an in-house scintillator[116] to ensure consistency. The cylindrical scintillator had dimensions of 1 mm in diameter and 2.5 mm in height to minimize volume averaging. Scintillator measurements captured five points along a given profile corresponding to the central axis (CAX) and four symmetric points about the CAX. For 6 MV, these points correspond to 2 mm and 5 mm on either side of the CAX, capturing the umbra, penumbra, and in-field regions of the profile. Due to the low dose rate of the 2.5 MV beam and collection time limitations in the spectrometer software, 2.5 MV low-Z measurements were captured at 0.5 mm and 1.5 mm from the CAX. Each scintillator measurement was corrected for fluorescence and Cherenkov using the method described by Lynch et al.[116].

5.4.4 Monte Carlo models

The Monte Carlo framework consisted of three sequential simulations beginning in Varian's VirtuaLinac[85] system to model the proprietary field independent portion of the TrueBeam treatment head. VirtuaLinac phase spaces were scored at a plane located above the jaws, 733 mm from isocenter, and used as input to EGSnrc BEAMnrc to model particle transport through the remaining treatment head geometry. The resultant BEAMnrc phase spaces were propagated through a tertiary geometry in dosxyznrc to calculate dose in a voxelized phantom. The dimensions and material properties of the custom 2.5 MV sintered diamond target were modeled to manufacturer's specifications in VirtuaLinac. Phase spaces for the 6 MV beam were generated in VirtuaLinac using

directional bremsstrahlung splitting to improve statistics in downstream dose calculations. The 6 MV phase space was created using identical parameters as those used to generate the open-source phase space files[69]. As such, the 6 MV beam model was used without validation under the presumption that the model represented 'golden beam data' (i.e. representative of typical clinical 6 MV beam)[117].

Two BEAMnrc input files were generated for each beam energy to model conical or HDMLC collimation. The 4 mm cone was modeled to manufacturer specifications and the TrueBeam HDMLC was defined based on engineering drawings sourced from the TrueBeam Monte Carlo Data Package[118]. For simplicity, the HDMLC model contained only the central 32 leaves, encompassing the 5x5 cm^2 field collimated by the jaws. Prior to treatment simulation, the 2.5 MV low-Z models were validated against measured beam data using a gamma evaluation with 1.5%/1 mm dose and distance-to-agreement criteria, respectively.

5.4.5 Treatment planning framework

Treatment plans were generated in Eclipse using open-source anonymized patient data[119]. Mock targets were created to realistically imitate treatment volumes for ocular melanoma (OM) and trigeminal neuralgia (TN) according to anatomical placement and volume. These sites were chosen due to their proximity to delicate structures, and to capture a range of treatment depths. The OM treatment volume was contoured to represent a tumor at the posterior aspect of the choroid with an equivalent sphere

diameter of 3 mm, replicating a small sized tumor as defined by the Collaborative Ocular Melanoma Study (COMS). The TN target was localized to the nerve root and contoured to be 30 mm^3.

Optimal beam placement was determined using a forward-planning approach to arrange static non-coplanar fields in a commercial treatment planning system (Eclipse v15.6, Varian Medical Systems). Both TN and OM plans were created using the 6 MV HDMLC field in the treatment planning system (TPS). The OM plan was generated to deliver 50 Gy in 5 fractions with planning target volume (PTV) coverage of 45 Gy or more to 98% of the volume (i.e. $D_{98\%} \geq 45$ Gy). The TN plan was designed with the following objectives: 1) deliver a maximum point dose of 90 Gy to the PTV, 2) $V_{45\ Gy} = 100\%$ (i.e. PTV encompassed by 50% isodose) and 3) maintain maximum brainstem point dose below 16 Gy. The resultant plans contained 16 and 13 static fields for the TN and OM cases, respectively.

Treatment deliveries were simulated for all four beam models (i.e. 2.5 MV low-Z and 6 MV collimated with HDMLC or cone collimation), as planned in the TPS with the 6 MV HDMLC field, amounting to eight total simulated treatments. Dose was scored in a voxelized anatomical phantom created using EGSnrc's ctcreate user code to define the geometric bounds and convert CT number to corresponding material properties using a ramp based on HU values observed in the TPS. The computational phantom was constructed with uniform 0.5 mm voxel dimensions to provide adequate resolution to demonstrate differences in dose distributions particularly in the fall-off regions. The number of histories was increased to provide < 1% uncertainty in the calculated dose at

isocenter. Due to the finite size of the phase spaces used in these simulations, particles were recycled as needed to produce the desired statistics. Each particle was recycled a maximum of 20 times in both BEAMnrc and dosxyz simulations. The resultant dose distributions for 6 MV yielded 0.5% statistical uncertainty, whereas 2.5 MV low-Z distributions had a statistical uncertainty of 0.7%. The calculated 3ddose files were analyzed in 3D slicer[120,121] to compare dose distributions and calculate corresponding dose volume histogram (DVH) metrics for the PTV and surrounding OARs. Prior to analysis, dose distributions were scaled in the software to produce the same PTV dose coverage, enabling meaningful comparisons.

5.5 Results

5.5.1 Relative dosimetry

All profiles measured with the microdiamond, gafchromic film and plastic scintillator were in good agreement. The beam qualities, as characterized by the PDD at 100 cm SSD and 10 cm depth, were 35.9%, 34.6%, 54.3%, and 54.8% for the 2.5 MV low-Z cone, 2.5 MV low-Z HDMLC, 6 MV cone and 6 MV HDMLC collimated beams, respectively. The corresponding depth of maximum dose was 0.38 cm, 0.38 cm, 0.89 cm, and 1.0 cm for the respective beams. The penumbral width and full width at half maximum (FWHM) of measured crossline and inline profiles for each beam are summarized in Table 5 and Table 6 below.

Table 5 Measured penumbra ($P_{90/10}$) and full width at half maximum (FWHM) for conically collimated beams

Beams	**6 MV**				**2.5 MV low-Z**			
Depth	$P_{90/10}$ Crossline (cm)	FWHM Crossline (cm)	$P_{90/10}$ Inline (cm)	FWHM Inline (cm)	$P_{90/10}$ Crossline (cm)	FWHM Crossline (cm)	$P_{90/10}$ Inline (cm)	FWHM Inline (cm)
0.2 cm	-	-	-	-	0.12	0.31	0.13	0.29
0.5 cm	-	-	-	-	0.13	0.31	0.13	0.28
0.8 cm	0.20	0.34	0.20	0.32	-	-	-	-
1.5 cm	0.21	0.35	0.20	0.32	0.13	0.32	0.14	0.29
5 cm	0.23	0.36	0.23	0.33	0.14	0.33	0.15	0.31
10 cm	0.25	0.38	0.24	0.35	0.14	0.36	0.16	0.33
20 cm	0.27	0.41	0.28	0.38	0.18	0.39	0.20	0.36

* $P_{90/10}$ is distance between 90% and 10% dose points on normalized profile
*FWHM is defined as the distance between 50% dose points on either side of the central axis

Table 6 Measured penumbra ($P_{90/10}$) and full width at half maximum (FWHM) for HDMLC collimated beams

Beams	**6 MV**				**2.5 MV low-Z**			
Depth	$P_{90/10}$ Crossline (cm)	FWHM Crossline (cm)	$P_{90/10}$ Inline (cm)	FWHM Inline (cm)	$P_{90/10}$ Crossline (cm)	FWHM Crossline (cm)	$P_{90/10}$ Inline (cm)	FWHM Inline (cm)
0.2 cm	-	-	-	-	0.17	0.26	0.21	0.41
0.5 cm	-	-	-	-	0.19	0.27	0.21	0.42
0.8 cm	0.32	0.36	0.28	0.43	-	-	-	-
1.5 cm	0.36	0.37	0.29	0.44	0.19	0.28	0.22	0.42
5 cm	0.39	0.39	0.32	0.46	0.19	0.29	0.24	0.44
10 cm	0.42	0.42	0.33	0.49	0.22	0.31	0.27	0.46
20 cm	0.46	0.46	0.39	0.54	0.27	0.35	0.33	0.52

* $P_{90/10}$ is distance between 90% and 10% dose points on normalized profile
*FWHM is defined as the distance between 50% dose points on either side of the central axis

The penumbra for the 2.5 MV low-Z cone collimated beam was 0.5 mm narrower compared to the 6 MV beam with the same collimation, across all common depths in the inline and crossline directions. The FWHM of crossline and inline profiles was reduced for the 2.5 MV low-Z cone collimated beam compared to the 6 MV cone collimated beam.

Similar differences in penumbral width and FWHM were observed for the HDMLC collimated beams.

5.5.2 2.5 MV low-Z beam model validation

The validation of the 2.5 MV low-Z models was an iterative process involving beam parameter specification in VirtuaLinac and quantification of agreement between measured and resultant calculated profiles. Changes to beam parameters between iterations was informed by the observed agreement in both PDD and off-axis profiles. The 2.5 MV low-Z beam models were validated using a gamma evaluation with criteria of 1.5% and 1 mm with a required pass rate exceeding 90%. This was met in both 2.5 MV low-Z models across all depths, except the HDMLC model crossline profile at 20 cm depth, as shown in Table 7, below. Upon re-evaluation, excluding the umbra region of the curve, the 20 cm crossline profile had a pass rate of 94.1%. The validated 2.5 MV low-Z models utilized an incident electron energy of 2.3 MeV with a 0.1 MeV energy sigma and focal spot size of 0.8999 mm in the x-direction and 0.956 mm in the y-direction.

Table 7 2.5 MV low-Z gamma pass rates for profiles with conical and HDMLC collimation

Depth	Inline (cone)	Crossline (cone)	Inline (HDMLC)	Crossline (HDMLC)
0.2 cm	91.3%	93.2%	96.0%	96.1%
0.5 cm	91.9%	94.8%	97.0%	96.0%
1.5 cm	93.9%	92.2%	91.3%	94.8%
5 cm	92.9%	93.2%	97.0%	96.0%
10 cm	96.1%	94.9%	98.0%	96.0%
20 cm	93.2%	96.0%	92.9%	49.5%*

* 94.1% for points D>10%

5.5.3 Treatment simulation and dose analysis

5.5.3A Trigeminal Neuralgia plan

Figure 34 illustrates two-dimensional dose distributions at isocenter in the axial, coronal, and sagittal planes, along with corresponding relative dose profiles captured through isocenter for each of the four beams in the TN case. As hypothesized, the 2.5 MV low-Z cone provided the sharpest dose fall-off in all three planes compared to 6 MV with both HDMLC and conical collimation, as well as the 2.5 MV low-Z HDMLC beam. Dose-volume histograms (DVHs) for the TN treatment volume and brainstem are provided below in Figure 35. The DVHs were calculated for distributions that were normalized to satisfy the PTV coverage requirement of $V_{45Gy} = 100\%$. The resultant distributions contained hotspots in the PTV of 121% and 186% for the 6 MV cone and 2.5 MV low-Z cone collimated beams, respectively.

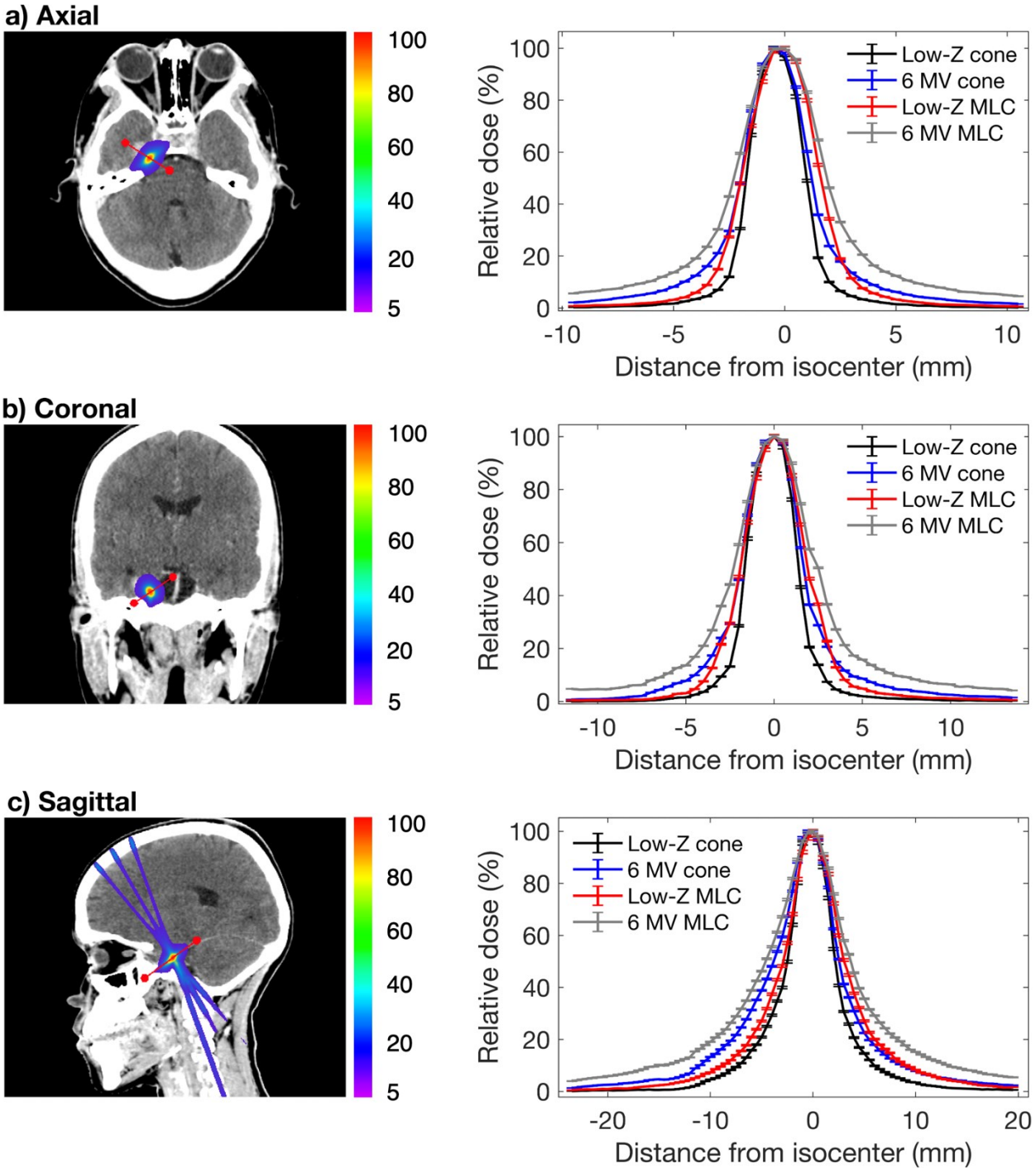

Figure 34. Calculated dose profiles in the a) axial b) coronal and c) sagittal planes for the trigeminal neuralgia plan captured along red line segment in cross-sectional images.

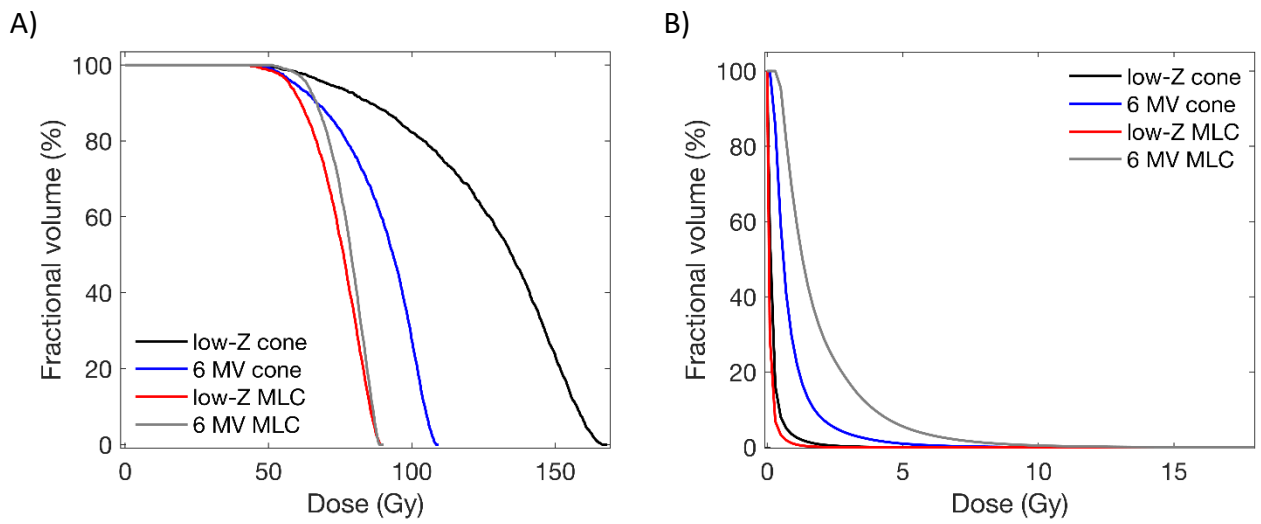

Figure 35. Dose-volume histogram (DVH) comparison of A) PTV and B) brainstem structures for trigeminal neuralgia plan with 4 mm cone and 5x3 mm2 HDMLC collimation to achieve the same PTV coverage of $D_{100\%} \geq 45$ Gy.

Maximum doses to the PTV and brainstem for all four beams providing the same PTV coverage in the TN case are provided in Table 8 below. Based on the significant inhomogeneity in the 2.5 MV low-Z cone collimated DVH, it is evident that the 30 mm^3 target is too large for treatment with the 2.5 MV low-Z beam collimated with the 4 mm cone. While this target was better suited for treatment with a larger cone to maintain reasonable maximum point dose to the PTV, the significantly reduced brainstem dose in the 2.5 MV low-Z cone distribution suggests that a larger cone may still be advantageous compared to the 6 MV 5x3 mm^2 HDMLC collimated beam, given adequate PTV coverage.

Table 8 Maximum brainstem and PTV doses in Gy for the TN plan with the same PTV coverage

	PTV	Brainstem
6 MV HDMLC	90.0	16.0
6 MV cone	109.2	11.4
Low-Z HDMLC	90.0	6.6
Low-Z cone	168.0	5.6

5.5.3B Ocular melanoma plan

Figure 36 displays sample dose distributions in axial, coronal and sagittal planes with resultant relative dose profiles captured along the red line segment in each image for the OM case. Before analyzing results, the dose distributions for each beam were set to provide the same dose coverage to the PTV as achieved in the 6 MV HDMLC plan to produce comparative distributions.

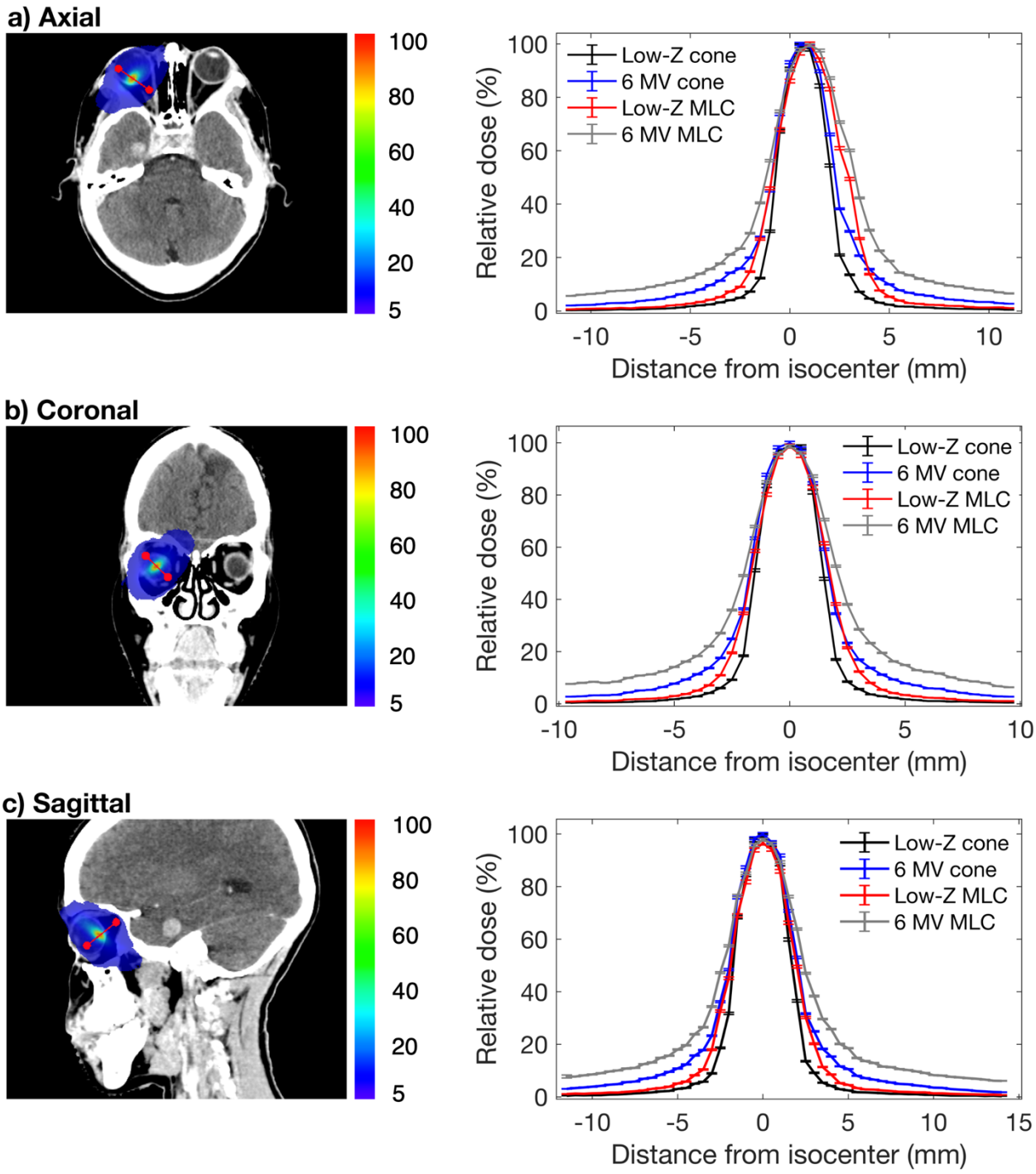

Figure 36. Calculated dose profiles in the a) axial, b) coronal and c) sagittal planes for the ocular melanoma treatment plan delivered with 2.5 MV low-Z and 6 MV beams to achieve the prescribed PTV dose coverage in each distribution. Profiles captured along red line segment in cross-sectional images.

Maximum and mean doses to relevant ipsilateral and contralateral OARs are included in Table 9 and Table 10. DVHs for the PTV and ipsilateral OAR structures including the right eye, right optic nerve, and right lens are provided in Figure 37. The maximum dose for the 2.5 MV low-Z cone collimated beam was 73.67 Gy, compared to 62.86 Gy, 63.54 Gy, and 56.62 Gy for 2.5 MV low-Z HDMLC, 6 MV cone and 6 MV HDMLC collimated beams. Using the 6 MV HDMLC maximum dose as a reference, these hotspots correspond to 130%, 111%, and 112% of the prescription dose for the respective beams. In terms of the prescription dose of 50 Gy, the maximum doses in each plan are 147%, 126%, 127%, and 113% for the 2.5 MV low-Z cone, 2.5 MV low-Z HDMLC, 6 MV cone and 6 MV HDMLC beams. The maximum dose in the 2.5 MV low-Z HDMLC plan is only 1% different from that for the 6 MV cone. Despite delivering the highest absolute dose, the dose fall-off was sharpest in the 2.5 MV low-Z cone distribution, as demonstrated in the dose profiles in all three planes. Conversely, the 6 MV HDMLC beam delivered the lowest dose (i.e. 56.62 Gy) to achieve target coverage but demonstrated the broadest penumbra. The coronal and sagittal profiles for the 6 MV cone collimated and 2.5 MV low-Z HDMLC collimated fields were nearly indistinguishable for doses > 20%. The mean dose to the right eye was lowest in the 2.5 MV low-Z cone distribution and highest in the 6 MV HDMLC plan. This trend was consistent across all mean and maximum doses to the OARs in Table 9 and Table 10.

Though the 2.5 MV low-Z cone collimated beam produced the largest hotspot within the PTV, it also provided the best sparing of right lens, right optic nerve, optic chiasm, left

eye, left lens and left optic nerve. In the ipsilateral structures, the maximum doses to the lens and optic nerve were reduced by 86% and 82%, respectively, in the 2.5 MV low-Z cone distribution compared to the reference 6 MV HDMLC distribution. Larger differences were observed in the contralateral structures, where maximum doses to the OAR structures for the 2.5 MV low-Z cone collimated beam were $\leq$ 5% of what was delivered by the 6 MV HDMLC collimated beam. The DVH for the PTV demonstrates similar dose coverage for the 2.5 MV low-Z HDMLC and 6 MV cone collimated beams across the range of doses. Both cone collimated beams delivered higher maximum doses to the PTV compared to the 6 MV HDMLC collimated beam while also providing better dose sparing to OARs, as evidenced by the maximum and mean doses.

Table 9 Maximum OAR doses in Gy for each beam in OM plan

	Eye (R)	Lens (R)	Optic Nerve (R)	Chiasm	Eye (L)	Lens (L)	Optic Nerve (L)
6 MV HDMLC	56.62	6.93	12.56	0.29	1.56	0.76	0.44
6 MV cone	63.54	4.13	7.54	0.10	0.67	0.18	0.12
Low-Z HDMLC	62.86	1.53	4.69	0.04	0.36	0.05	0.05
Low-Z cone	73.67	0.96	2.29	0.01	0.24	0.07	0.04

Table 10 Mean OAR doses in Gy for each beam in OM plan

	Eye (R)	Lens (R)	Optic Nerve (R)	Chiasm	Eye (L)	Lens (L)	Optic Nerve (L)
6 MV HDMLC	8.96	4.26	2.27	0.14	0.48	0.54	0.20
6 MV cone	6.12	2.00	0.74	0.04	0.09	0.09	0.06
Low-Z HDMLC	4.14	0.67	0.39	0.01	0.05	0.11	0.02
Low-Z cone	3.11	0.37	0.21	0.00	0.02	0.02	0.01

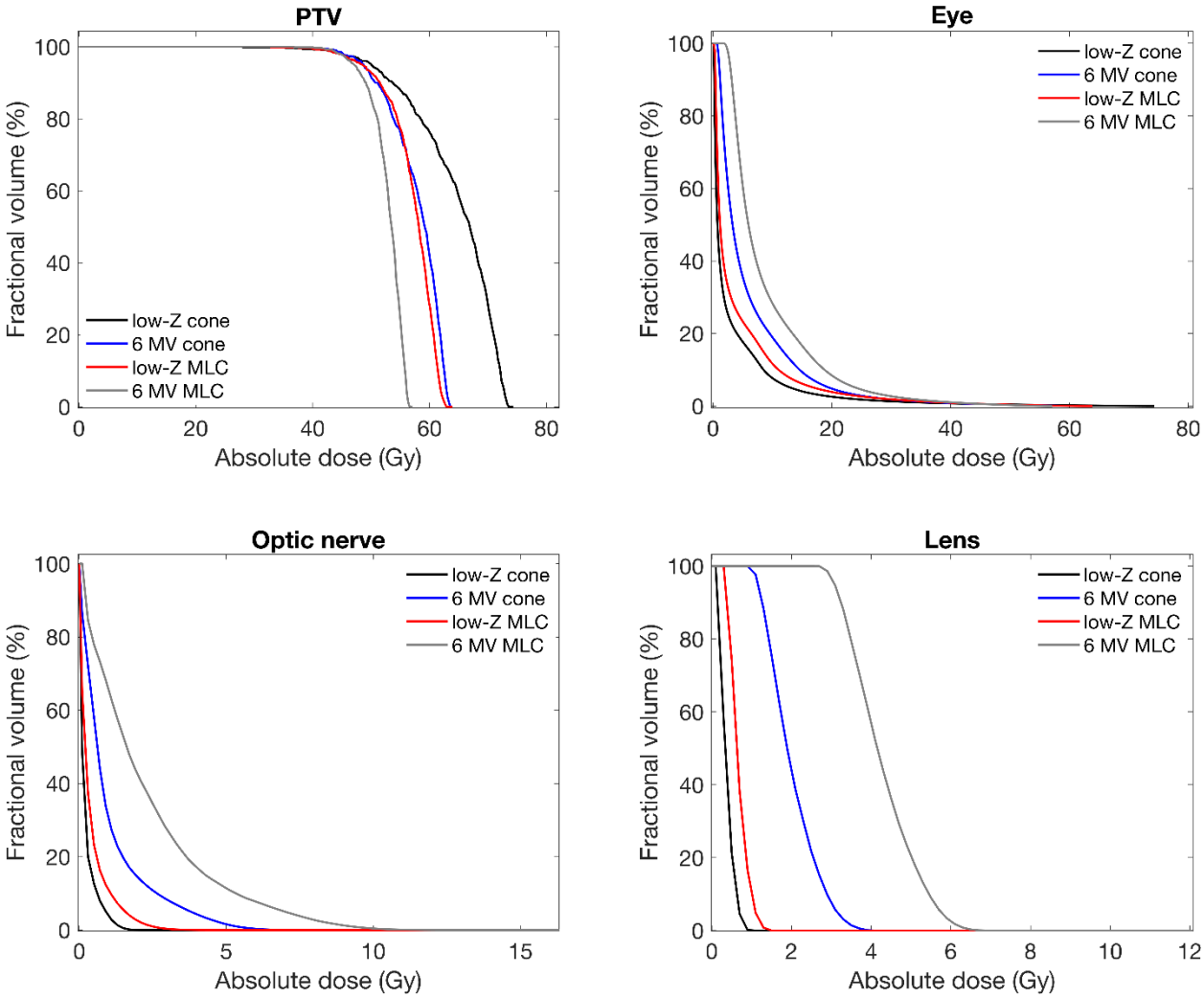

Figure 37. Dose-volume histogram (DVH) comparison of PTV and ipsilateral (right) OAR structures for ocular melanoma plan for equivalent PTV coverage ($V_{98\%}$ = 45 Gy).

Figure 38 displays comparative dose distributions for the OM plan at isocenter in each of the three planes for all four beams. Qualitative review of these distributions demonstrates improved dose compactness in the cone collimated fields compared to the HDMLC collimated fields for both 6 MV and 2.5 MV low-Z beams. Dose is most compact in the 2.5 MV low-Z cone distribution compared to the other three beams, as hypothesized. As anticipated, the distributions illustrate the improved dose fall-off in

cone collimated fields compared to HDMLC collimated fields for both 2.5 MV low-Z and 6 MV beams. This observation is contributed partly by the decreased field size of the cone compared to the HDMLC aperture (i.e. equivalent square field size of 3.54 mm versus 3.75 mm). Similarly, the comparison between dose distributions for the 2.5 MV low-Z beam versus 6 MV with the same collimation illustrates the improved dose fall-off contributed by the decreased radiological penumbra, resulting from the softer 2.5 MV low-Z spectrum.

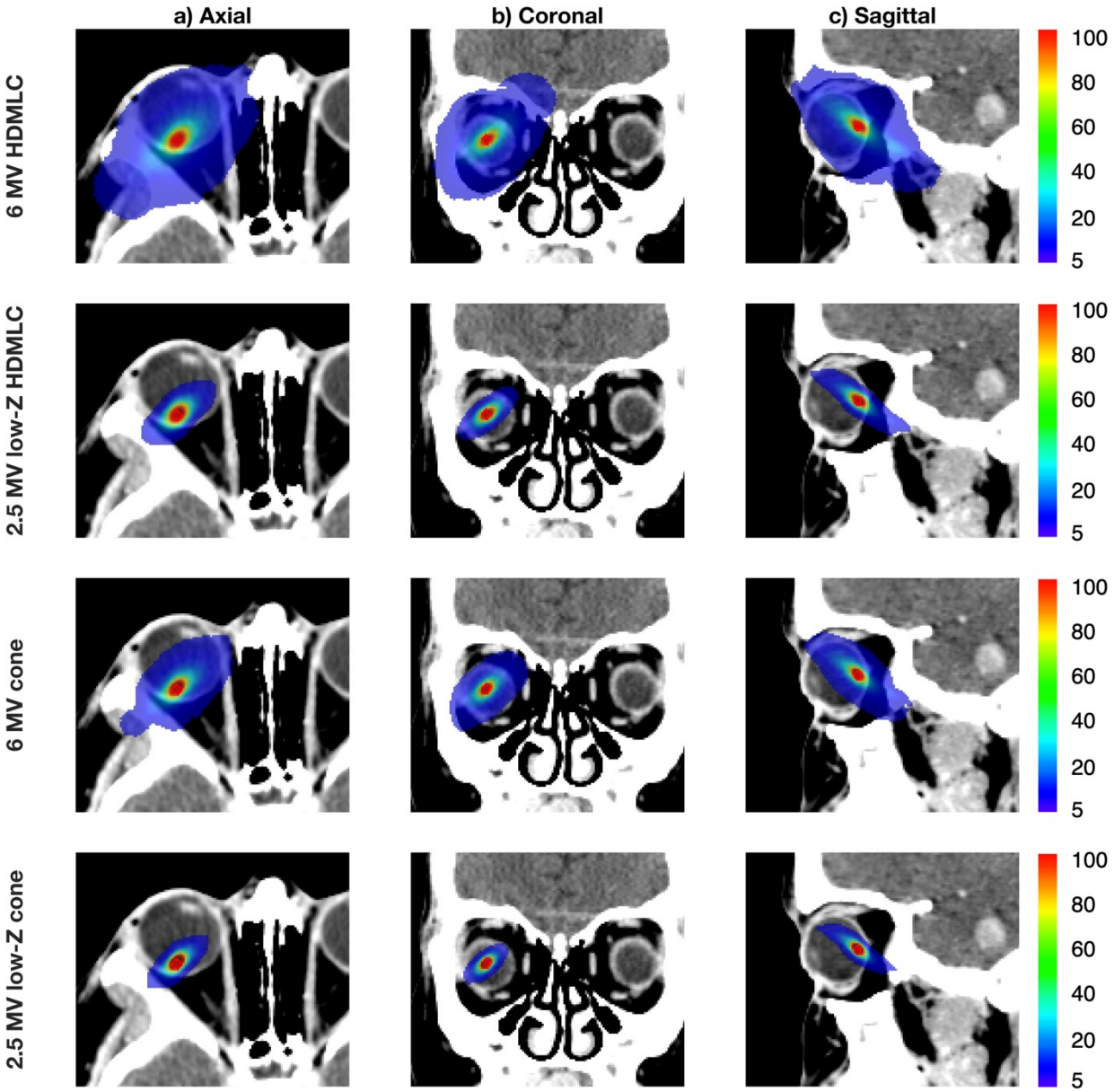

Figure 38. a) Axial, b) coronal, and c) sagittal slices of ocular melanoma dose distributions for the 6 MV HDMLC, 6 MV cone, 2.5 MV low-Z HDMLC, and 2.5 MV low-Z cone collimated beams.

5.6 Discussion

The results of this work supported the hypothesis that the 2.5 MV sintered diamond target beam provided improved dose fall-off compared to the clinical 6 MV beam with both cone and HDMLC collimation. The measured profiles demonstrated reductions in

the penumbral widths of greater than 0.5 mm for 2.5 MV low-Z compared to 6 MV with both collimation methods across all common depths. In addition to improvements in penumbra, the FWHM of 2.5 MV low-Z profiles was reduced compared to 6 MV. These findings are inconsistent with those reported for the 2.5 MV commercial beam with 4 mm conical collimation, which demonstrated a constant 4 mm FWHM independent of beam energy[35]. Consistent with relative dose measurements, the dose profiles through isocenter for both treatment cases showed sharper dose fall-off for 2.5 MV low-Z beams compared to 6 MV. As expected, the 2.5 MV low-Z beam with conical collimation provided the sharpest dose fall-off, owing to the combined effects of decreased radiological and geometric penumbra as well as decreased scatter due to small field size differences (i.e. equivalent square field size of 3.75 mm versus 3.54 mm).

In the TN case, the 2.5 MV low-Z HDMLC collimated beam provided similar PTV coverage to 6 MV while also reducing the maximum dose to the brainstem by 59%. Though the PTV was infeasibly large for the 4 mm cone, the 65% reduction in brainstem dose suggests that a larger cone may still prove advantageous compared to the 6 MV HDMLC collimated beam. The 2.5 MV low-Z HDMLC and 6 MV cone collimated beams provided nearly identical PTV coverage in the OM case, with hotspots of 111% and 112%, respectively. Despite similar maximum PTV doses, the 2.5 MV low-Z HDMLC collimated beam produced a more compact dose distribution which better spared all ipsilateral and contralateral structures. The 2.5 MV low-Z beam showed significantly sharper beam profiles for both

cone and HDMLC collimation at both shallow and deep intracranial depths, as demonstrated in the OM and TN cases, respectively.

At 5 cm depth, the penumbral width of the 2.5 MV low-Z beam collimated with a 4 mm cone was 1.4 mm compared to 1.78 mm for the 3 MV beam on the Zap-X platform[75]. This improved dose fall-off suggests that this novel 2.5 MV low-Z linac beam could provide dosimetric advantages over the 3 MV Zap-X beam, though further investigation is warranted to make direct comparisons between these modalities.

The treatment plans developed in this work utilized 13 and 16 static non-coplanar fields for stereotactic treatment of ocular melanoma and trigeminal neuralgia, respectively. This delivery method was chosen to simplify the simulation of treatment compared to dynamic methods. Non-coplanar arrangements prioritize the intersection of beams at the target while minimizing overlap of beam entrance and exit dose. Compared to coplanar fields, the reduced overlap of entrance and exit dose in non-coplanar fields reduces the dose contributions to normal tissues in the peripheral anatomy, allowing escalated dose to the treatment volume and sparing of normal tissues. While coplanar beam arrangements impact the dose gradient in a single plane, non-coplanar beam arrangements effect the dose gradient in several planes, by spreading the additive penumbral contributions in different directions around the treatment volume. Sharpening the penumbra of a single field, using conical collimation and reduced energy

(i.e. 2.5 MV), improves the dose fall-off in the aggregate dose distribution as demonstrated in the planar dose distributions contained in Figure 38.

The results contained in this proof-of-concept study motivate further development of this 2.5 MV sintered diamond target stereotactic beam to decrease toxicity in intracranial treatments compared to the standard 6 MV linac-based treatment. In its current state, the prototype beam is restricted to a dose rate of 60 MU/min, restricting its practical use for treatment. This dose rate issue will require industry collaboration to enable clinical translation of 2.5 MV low-Z linac-based treatment.

5.7 Conclusion

This work investigated a novel 2.5 MV sintered diamond target beam for its potential use in intracranial linac-based stereotactic treatments. Compared to the conventional 6 MV beam, the measured profiles demonstrated reductions in the penumbral width and FWHM for the 2.5 MV low-Z beam collimated with both conical and HDMLC collimation. Using the Monte Carlo method, we simulated treatments of trigeminal neuralgia and ocular melanoma to compare dose fall-off for the 2.5 MV low-Z beam compared to 6 MV, for the same PTV dose coverage. In both plans, the 2.5 MV low-Z beam demonstrated improved dose fall-off compared to 6 MV, as evidenced by relative dose profiles through isocenter and reduced OAR doses well exceeding 50%. Though the current dose rate restricts the clinical translation of 2.5 MV low-Z treatment, the results contained in this

study motivate the further development of this beam to improve the achievable dose fall-off in intracranial stereotactic treatments and decrease normal tissue toxicity.

5.8 Additional Material

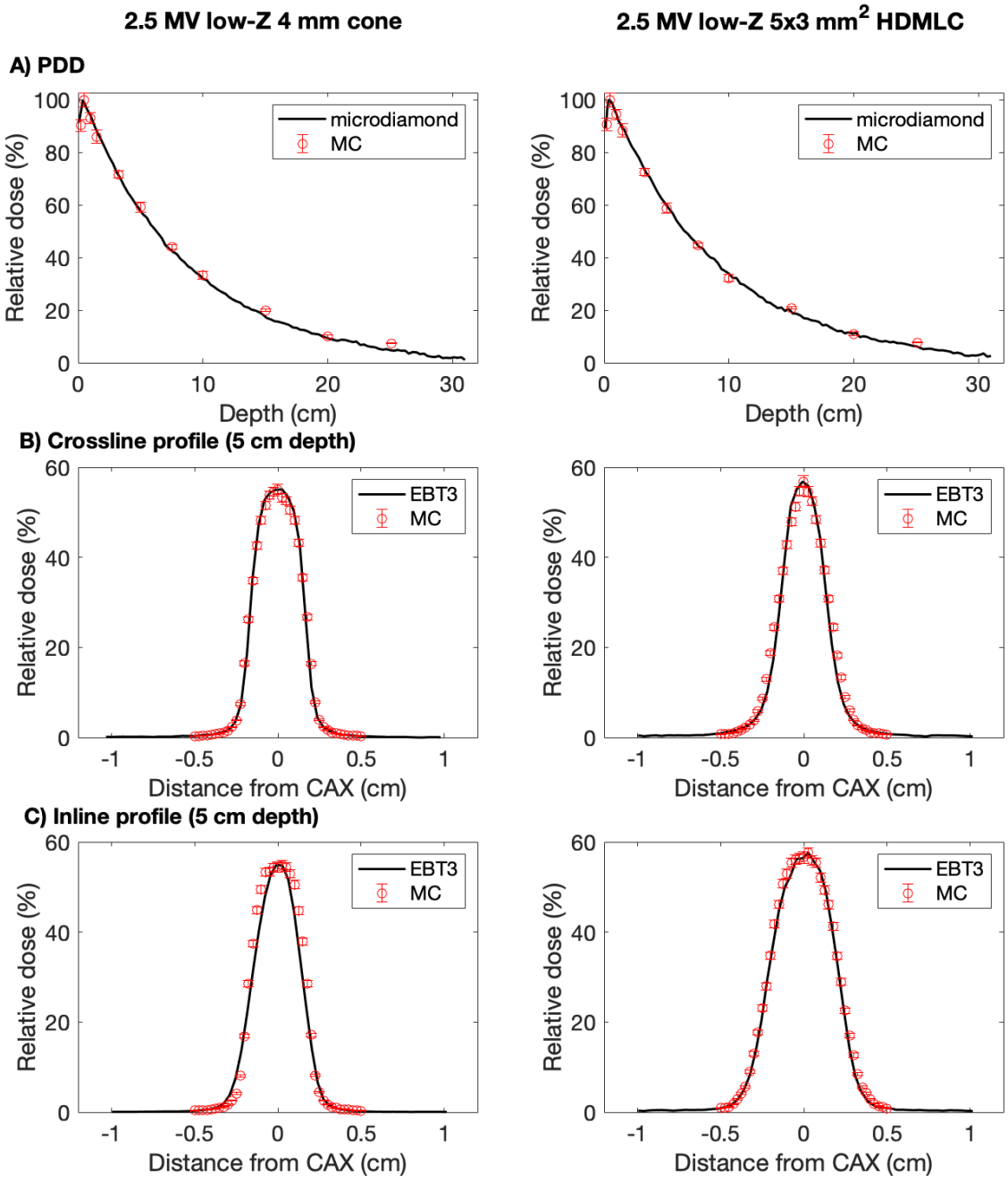

Figure 39. Representative measured and Monte Carlo simulated profiles at 90 cm SSD demonstrating agreement of model in A) PDD, B) crossline profiles measured at 5 cm depth, and C) inline profiles measured at 5 cm depth.

Chapter 6 Conclusions

6.1 Summary

The purpose of this thesis was to investigate a novel 2.5 MV sintered diamond target beam on the TrueBeam platform for potential image quality improvements and treatment applications. Due to the decreased photoelectric absorption of low-energy photons within the sintered diamond target, it was hypothesized that this novel beam would contain a higher proportion of diagnostic energy photons, providing both image quality and dosimetric advantages compared to commercial 2.5 and 6 MV beams. In terms of diagnostic benefits, it was hypothesized that the increased yield of low energy photons would improve the achievable CNR in both planar and volumetric MV imaging due to the increased probability of photoelectric interactions. Regarding therapeutic benefit, it was hypothesized that this increased proportion of low-energy photons would provide sharper dose fall-off in stereotactic treatments due to the decreased lateral scatter of secondary charged particles generated by the primary fluence. These hypotheses were investigated through a series of three manuscripts, describing the design and installation of the experimental low-Z target as well as the methodology for measuring dosimetric characteristics, image quality metrics, and calculating comparative dose distributions for stereotactic treatment applications.

The first manuscript, included in Chapter 3, addressed the design and installation of the sintered diamond target and the image quality characteristics of the 2.5 MV sintered diamond target beam in planar imaging. Due to the photoelectric absorption dependence

on Z^3, it was hypothesized that replacing the 2.5 MV copper target with low-Z sintered diamond would reduce the self-absorption of diagnostic energy photons, producing a softer beam with improved planar CNR. This investigation was carried out using two distinct target setups including i) an external target placed in the carousel of the linac and ii) a clinically realistic setup with target placement in the target arm. Unlike previous studies on older platforms, this work demonstrated an incompatibility of the external target setup on the TrueBeam platform. Placing the target in the target arm was a viable installation setup, for which image quality was measured compared to the commercial 2.5 MV and 6 MV beams. In support of the hypothesis, this study demonstrated a reduction in the beam quality, as measured by the PDD at 10 cm depth, by 2.7% for the 2.5 MV low-Z sintered diamond target beam compared to the commercial 2.5 MV copper target beam. The softer low-Z spectrum provided improved CNR by factors of up to 1.7 times compared to the commercial 2.5 MV beam. This study concluded that due to the improved contrast characteristics, sintered diamond presents as a favorable alternative to the current copper target implemented in the commercial 2.5 MV beamline.

The second manuscript, included in Chapter 4, assessed the volumetric image quality of the novel 2.5 MV low-Z target beam in both full field of view and volume-of-interest CBCT imaging. It was hypothesized that the softer spectrum of the 2.5 MV low-Z target beam would provide CNR advantages in full-field CBCT imaging and further advantages may be realized through a VOI approach due to improved primary-to-scatter characteristics. For full-field CBCT, CNR was measured as a function of imaging dose for various tissue

equivalent materials including lung (inhale and exhale), liver, bone (200 mg/cc) and bone (800 mg/cc) in thin and thick phantoms. In the thick phantom, CNR improvements by factors of up to 1.25 were observed for the 2.5 MV low-Z beam compared to the commercial beam for doses greater than 5 cGy. In the thin phantom, the 2.5 MV low-Z beam demonstrated CNR improvements of up to 1.7 times at doses of ~2 cGy. CNR was evaluated for VOI acquisitions at bone-tissue and bone-sinus interfaces as a function of VOI equivalent radius. These results demonstrated dose reductions of up to 80% outside of the volume, and 20% within the volume for the smallest VOI. In terms of CNR, VOI images demonstrated improvements at the bone-sinus interface compared to the full FOV acquisition. Due to the image quality improvements observed in both full-field and VOI acquisitions, this manuscript suggests the further clinical development of 2.5 MV low-Z CBCT acquisition to improve beam's-eye-view image guidance.

The third manuscript examined the use of the novel 2.5 MV sintered diamond target beam in intracranial stereotactic treatments of trigeminal neuralgia and ocular melanoma. Due to the increased proportion of low-energy photons, it was hypothesized that the 2.5 MV low-Z beam would provide improved dose fall-off compared to the commercial 6 MV beam, owing to the reduced energy, and therefore range, of secondary electrons. Treatments were simulated using Monte Carlo to calculate comparative dose distributions for 6 MV and 2.5 MV low-Z beams with conical and HDMLC collimation. Resultant distributions demonstrated sharper dose fall-off for the 2.5 MV low-Z beam compared to 6 MV for both collimation methods. The improved 2.5 MV low-Z dose fall-

off resulted in reductions to the brainstem dose by greater than 50% in the trigeminal neuralgia case, and reductions greater than 80% for the ipsilateral optic nerve and lens in the ocular melanoma case. This work concluded that the dose sparing benefit offered by the 2.5 MV low-Z beam motivates industry collaboration to enable suitable dose rates for clinical translation of 2.5 MV low-Z treatment.

The results of these three studies demonstrate the combined image quality and dosimetric benefits of the novel 2.5 MV sintered diamond target beam, with improved CNR versus dose characteristics in both planar and volumetric imaging as well as sharper dose fall-off in stereotactic treatments. The prototyped beam investigated in this thesis presents a straightforward modification to the current 2.5 MV beamline which could improve beam's-eye-view image guidance. With increased dose rate, made feasible through industry collaboration, this beam could be implemented in stereotactic treatment to improve dose fall-off and decrease normal tissue toxicity.

6.2 Future directions

The results contained in this work motivate further investigation of this prototyped 2.5 MV sintered diamond target beam to optimize its performance for both imaging and treatment applications. This section highlights the future directions for this work and the motivation behind pursuing them.

While the work in the first two manuscripts demonstrated improved CNR versus dose in MV imaging, the CNR versus dose characteristics of the 2.5 MV diamond target beam is still inferior to kV imaging beams. This disparity is a physical limitation owing to the energy dependent nature of the underlying physics of photon production and interactions. However, the advantages of MV imaging, as follows, motivate the further development of this beam for image guidance.

1. The beam's-eye-view perspective provides visualization of the treatment anatomy with respect to the collimation of the treatment beam.
2. The HU numbers in MV images are directly correlated to electron density.
3. MV imaging provides reduced high-Z artifacts compared to kV acquisitions.

It is anticipated that the 2.5 MV sintered diamond target beam could be further improved by modifying other beamline components. A simple modification which could be implemented in future work involves the removal of the brass cover-plate from the carousel of the 2.5 MV beamline. While this cover-plate is thin (0.81 mm), the additive high-Z material in the beamline may cause beam-hardening which is counterproductive to improving the achievable contrast. Another practical alteration is the implementation of a thick CsI flat-panel detector [98] in place of the current aS1000 detector in the 2.5 MV sintered diamond target beamline. Such a detector, with increased DQE, may further improve the CNR versus dose characteristics of this beam. With further improvement, this beam could potentially be useful in an adaptive workflow to directly measure attenuation maps for online dose calculations using integrated kV/MV acquisitions, or to reduce the appearance of high-Z artifacts.

While low-Z targets have been primarily investigated on C-arm linacs, this technology could be implemented on newly designed platforms such as the O-ring gantry, e.g. Ethos (Varian Medical Systems), or on a gyroscopic platform, e.g. Zap-X, (Zap-X Surgical) with some extensive modification. Unlike the classic C-arm design, the beamline in the Zap-X and Ethos platforms are configured in-line with the treatment head, negating the need for a bending magnet. In this configuration, the target is fixed to the end of the accelerating waveguide for compactness. Due to this fixation, the implementation of a low-Z target in these beamlines would require redesign of the accelerating waveguide to replace the current target material with a low-Z alternative or to implement a switching target[112]. This switching target assembly could contain a high-Z treatment target and a low-Z imaging target, to permit imaging from the treatment beam's-eye-view. If this modification were to be considered for the Ethos platform, it would be beneficial to consider lowering the beam energy through the installation of an energy switch in the accelerating structure to optimize the CNR vs dose characteristics of the beam.

The treatment planning study performed in the third manuscript was intended as proof-of-concept and requires more vigorous investigation to promote clinical translation. First, the treatment plans were developed using the larger HDMLC field rather than the 4 mm cone. While this choice was practical for planning purposes, it led to clinically infeasible PTV hotspots in the dose distributions calculated for the 2.5 MV and 6 MV conically collimated beams. These plans were also designed using the higher energy 6 MV beam due to limitations of accurately modeling the 2.5 MV sintered diamond target beam in

the TPS. Additionally, these plans were developed using a forward planning approach to arrange static beams; while this was convenient for these purposes, this method does not reflect clinical stereotactic planning strategies. Despite these limitations, this proof-of-concept study demonstrated improved dose fall-off which warrants further investigation of the application of this beam. As an extension of this work, additional comparisons could be made to plaque brachytherapy and protons in the treatment of OM to determine advantages or disadvantages. A caveat in the application of this beam for treatment, which was discussed in the third manuscript, involves the limiting dose rate of 60 MU/min. While this dose rate is sufficient for imaging purposes, it is infeasible for treatment. This drawback would require industry collaboration to optimize the accelerating structure to enable high dose rate delivery at such an energy.

Bibliography

1. World Health Organization. Cancer. World Health Organization.

2. Sung H, Ferlay J, Siegel RL, et al. Global Cancer Statistics 2020: GLOBOCAN Estimates of Incidence and Mortality Worldwide for 36 Cancers in 185 Countries. *CA Cancer J Clin*. 2021;71(3):209-249. doi:10.3322/caac.21660

3. Canadian Cancer Statistics Advisory Committee in collaboration with the Canadian Cancer Society SC and the PHA of C. *Canadian Cancer Statistics 2021*.; 2021.

4. American Cancer Society. *Cancer Facts & Figures 2021*.; 2021.

5. Baskar R, Lee KA, Yeo R, Yeoh KW. Cancer and radiation therapy: Current advances and future directions. *Int J Med Sci*. 2012;9(3). doi:10.7150/ijms.3635

6. Hanahan D. Hallmarks of Cancer: New Dimensions. *Cancer Discov*. 2022;12(1). doi:10.1158/2159-8290.CD-21-1059

7. Delaney G, Jacob S, Featherstone C, Barton M. The role of radiotherapy in cancer treatment: Estimating optimal utilization from a review of evidence-based clinical guidelines. *Cancer*. 2005;104(6). doi:10.1002/cncr.21324

8. Barnett GC, West CML, Dunning AM, et al. Normal tissue reactions to radiotherapy: Towards tailoring treatment dose by genotype. *Nat Rev Cancer*. 2009;9(2). doi:10.1038/nrc2587

9. Begg AC, Stewart FA, Vens C. Strategies to improve radiotherapy with targeted drugs. *Nat Rev Cancer*. 2011;11(4). doi:10.1038/nrc3007

10. Hall EJ, Giaccia AJ. *Radiobiology for the Radiologist: Seventh Edition*.; 2012.

11. Phaniendra A, Jestadi DB, Periyasamy L. Free Radicals: Properties, Sources, Targets, and Their Implication in Various Diseases. *Indian Journal of Clinical Biochemistry*. 2015;30(1). doi:10.1007/s12291-014-0446-0

12. McMahon SJ. The linear quadratic model: Usage, interpretation and challenges. *Phys Med Biol*. 2019;64(1). doi:10.1088/1361-6560/aaf26a

13. Gräfe JL, Owen J, Eduardo Villarreal-Barajas J, Khan RFH. Characterization of a 2.5 MV inline portal imaging beam. *J Appl Clin Med Phys*. 2016;17(5):222-234. doi:10.1120/jacmp.v17i5.6323

14. Parsons D, Robar JL, Sawkey D. A Monte Carlo investigation of low-Z target image quality generated in a linear accelerator using Varian's VirtuaLinac. *Med Phys*. 2014;41(2). doi:10.1118/1.4861818

15. Galbraith DM. Low-energy imaging with high-energy bremsstrahlung beams. *Med Phys*. 1989;16(5). doi:10.1118/1.596332

16. Orton EJ, Robar JL. Megavoltage image contrast with low-atomic number target materials and amorphous silicon electronic portal imagers. *Phys Med Biol*. 2009;54(5):1275-1289. doi:10.1088/0031-9155/54/5/012

17. Ostapiak OZ, O'Brien PF, Faddegon BA. Megavoltage imaging with low Z targets: Implementation and characterization of an investigational system. *Med Phys*. 1998;25(10):1910-1918. doi:10.1118/1.598380

18. Sawkey D, Lu M, Morin O, et al. A diamond target for megavoltage cone-beam CT. *Med Phys*. 2010;37(3):1246-1253. doi:10.1118/1.3302831

19. Faddegon BA, Wu V, Pouliot J, Gangadharan B, Bani-Hashemi A. Low dose megavoltage cone beam computed tomography with an unflattened 4 MV beam from a carbon target. *Med Phys*. 2008;35(12). doi:10.1118/1.3013571

20. Roberts DA, Hansen VN, Niven AC, Thompson MG, Seco J, Evans PM. A low Z linac and flat panel imager: comparison with the conventional imaging approach. *Phys Med Biol*. 2008;53(22):6305-6319. doi:10.1088/0031-9155/53/22/003

21. Flampouri S, Evans PM, Verhaegen F, Nahum AE, Spezi E, Partridge M. Optimization of accelerator target and detector for portal imaging using Monte Carlo simulation and experiment. *Phys Med Biol*. 2002;47(18):3331-3349. doi:10.1088/0031-9155/47/18/305

22. Flampouri S, McNair HA, Donovan EM, et al. Initial patient imaging with an optimised radiotherapy beam for portal imaging. *Radiotherapy and Oncology*. 2005;76(1):63-71. doi:10.1016/j.radonc.2005.04.006

23. Parsons D, Robar JL. Beam generation and planar imaging at energies below 2.40 MeV with carbon and aluminum linear accelerator targets. *Med Phys*. 2012;39(7Part2):4568-4578. doi:10.1118/1.4730503

24. Robar JL, Connell T, Huang W, Kelly RG. Megavoltage planar and cone-beam imaging with low- targets: Dependence of image quality improvement on beam energy and patient separation. *Med Phys*. 2009;36(9Part1):3955-3963. doi:10.1118/1.3183499

25. Connell T, Robar JL. Low-Z target optimization for spatial resolution improvement in megavoltage imaging. *Med Phys*. 2010;37(1):124-131. doi:10.1118/1.3267040

26. Motz JW. Bremsstrahlung differential cross-section measurements for 0.5- and 1.0-Mev electrons. *Physical Review*. 1955;100(6). doi:10.1103/PhysRev.100.1560

27. Robar JL. Beam's eye view imaging with low atomic number linear accelerator targets. In: *Beam's Eye View Imaging in Radiation Oncology*. ; 2017. doi:10.1201/9781315120928-8

28. Sheehan JP, Yen CP, Lee CC, Loeffler JS. Cranial stereotactic radiosurgery: Current status of the initial paradigm shifter. *Journal of Clinical Oncology*. 2014;(26). doi:10.1200/JCO.2013.53.7365

29. Keller BM, Pignol JP, Presutti J, Beachey DJ. Intermediate energy photons (1 MV) to improve dose gradient, conformality, and homogeneity: Potential benefits for small field intracranial radiosurgery. *Med Phys*. 2009;36(1). doi:10.1118/1.3026588

30. Solberg TD, Siddon RL, Kavanagh B. Historical Development of Stereotactic Ablative Radiotherapy. In: ; 2012. doi:10.1007/174_2012_540

31. Laughlin JS, Mohan R, Kutcher GJ. Choice of optimum megavoltage for accelerators for photon beam treatment. *Int J Radiat Oncol Biol Phys*. 1986;12(9). doi:10.1016/0360-3016(86)90277-4

32. O'Malley L, Pignol JP, Beachey DJ, Keller BM, Presutti J, Sharpe M. Improvement of radiological penumbra using intermediate energy photons (IEP) for stereotactic radiosurgery. *Phys Med Biol*. 2006;51(10). doi:10.1088/0031-9155/51/10/012

33. Weidlich GA, Schneider MB, Adler JR. Self-Shielding Analysis of the Zap-X System. *Cureus*. Published online 2017. doi:10.7759/cureus.1917

34. Ding G. Is there a dosimetric advantage of using 2.5 MV over 6 MV photons for stereotactic radiosurgery? In: *Joint AAPM and COMP Meeting, Virtual*. ; 2020.

35. Ding GX, Homann KL. The effects of different photon beam energies in stereotactic radiosurgery with cones. *Med Phys*. 2023;50(8). doi:10.1002/mp.16435

36. Khaledi N, Hayes C, Belshaw L, Grattan M, Khan R, Gräfe JL. Treatment planning with a 2.5 MV photon beam for radiation therapy. *J Appl Clin Med Phys*. 2022;23(12). doi:10.1002/acm2.13811

37. Gilbo P, Zhang I, Knisely J. Stereotactic radiosurgery of the brain: A review of common indications. *Chin Clin Oncol*. 2017;6. doi:10.21037/cco.2017.06.07

38. Trifiletti DM, Ruiz-Garcia H, Quinones-Hinojosa A, Ramakrishna R, Sheehan JP. The evolution of stereotactic radiosurgery in neurosurgical practice. *J Neurooncol*. 2021;151(3). doi:10.1007/s11060-020-03392-0

39. Scoccianti S, Detti B, Gadda D, et al. Organs at risk in the brain and their dose-constraints in adults and in children: A radiation oncologist's guide for delineation in everyday practice. *Radiotherapy and Oncology*. 2015;114(2). doi:10.1016/j.radonc.2015.01.016

40. Nichols EE, Richmond A, Daniels AB. Disparities in Uveal Melanoma: Patient Characteristics. *Semin Ophthalmol*. 2016;31(4). doi:10.3109/08820538.2016.1154176

41. Pereira PR, Odashiro AN, Lim LA, et al. Current and emerging treatment options for uveal melanoma. *Clinical Ophthalmology*. 2013;7. doi:10.2147/OPTH.S28863

42. Akbaba S, Foerster R, Nicolay NH, et al. Linear accelerator-based stereotactic fractionated photon radiotherapy as an eye-conserving treatment for uveal melanoma. *Radiation Oncology*. 2018;13(1). doi:10.1186/s13014-018-1088-9

43. Yazici G, Kiratli H, Ozyigit G, et al. Stereotactic Radiosurgery and Fractionated Stereotactic Radiation Therapy for the Treatment of Uveal Melanoma. *Int J Radiat Oncol Biol Phys*. 2017;98(1). doi:10.1016/j.ijrobp.2017.02.017

44. Brewington BY, Shao YF, Davidorf FH, Cebulla CM. Brachytherapy for patients with uveal melanoma: Historical perspectives and future treatment directions. *Clinical Ophthalmology*. 2018;12. doi:10.2147/OPTH.S129645

45. Weber DC, Bogner J, Verwey J, et al. Proton beam radiotherapy versus fractionated stereotactic radiotherapy for uveal melanomas: A comparative study. *Int J Radiat Oncol Biol Phys*. 2005;63(2). doi:10.1016/j.ijrobp.2005.01.057

46. Zakrzewska JM, Linskey ME. Trigeminal neuralgia. *BMJ*. 2014;348:g474. doi:10.1136/bmj.g474

47. Lambru G, Zakrzewska J, Matharu M. Trigeminal neuralgia: A practical guide. *Pract Neurol*. 2021;21(5). doi:10.1136/practneurol-2020-002782

48. Kc E, Islam J, Park YS. Trigeminal ganglion itself can be a viable target to manage trigeminal neuralgia. *Journal of Headache and Pain*. 2022;23(1). doi:10.1186/s10194-022-01512-x

49. Singh R, Davis J, Sharma S. Stereotactic Radiosurgery for Trigeminal Neuralgia: A Retrospective Multi-Institutional Examination of Treatment Outcomes. *Cureus*. Published online 2016. doi:10.7759/cureus.554

50. International Atomic Energy Agency. *Radiation Oncology Physics: A Handbook for Teachers and Students. Podgorsak*.; 2004.

51. Gibbons JP. *Khan's the Physics of Radiation Therapy*.; 2019. doi:10.4103/jmp.jmp_17_20

52. Miklos Gaspar. IAEA Receives Medical Linear Accelerator under Partnership from Manufacturer. International Atomic Energy Agency.

53. Attix FH. *Introduction to Radiological Physics and Radiation Dosimetry*.; 1986. doi:10.1002/9783527617135

54. Nordell B, Brahme A. Angular distribution and yield from bremsstrahlung targets (for radiation therapy). *Phys Med Biol*. 1984;29(7). doi:10.1088/0031-9155/29/7/004

55. Karzmark CJ, Morton RJ. *A Primer on Theory and Operation of Linear Accelerators in Radiation Therapy*. 2nd Ed. Medical Physics Publishing; 1998. doi:10.54947/9781930524965

56. Ding GX, Munro P. Characteristics of 2.5 MV beam and imaging dose to patients. *Radiotherapy and Oncology*. 2017;125(3):541-547. doi:10.1016/j.radonc.2017.09.023

57. Groh BA, Siewerdsen JH, Drake DG, Wong JW, Jaffray DA. A performance comparison of flat-panel imager-based MV and kV cone-beam CT. *Med Phys*. 2002;29(6). doi:10.1118/1.1477234

58. Harold Elford Johns, John Robert Cunningham. *The Physics of Radiology, 4th Ed.* Charles C. Thomas; 1983.

59. Bushberg JT. The Essential Physics of Medical Imaging, Third Edition. *Med Phys*. 2013;40(7).

60. Jaffray DA, Battista JJ, Fenster A, Munro P. Monte Carlo studies of x-ray energy absorption and quantum noise in megavoltage transmission radiography. *Med Phys*. 1995;22(7). doi:10.1118/1.597593

61. Huda W. *Review of Radiologic Physics: Third Edition*.; 2012.

62. Huda W, Abrahams RB. Radiographic techniques, contrast, and noise in x-ray imaging. *AJR Am J Roentgenol*. 2015;204(2). doi:10.2214/AJR.14.13116

63. Hendee WR. The Essential Physics of Medical Imaging. *Radiology*. 1994;191(3). doi:10.1148/radiology.191.3.786

64. Alaei P, Ding GX. Overview Of Image Guidance in Radiation Therapy. In: *Image Guidance in Radiation Therapy:Techniques, Accuracy, and Limitations*. ; 2018. doi:10.54947/9781936366620_ch01

65. Van Herk M. History of MV imaging. In: *Beam's Eye View Imaging in Radiation Oncology*. ; 2017. doi:10.1201/9781315120928-1

66. Rottmann J, Morf D, Fueglistaller R, Zentai G, Star-Lack J, Berbeco R. A novel EPID design for enhanced contrast and detective quantum efficiency. *Phys Med Biol*. 2016;61(17). doi:10.1088/0031-9155/61/17/6297

67. Popescu IA, Shaw CP, Zavgorodni SF, Beckham WA. Absolute dose calculations for Monte Carlo simulations of radiotherapy beams. *Phys Med Biol*. 2005;50(14). doi:10.1088/0031-9155/50/14/013

68. Fenster A, Battista JJ, Munro P. X-ray sources of medical linear accelerators: Focal and extra-focal radiation. *Med Phys*. 1993;20(5). doi:10.1118/1.597106

69. Varian Medical Systems. Monte Carlo Simulation of TrueBeam. myvarian.com/s/montecarlo.

70. Rogers DWO, Faddegon BA, Ding GX, Ma CM, We J, Mackie TR. BEAM: A Monte Carlo code to simulate radiotherapy treatment units. *Med Phys*. 1995;22(5). doi:10.1118/1.597552

71. Iida H. Radiation quantities and units, ICRU report 19, 1971. *Journal of the Atomic Energy Society of Japan / Atomic Energy Society of Japan*. 1972;14(8). doi:10.3327/jaesj.14.430

72. D. Dance, S. Christofides, M. Maidment IM. Diagnostic Radiology Physics: A handbook for teachers and students. *Iaea*. Published online 2014.

73. Das IJ, Kase KR. Higher Energy: Is it Necessary, is it Worth the Cost for Radiation Oncology? *Med Phys*. 1992;19(4). doi:10.1118/1.596779

74. Weidlich GA, Schneider MB, Simcic V, Oostman Z, Adler JR. Self-Shielding for the ZAP-X®: Revised Characterization and Evaluation. *Cureus*. Published online 2021. doi:10.7759/cureus.13660

75. Weidlich GA, Bodduluri M, Achkire Y, Lee C, Adler JR. Characterization of a Novel 3 Megavolt Linear Accelerator for Dedicated Intracranial Stereotactic Radiosurgery. *Cureus*. Published online 2019. doi:10.7759/cureus.4275

76. Weidlich GA, Chung W, Kolli S, Thirunarayanan I, Loysel T. Characterization of the ZAP-X® Peripheral Dose Fall-Off. *Cureus*. Published online 2021. doi:10.7759/cureus.13972

77. D.W.O. Rogers. Monte Carlo Techniques in Radiotherapy. *Physics in Canada*. 2002;58(2):63-70.

78. Bielajew AF. History of monte carlo. In: *Monte Carlo Techniques in Radiation Therapy*. ; 2016. doi:10.1201/9781003211846-2

79. Sobol' IM. *A Primer for the Monte Carlo Method*.; 1994. doi:10.1201/9781315136448

80. Iwan Kawrakow. The Monte Carlo Simulation of Radiation Transport. In: *AAPM Annual Conference*. The American Association of Physicists in Medicine; 1999.

81. Bielajew AF. Fundamentals of the Monte Carlo method for neutral and charged particle transport. *Sciences-New York*. Published online 2000.

82. Kawrakow I, Bielajew AF. On the condensed history technique for electron transport. *Nucl Instrum Methods Phys Res B*. 1998;142(3). doi:10.1016/S0168-583X(98)00274-2

83. Fippel M. Variance reduction techniques. In: *Monte Carlo Techniques in Radiation Therapy*. ; 2016.

84. Daryoush Sheikh-Bagheri, Iwan Kawrakow, Blake Walters, D. W. O. Rogers. Monte Carlo Simulations: Efficiency Improvement Techniques and Statistical Considerations. In: *"Integrating New Technologies into the Clinic: Monte Carlo and Image-Guided Radiation Therapy - Proc. of 2006 AAPM Summer School*. Medical Physics Publishing; 2006:71-91.

85. Sawkey D, Constantin M, Svatos M. WE-F-105-05: A Web Interface to Cloud-Based Treatment Head Simulations. In: *Medical Physics*. Vol 40. ; 2013. doi:10.1118/1.4815621

86. Kawrakow I, Mainegra-Hing E, Rogers DWO, Tessier F, Walters BRB. The EGSnrc Code System : Monte Carlo Simulation of Electron and Photon Transport. Published online 2023.

87. Berger MJ. Monte Carlo calculation of the penetration and diffusion of fast charged particles. *Methods in Computational Physics*. 1963;1.

88. Nelson WR, Hirayama H, Rogers DW. The EGS4 Code System. *System*. 1985;(SLAC-265).

89. Walters B, Kawrakow I, Rogers DWO. DOSXYZnrc Users Manual, NRCC Report PIRS-0794. *National Research Council of Canada*. Published online 2021.

90. Rogers DWO, Walters B, Kawrakow I. BEAMnrc Users Manual. *Source*. Published online 2005.

91. Sawkey D. VirtuaLinac documentation 1.3.0. Published online 2017.

92. Kawrakow I. Accurate condensed history Monte Carlo simulation of electron transport. I. EGSnrc, the new EGS4 version. *Med Phys*. 2000;27(3). doi:10.1118/1.598917

93. Rajapakshe R, Luchka K, Shalev S. A quality control test for electronic portal imaging devices. *Med Phys*. 1996;23(7). doi:10.1118/1.597866

94. Droege RT, Morin RL. A practical method to measure the MTF of CT scanners. *Med Phys*. 1982;9(5). doi:10.1118/1.595124

95. Sun Nuclear Corporation. *CT Electron Density Phantom User Guide*.; 2022.

96. Almond PR, Biggs PJ, Coursey BM, et al. AAPM's TG-51 protocol for clinical reference dosimetry of high-energy photon and electron beams. *Med Phys*. 1999;26(9). doi:10.1118/1.598691

97. Leary D, Robar JL. CBCT with specification of imaging dose and CNR by anatomical volume of interest. *Med Phys*. 2014;41(1). doi:10.1118/1.4855835

98. Tang G, Moussot C, Morf D, Seppi E, Amols H. Low-dose 2.5 MV cone-beam computed tomography with thick CsI flat-panel imager. *J Appl Clin Med Phys*. 2016;17(4). doi:10.1120/jacmp.v17i4.6185

99. Harris TC, Seco J, Ferguson D, et al. Clinical translation of a new flat-panel detector for beam's-eye-view imaging. *Phys Med Biol*. 2020;65(22). doi:10.1088/1361-6560/abb571

100. Myronakis M, Huber P, Lehmann M, et al. Low-dose megavoltage cone-beam computed tomography using a novel multi-layer imager (MLI). *Med Phys*. 2020;47(4). doi:10.1002/mp.14017

101. Borsavage JM, Cherpak A, Robar JL. Investigation of planar image quality for a novel 2.5 MV diamond target beam from a radiotherapy linear accelerator. *Phys Imaging Radiat Oncol*. 2020;16. doi:10.1016/j.phro.2020.10.007

102. Jacobson MW, Lehmann M, Huber P, et al. Abbreviated on-treatment CBCT using roughness penalized mono-energization of kV-MV data and a multi-layer MV imager. *Phys Med Biol*. 2021;66(13). doi:10.1088/1361-6560/abddd2

103. Pouliot J, Bani-Hashemi A, Josephine Chen, et al. Low-dose megavoltage cone-beam CT for radiation therapy. *Int J Radiat Oncol Biol Phys*. 2005;61(2). doi:10.1016/j.ijrobp.2004.10.011

104. Jaffray DA, Battista JJ, Fenster A, Munro P. X-ray scatter in megavoltage transmission radiography: Physical characteristics and influence on image quality. *Med Phys*. 1994;21(1). doi:10.1118/1.597255

105. Robar JL, Parsons D, Berman A, MacDonald A. Volume-of-interest cone-beam CT using a 2.35 MV beam generated with a carbon target. *Med Phys*. 2012;39(7). doi:10.1118/1.4728977

106. Robar JL, Connell T, Huang W, Kelly RG. Megavoltage planar and cone-beam imaging with low- Z targets: Dependence of image quality improvement on beam energy and patient separation. *Med Phys*. 2009;36(9). doi:10.1118/1.3183499

107. Wang J, Robar J, Guan H. Noise suppression in reconstruction of low-Z target megavoltage cone-beam CT images. *Med Phys*. 2012;39(8). doi:10.1118/1.4737116

108. Boas FE, Fleischmann D. CT artifacts: Causes and reduction techniques. *Imaging Med*. 2012;4(2). doi:10.2217/iim.12.13

109. Micke A, Lewis DF, Yu X. Multichannel film dosimetry with nonuniformity correction. *Med Phys*. 2011;38(5). doi:10.1118/1.3576105

110. Tonkopi E, Manos D, Ross A. Does the use of contemporary ct scanners alter the radiation dose debate in the imaging work up for pulmonary embolism? *Radiat Prot Dosimetry*. 2019;187(3). doi:10.1093/rpd/ncz174

111. Al-Senan RM, Hatab MR. Characteristics of an OSLD in the diagnostic energy range. *Med Phys*. 2011;38(7). doi:10.1118/1.3602456

112. Berbeco RI, Detappe A, Tsiamas P, Parsons D, Yewondwossen M, Robar J. Low Z target switching to increase tumor endothelial cell dose enhancement during gold nanoparticle-aided radiation therapy. *Med Phys*. 2016;43(1). doi:10.1118/1.4938410

113. Keller BM, Beachey DJ, Pignol JP. Experimental measurement of radiological penumbra associated with intermediate energy x-rays (1 MV) and small radiosurgery field sizes. *Med Phys*. 2007;34(10). doi:10.1118/1.2775666

114. Varian Medical Systems. ICVI Conical Collimators Representative Beam Data for Eclipse (ICVI_Data_2). *https://www.myvarian.com/s/productdocumentationdetail?Id=069E0000000rsBNIAY&lang=en*.

115. Borsavage JM, Cherpak AJ, Robar JL. Improving image quality and reducing dose with 2.5 MV diamond target volume-of-interest cone beam CT imaging. *Med Phys*. 2022;49(12). doi:10.1002/mp.15974

116. Lynch N, Monajemi T, Robar JL. Characterization of novel 3D printed plastic scintillation dosimeters. *Biomed Phys Eng Express*. 2020;6(5). doi:10.1088/2057-1976/aba880

117. Constantin M, Sawkey D, Svatos M. SU-E-T-504: Electron Beam Tuning Methodology for TrueBeam Phase-Space Library Generation. In: *Medical Physics*. Vol 40. ; 2013. doi:10.1118/1.4814933

118. Varian Medical Systems. TrueBeam Monte Carlo Data Package version 1.1. myvarian.com/s/montecarlo.

119. Varian Medical Systems. Multimet (5) Brain 21/18Gy (HyperArc). https://medicalaffairs.varian.com/edge-multi5brainmetastasis-vmat.

120. Slicer. 3D Slicer image computing platform. slicer@ai.mit.edu.

121. Fedorov A, Beichel R, Kalpathy-Cramer J, et al. 3D Slicer as an image computing platform for the Quantitative Imaging Network. *Magn Reson Imaging*. 2012;30(9). doi:10.1016/j.mri.2012.05.001

Appendix A Copyright permissions

A1 Copyright permission for Investigation of planar image quality for a novel 2.5 MV diamond target beam from a radiotherapy linear accelerator

ISSN:	2405-6316	**Publisher:**	Elsevier
Type of Use:	Republish in a thesis/dissertation	**Portion:**	Chapter/article

LICENSED CONTENT

Publication Title	Physics and Imaging in Radiation Oncol...	**Country**	United Kingdom of Great Britain and N...
Article Title	Investigation of planar image quality fo...	**Rightsholder**	Elsevier Science & Technology Journals
Author / Editor	European Society of Radiotherapy & O...	**Publication Type**	Journal
Date	01/01/2017	**Start Page**	103
Language	English	**Volume**	16

REQUEST DETAILS

Page Range(s)	1-6	**Distribution**	Worldwide
Total Number of Pages	6	**Translation**	Original language of publication
Format (select all that apply)	Electronic	**Copies for the Disabled?**	No
Who Will Republish the Content?	Author of requested content	**Minor Editing Privileges?**	Yes
Duration of Use	Life of current edition	**Incidental Promotional Use?**	No
Lifetime Unit Quantity	Up to 499	**Currency**	USD
Rights Requested	Main product		

NEW WORK DETAILS

Title	The image quality and dosimetric bene...	**Institution Name**	Dalhousie University
Instructor Name	Jennifer Borsavage	**Expected Presentation Date**	2024-08-01

ADDITIONAL DETAILS

The Requesting Person / Organization to Appear on the License	Jennifer Marie Borsavage

REQUESTED CONTENT DETAILS

Title, Description or Numeric Reference of the Portion(s)	Investigation of planar image quality fo...	**Title of the Article / Chapter the Portion Is From**	Investigation of planar image quality fo...
Editor of Portion(s)	Borsavage, Jennifer M.; Cherpak, Aman...	**Author of Portion(s)**	Borsavage, Jennifer M.; Cherpak, Aman...
Volume / Edition	16	**Publication Date of Portion**	2020-11-05
Page or Page Range of Portion	103-108		

A2 Copyright permission for Improving image quality and reducing dose with 2.5 MV diamond target volume-of-interest cone beam CT imaging

JOHN WILEY AND SONS LICENSE TERMS AND CONDITIONS

Jun 20, 2024

This Agreement between Jennifer Borsavage ("You") and John Wiley and Sons ("John Wiley and Sons") consists of your license details and the terms and conditions provided by John Wiley and Sons and Copyright Clearance Center.

License Number	5805471237115
License date	Jun 10, 2024
Licensed Content Publisher	John Wiley and Sons
Licensed Content Publication	Medical Physics
Licensed Content Title	Improving image quality and reducing dose with 2.5 MV diamond target volume-of-interest cone beam CT imaging
Licensed Content Author	James L. Robar, Amanda J. Cherpak, Jennifer M. Borsavage
Licensed Content Date	Oct 11, 2022
Licensed Content Volume	49
Licensed Content Issue	12
Licensed Content Pages	11
Type of Use	Dissertation/Thesis
Requestor type	Author of this Wiley article
Format	Print and electronic
Portion	Full article
Will you be translating?	No
Title of new work	The image quality and dosimetric benefits of a novel 2.5 MV sintered diamond target beam on a modern radiation therapy linear accelerator
Institution name	Dalhousie University
Expected presentation date	Aug 2024
The Requesting Person / Organization to Appear on the License	Jennifer Borsavage
Requestor Location	Jennifer Borsavage 30 Snuff Mill Rd. SAUNDERSTOWN, RI 02874 United States Attn: Jennifer Borsavage
Publisher Tax ID	EU826007151
Total	**0.00 USD**
Terms and Conditions	

Appendix B Standard operating procedure – Switching between low-Z carousel mounted target beamline and clinical low-X imaging mode

Low-Z Target Beamline with Target Arm Retracted on TrueBeam v2.5

1. Mode up and run a standard 2.5 MV or 6 MV beam

2. In the *Utilities Bar*, go into the *Carousel* tab

3. Switch the *Mode* to *Manual* and check the *Advanced* box.

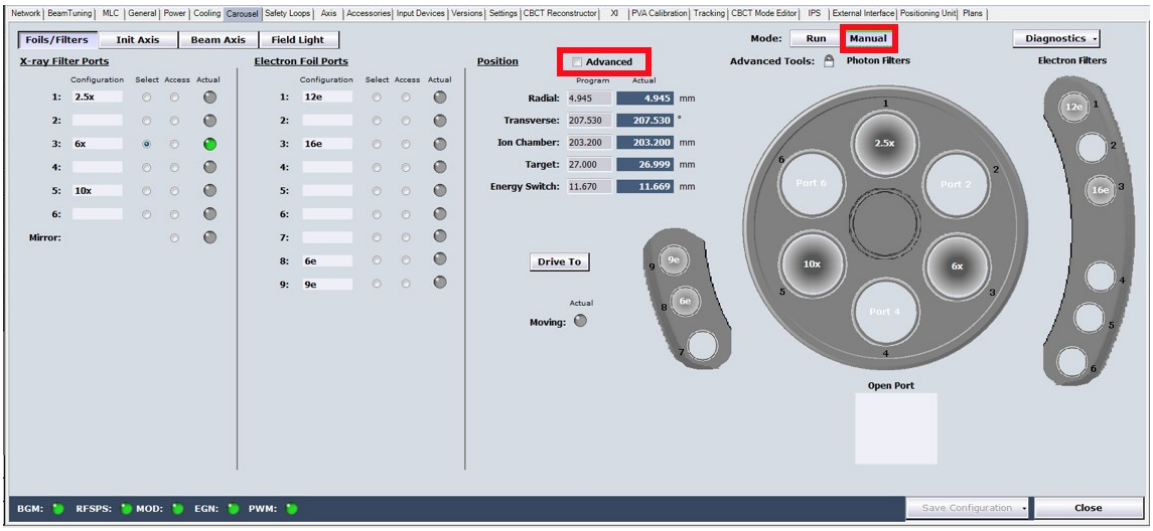

4. Enter the parameters for a retracted target arm and Port 2. Only **Transverse** and **Target** need to be altered.

	6 MV Standard	2.5 MV Standard	6 MV Diamond	2.5 MV Diamond
Radial (mm)	4.945	4.839	4.945	4.839
Transverse (degrees)	207.45	327.530	**27.53**	**267.53**
Ion Chamber (mm)	203.200	203.200	203.200	203.200
(retracted)			(50.0)	(59.96)
Target (mm)	27.000	70.000	**3.500**	**3.500**
Energy Switch (mm)	10.828	12.219	10.828	12.219

5. Once settings are entered hit *Drive To*

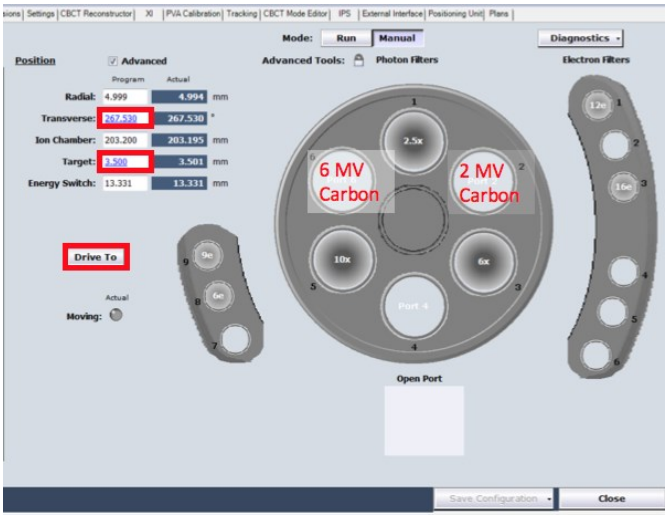

6. In the *Utilities Bar*, go into the *BeamTuning* tab.
Popup window: “Stay in manual mode?” - No.

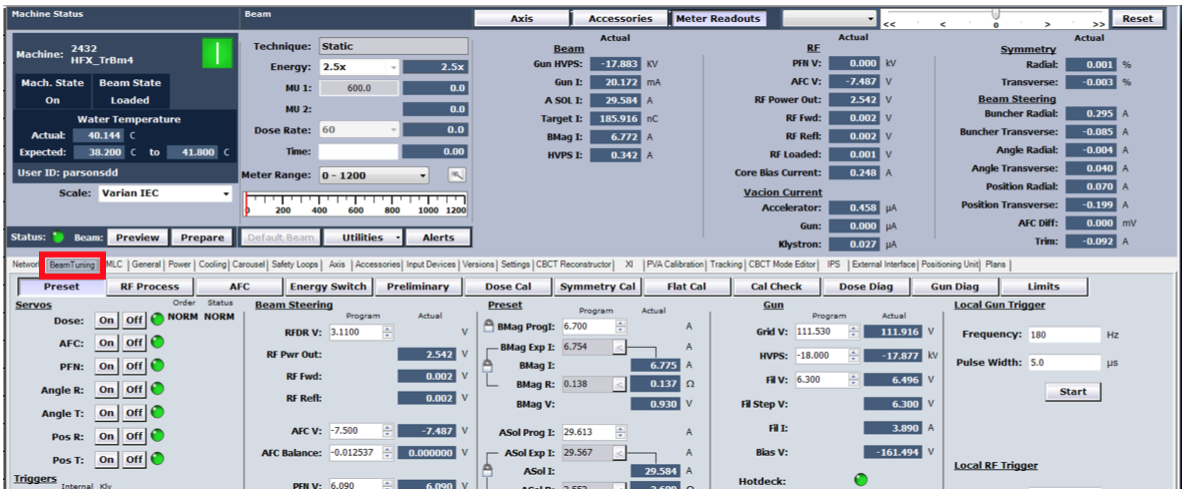

7. Turn off the *Servos* for **Dose, Angle R/T** and **Pos R/T**

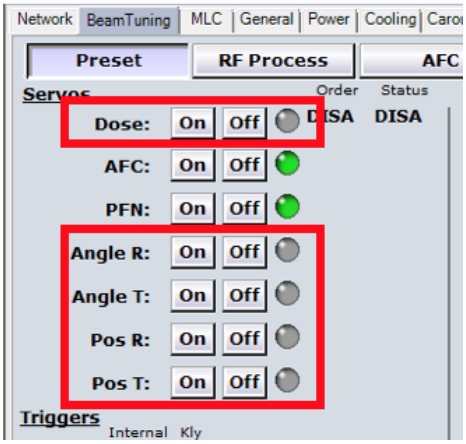

8. Override all of **DOSE**, **FLAT**, **RSYM, TSYM** and **CALCH**.
Additionally, override (these will appear once the beam is running, typically in three batches):

SPV	100000	136009
BGM_S	210016	

<u>DO NOT BLINDLY OVERRIDE INTERLOCKS! ALWAYS CHECK WHAT YOU ARE OVERRIDING!</u>

9. Additionally, some interlocks for running the carousel in manual mode will appear. Override those in the interlock window.

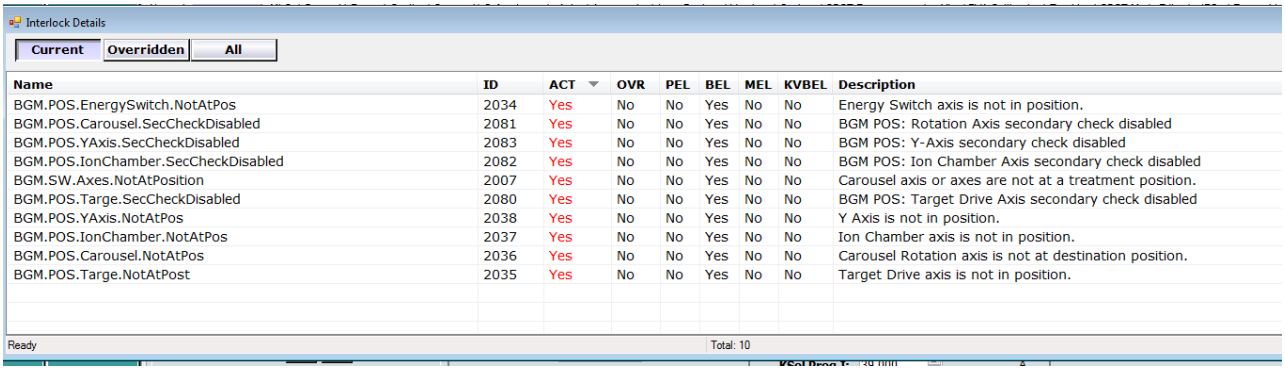

10. In *Machine Controls*, press *Preview* followed by *Prepare*

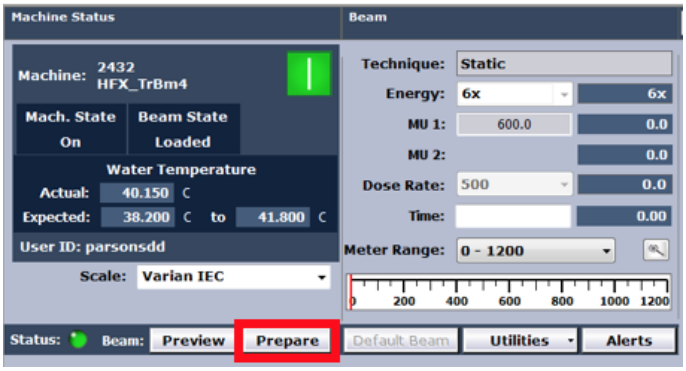

11. Run BEAM. **Always watch the accelerator vacuum!!!! This should never exceed 6 µA!!!** This can be found under *Machine Controls* and pressing *Meter Readouts*.

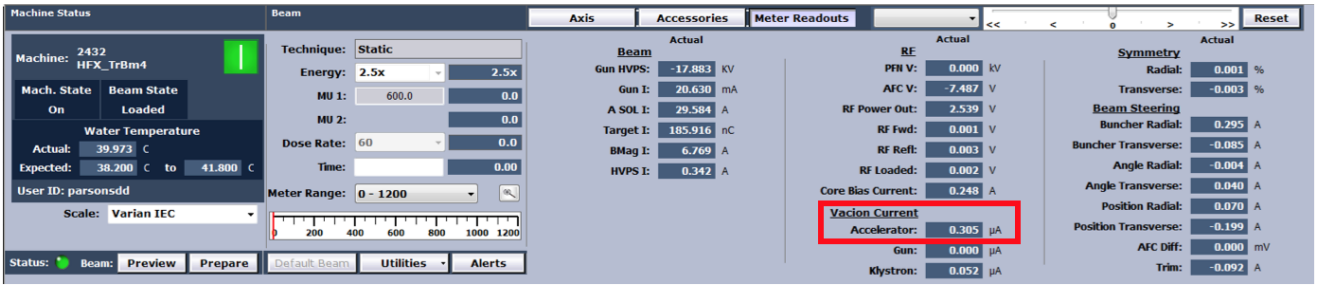

12. When finished with the Low-Z beamline:

a. Un-override the interlocks
b. Turn back on the servos
c. Switch the Carousel to *Run*

13. Reboot the supervisor, found in the *Utilities Bar*, under the *Network* tab. This take approximately 2 minutes to complete.

Post Research QA:

At the end of the night the following needs to occur:

- Verify that new positions match previous recorded positions for 2.5 and 6 MV

	6 MV Standard	2.5 MV Standard
Radial (mm)	4.945	4.839
Transverse (degrees)	207.45	327.530
Ion Chamber (mm)	203.200	203.200
Target (mm)	27.000	70.000
Energy Switch (mm)	10.828	12.219

- Verify beam output with solid water
- Run a patient verification QA in **TREATMENT MODE**

14. Reboot the BGM Subnodes, found in the *Utilities Bar*, under the *Network* tab. This takes approximately 3 minutes to complete.

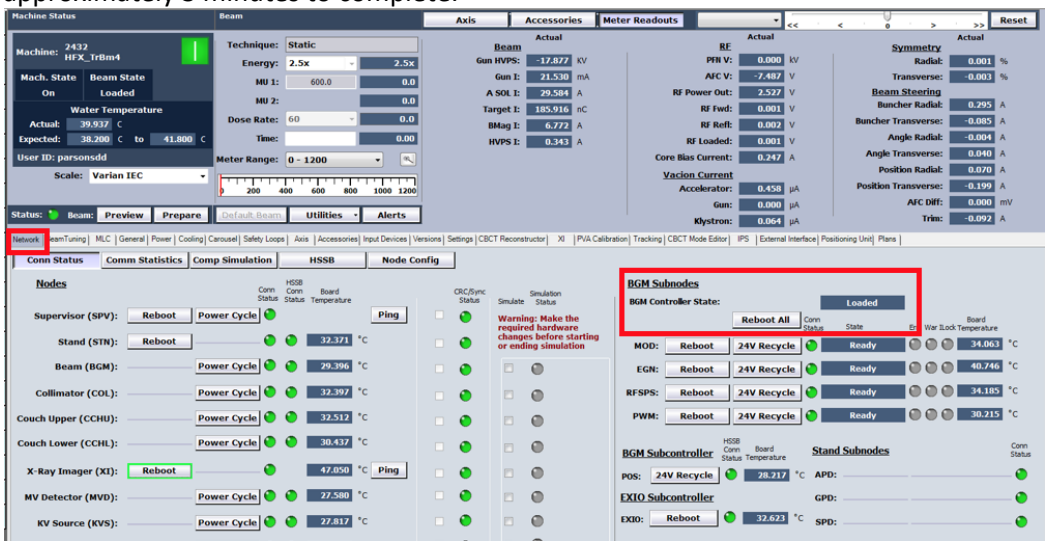

15. Power cycle the BGM, found in the *Utilities Bar*, under the *Network* tab. This takes approximately 5 minutes to complete.

16. Next initialize axis for the MLC and Carousel. MLC is found in the *Utilities Bar*, under the *MLC* tab and pressing *Initialization*.

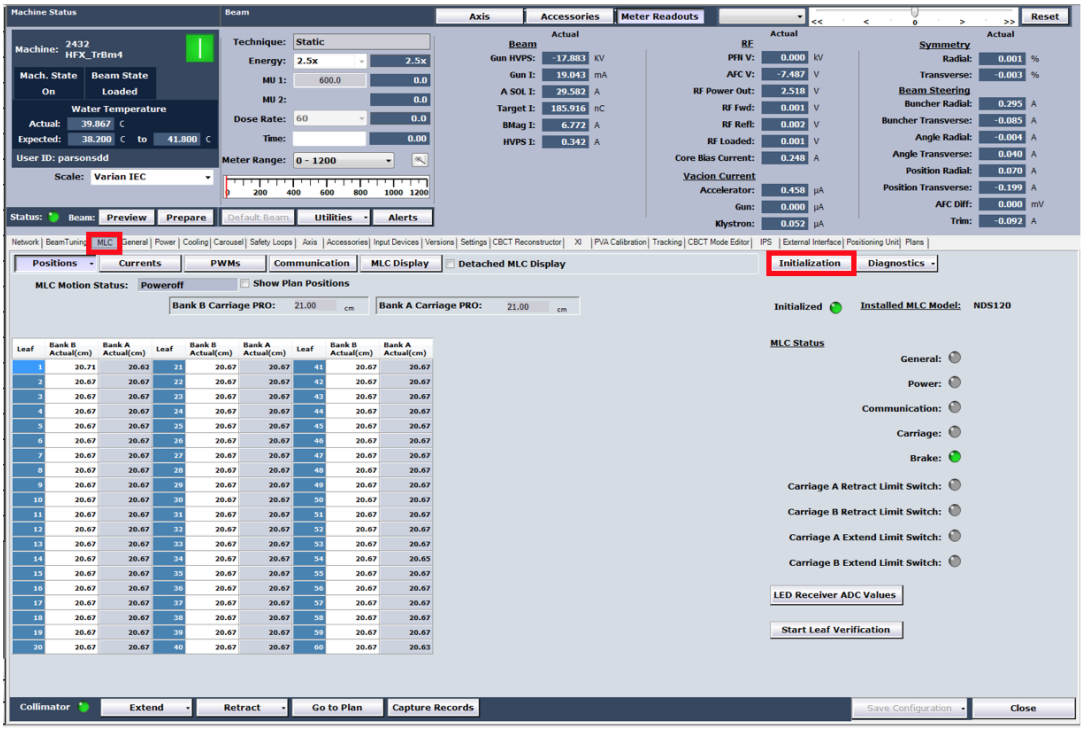

17. Additionally, the Carousel may not initialize. This will require calibrations of the Carousel (essentially homes to each hard stop twice). This should only be for the transverse and radial of the carousel.

This will require more than normal post research QA:

- Verify light field vs x-ray field coincidence with Profiler
- Verify beam symmetry and flatness with Profiler
- Verify un-servoed dose rate